



HAL
open science

Collisional interactions and the transition between lava dome sector collapse and pyroclastic density currents at Tutupaca volcano (Southern Peru)

Karine Bernard, Benjamin van Wyk de Vries, Pablo Samaniego, Patricio Valderrama, Jersy Mariño

► To cite this version:

Karine Bernard, Benjamin van Wyk de Vries, Pablo Samaniego, Patricio Valderrama, Jersy Mariño. Collisional interactions and the transition between lava dome sector collapse and pyroclastic density currents at Tutupaca volcano (Southern Peru). *Journal of Volcanology and Geothermal Research*, 2022, 431, 10.1016/j.jvolgeores.2022.107668 . insu-03825079

HAL Id: insu-03825079

<https://insu.hal.science/insu-03825079v1>

Submitted on 9 Nov 2023

HAL is a multi-disciplinary open access archive for the deposit and dissemination of scientific research documents, whether they are published or not. The documents may come from teaching and research institutions in France or abroad, or from public or private research centers.

L'archive ouverte pluridisciplinaire **HAL**, est destinée au dépôt et à la diffusion de documents scientifiques de niveau recherche, publiés ou non, émanant des établissements d'enseignement et de recherche français ou étrangers, des laboratoires publics ou privés.



Distributed under a Creative Commons Attribution 4.0 International License

Journal of Volcanology and Geothermal Research

Collisional interactions and the transition between lava dome sector collapse and pyroclastic density currents at Tutupaca volcano (Southern Peru).

--Manuscript Draft--

Manuscript Number:	VOLGEO-D-21-00343R3
Article Type:	Research Paper
Keywords:	volcanic debris-avalanche deposit, local kinematics, block clusters, striations, sedimentology.
Corresponding Author:	Karine Bernard, Professor AUBIERE, FRANCE
First Author:	Karine Bernard, Professor
Order of Authors:	Karine Bernard, Professor Benjamin van Wyk de Vries Pablo Samaniego Patricio Valderrama Jersy Mariño
Abstract:	<p>We describe sedimentological variations of the block-rich debris avalanche deposits and associated pyroclastic density current deposits emplaced around AD 1802 from Tutupaca volcano in southern Peru. We use these exceptionally well-preserved features to document the collisional shearing contact between the avalanche and coeval pyroclastic density currents. Furthermore, we show how the first stages of the edifice collapse and syn-cataclastic emplacement process affect the block-size distributions.</p> <p>With field observations, we describe imbricated block clusters, jigsaw cracks and striations related to elongated ridge structures on the deposit surface. Sedimentological and statistical methods (Fourier Shape analysis and Shape Preferred Orientation measured on 208 blocks and 566 mesoscale structures) help us to characterize the cataclastic gradient and establish the collisional relationships between different units. We determine that the proximal impacted deposits and block lithofacies from ridges may be related to distal block units around ~ 10 km run-out distance. Different block clusters indicate a kinematic transition between avalanche units to pyroclastic density currents. Block shape parameters help to differentiate rounded blocks resulting from matrix abrasion with and striated blocks from ridges related to proximal imbricated block clusters. From the statistical dataset, a few equations have been developed indicating a common cataclastic origin with a co-genetic evolution of block lithofacies during sequential syn-cataclastic emplacement.</p> <p>The dome collapse is associated with a specific granular flow regime between avalanche and pyroclastic density currents with secondary reworking. Cyclic impact waves contribute to block cluster growth. Clusters are disaggregated during shock propagation. The inherited shapes of the block lithofacies with $a/b = 1.2-2$ and ellipses $= 0.2-2.5$ indicate the reworking by impact waves. A multidirectional switch to mass spreading in the median zone between 2 and 6 km may be considered with secondary flow and segregation waves. A basal frictional regime with striations is differentiated from collisional cataclastic flow, generating polymodal grooves during peak velocity at the flow front. Impact forces around $\sim 15.7 \times 10^{10}$ N are implied by suggested clast velocities around 8.86 m.s^{-1} and the transitional regime between avalanche units and pyroclastic density currents between 15.5 and 39.6 m.s^{-1}. An extensional disaggregation with the fractal dimensions (D) of the surrounded matrix between 0.6 and 2.8 characterizes the granular transport. A collisional shearing contact probably operated between avalanche units and pyroclastic density currents, which contribute to co-genetic evolution of block clusters from median to frontal distal zones. In the distal zone, abraded block clusters and tilted blocks are related to frontal reworking by impact wave.</p> <p>The cataclastic gradient of avalanche units is correlated with the pyroclastic flow</p>

	regime. Semi-quantitative analysis of block clusters provides information about syn - emplacement processes during sequential impact waves related to volcanic debris-avalanche units and pyroclastic density currents.
Suggested Reviewers:	Lucia Capra lcapra@geociencias.unam.mx Debris avalanche
	Jean-Luc Schneider l.schneider@epoc.u-bordeaux1.fr debris avalanche
	Marcus Bursik mib@buffalo.edu Striations and PDC
	Greg Valentine gav4@buffalo.edu Volcanic deposits
Opposed Reviewers:	
Response to Reviewers:	

Clermont-Ferrand, August 22, 2022

Journal of Volcanology and Geothermal Research

Editor-in-Chief, Dr. Jose Luis Macias

Dear Sir,

We would like to re-submit the revised manuscript entitled: ‘*Collisional interactions and the transition between lava dome sector collapse and pyroclastic density currents at Tutupaca volcano (Southern Peru)*.’ to the Journal of Volcanology and Geothermal Research. We acknowledge your editorial comments as well as the reviewers for their useful remarks. The rebuttal letter describes how we abode by all requested changes, which appear in blue in the revised paper. This revised manuscript contains 26 pages, 5 tables, 10 figures and 2 Supplemental files. The research project presented in this manuscript has been conducted by a group of five researchers from the Laboratory Magmas and Volcans at the University Clermont Auvergne in French and the Institut de la Recherche pour le Développement (IRD) and supported by LMV and IRD.

The revision takes account of the suggestions about the definitions and the figure of the shape parameters (Feret diameter, roughness...) for the debris avalanche, which are described separately in Table 3. To facilitate the reading of this study, we provide the original data in Supplementary files 1 and 2 to calculate the fractal dimension, the mean values and standard errors of the shape parameters. The negative values of fractal dimension have been removed and the standard errors ($<10^{-3}$) related to photographic shot geometries have been considered. Figures and statistical parameters with no clear correlations (with $R^2 \leq 0.5$) that we attributed to the shape variations of block lithofacies and striations based on textural parameters have been removed (Figs. 9B-10B) according to reviewers 1 and 2.

We hope that our revised manuscript meets the high standard of the Journal of Volcanology and Geothermal Research, and we look forward to hearing from the Editorial Board. Thank you very much for your consideration on this matter.

Yours sincerely,

Karine Bernard and co-authors

Please address all correspondence to the first and corresponding Author:

Laboratoire Magmas et Volcans LMV UMR6524 CNRS, OPGC and IRD UR 163,

Université Clermont-Auvergne, 6 avenue Blaise Pascal, Campus les Cézeaux, 63178 Aubière, France.

Phone: +33 (0)4 73 34 67 74; E-mail: kbernard@opgc.univ-bpclermont.fr

Co-authors: Benjamin van Wyk de Vries, also at LMV and UCA, Pablo Samaniego, also at LMV and IRD, Patricio Valderrama at Departamento de Ingenieria, Pontificia Univesidad Catòlica del Perú, Jersy Mariño at INGEMMET.

1 1. Introduction

2 1
3 2 Volcanic debris-avalanche deposits are often associated with pyroclastic density currents and lahar deposits
4 4 (i.e. Mount Saint Helens in the USA, [Glicken, 1986](#)), suggesting interactions during flow propagation. The
5 6 stratigraphic relationships between the associated *syn*-eruptive volcanic deposits are described, implying
6 8 differential kinematic between the mass flow such as striations and grooves on clast faces related to dome-
7 9 collapse generating avalanche deposits interstratified between pyroclastic units (Mono Craters, CA, [Dennen
11
12 et al., 2014](#)); matrix transformations into lahar deposits (Misti in Peru, [Bernard et al., 2017](#)). Block lithofacies
13
14 are rarely used to characterize the differential movements inside the mass flow during *syn*-eruptive collapse.
15
16 A basal frictional regime with striations is differentiated from an upper collisional cataclastic flow for block
17 17 lithofacies (e.g. Parinacota and Ollagüe in Chile, [Clavero et al., 2002](#); [Clavero et al., 2004](#); El Zaguán,
18
19 Mexico, [Caballero and Capra, 2011](#)).
20
21 Lava dome extrusion produced block lithofacies may be mixed with matrix-rich debris-avalanche deposits
22
23 (Mount Saint Helens, [Glicken 1986](#); Parinacota in Chile, [Clavero et al., 2002](#); Tutupaca in Peru, [Samaniego
24
25 et al., 2015](#); [Valderrama et al., 2016](#)). Different avalanche structures are identified with such block
26 26 lithofacies: (1) *torevas* that are large blocks ($L > 100$ m), which occur in the proximal zones and could
27 27 constitute up to ~30% of the debris avalanche deposits (Socompa in Chile, [Davies et al., 2010](#)). (2) Type A
28 28 hummocks that are large cataclased blocks ($H < 80$ m, $w < 300$ m, $L < 400$ m, Mount Saint Helens, [Voight et
29
30 al., 1981](#); [Glicken, 1998](#); Jocotitlán in Central Mexico, [Siebe et al., 1992](#); Parinacota and Taapaca in Chile,
31
32 [Clavero et al., 2002](#); [Clavero et al., 2004](#)) with steep slopes. (3) Longitudinal or transverse ridges ($H = 10$ -30
33
34 m, [Shea and van Wyk de Vries, 2008](#); [Dufresne and Davies, 2009](#); [Andrade and van Wyk de Vries, 2010](#)),
35
36 that are attributed to deflection of the mass flow ([Valderrama et al., 2018](#)). The alignment of blocks or
37
38 isolated blocks between 0.01 and 1000 m can be observed in some debris avalanche deposits (Socompa, [van
39
40 Wyk de Vries et al., 2001](#); [Shea and van Wyk de Vries, 2008](#)). The frontal lobes thrust the large blocks in
41
42 distal zones (Jocotitlán, [Siebe et al., 1992](#)) showing fluidization with matrix transformations into lahars
43
44 (Perrier in French Massif Central, [Bernard and van Wyk de Vries, 2017](#)). Different mesoscale structures have
45
46 been described related to specific kinematic context such as gravitational flank collapse with an initial
47
48 dilation of jigsaw-fit textures (Mount Saint Helens, [Glicken, 1986](#)), abrasion and striations along fault planes
49
50 ([Mehl and Schmincke, 1999](#)), collisional textures during transport (El Zaguán in Mexico, [Caballero and
51
52 Capra, 2011](#)), and impact waves with pseudotachylite and gouge along avalanche fault zones (Pichu Pichu in
53
54 Peru, [Legros et al., 2000](#); Mont Dore in French Massif Central, [Bernard and van Wyk de Vries, 2017](#)).
55
56 *Syn*-eruptive collapses of a volcanic edifice and volcano-sedimentary processes have been well documented
57
58 at Las Derrumbadas Volcano, Mexico ([Guilbaud et al., 2022](#)), Panum Crater, (Mono Crater, CA, [Dennen et
59
60 al., 2014](#)) and Tutupaca volcano in southern Peru ([Samaniego et al., 2015](#); [Valderrama et al., 2016](#); [Mariño et
61
62 al. 2021](#)). This volcano hosts probably the well-preserved and displayed lava dome related debris avalanche
63
64
65

36 and pyroclastic density current features that are young and little altered by the climate or human interference.
 37 1 Two volcanic avalanche units exposed in the northeastern part of the Tutupaca collapsed edifice are
 38 2 interstratified with the pyroclastic density current deposits (Samaniego et al., 2015). Block-rich ridge
 39 4 structures have been attributed to granular segregation and differential block velocities in the flowing mass,
 40 6 suggesting the interactions between debris-avalanche units and the associated PDC deposits.

41 8 In this study, we show how semi-quantitative sedimentological analysis of the block lithofacies and
 42 9 mesoscale structures associated to these exceptionally well-preserved volcanic deposits provide information
 43 11 about *syn*-emplacement processes during a collapsing dome generating pyroclastic density currents. To
 44 13 facilitate the reading of this study, we provide a list of the acronyms in Table 1.

45 15 46 17 2. Collisional interactions between volcanic-debris avalanche and pyroclastic density currents: a State- 47 19 of-the-Art

48 21
49 22 The volcanic debris avalanche deposits are commonly associated with PDC. Mount Saint Helens in the USA
 50 24 (Crandell et al., 1984; Glicken, 1986), Bezymianni in Kamchatka (Siebert et al., 1987), Soufrière in
 51 26 Guadeloupe (Boudon et al., 1984) show several sequences of lava dome collapses associated with
 52 28 decompression to the co-magmatic deposits in *syn*-eruptive sequences. The hot volcanic debris-avalanche
 53 30 deposits, gravitational mass spreading ($v = 50-70 \text{ m.s}^{-1}$) of the collapsed edifice, interacted with the blast-
 54 32 generated the PDC, transport of the fluidized mixture of clasts and gas ($v \geq 100 \text{ m.s}^{-1}$, Soufrière, Boudon et
 55 34 al., 1984; Mount Saint Helens 1980, Glicken, 1986; Bezymanni 1956, Saint Augustine, Siebert et al., 1987).
 56 35 The PDCs are interstratified between the debris avalanche units, related to cyclic volcanoclastic
 57 37 sedimentation. Cyclic phases can be differentiated: precursor stages with seismes and localized collapses
 58 39 with hydrothermal alteration, large collapse of altered lava-dome edifice with explosion and the blast-
 59 41 generated the PDC including an open conduit, and different post-collapse eruption. Volcanic lateral blast is
 60 43 associated to the successive shock waves during collapse, with ballistic clasts and sliding blocks generating
 61 45 internal shock structures. Transformations of the debris-avalanche deposits into lahars ($v = 30-40 \text{ m.s}^{-1}$) by
 62 47 dewatering have been observed during initiation of pyroclastic flow such as Mount Saint Helens (Glicken,
 63 49 1986).

64 50 Deposit structures have been formed by interactions between the moving avalanche and the superposed PDC,
 65 52 implicating a strong frictional contact. We observed aggregation of lava block clusters (Taranaki, Zernack et
 66 54 al., 2009) with breccification and curvilinear surfaces related to blocky morphology interactions, pyroclastic
 67 56 slump blocks with progressive disaggregation of blocks, fingering segregation related to ridge structures
 68 58 (Tutupaca, Samaniego et al., 2015; Valderrama et al., 2016), striations and flow bands (Lastaria in Chile,
 69 59 Naranjo and Francis, 1987) with distal digitations related to weak pyroclastic material.

70 61 Different generations of striations have been described related to sliding mode transport during interactions

71 between no-cohesive avalanche lithofacies and PDC: striations of the bedrock in scar (Mount Saint Helens,
 72 [Glicken, 1986](#)); grooves and striations at the base and the underlying substratum; and parallel grooves and
 73 furrow at the base and the upper part of faulted megablocks (Gran Canaria, Spain, [Mehl and Schmincke,](#)
 74 [1999](#)). We differentiate an upper collisional regime with impact marks at the surface of block lithofacies
 75 (Parinacota and Ollague in Chile, [Clavero et al., 2002](#); [Clavero et al., 2004](#)). Impact marks and linear trends
 76 appear concentrated on one side of blocks, showing conchoidal fractures related to collisional interactions
 77 between the blocks.

78 We examine how block lithofacies of volcanic debris avalanche deposits interact with PDC to generate block
 79 clusters and grooves with striations related ridges structures. We show how semi-quantitative
 80 sedimentological analysis of the block lithofacies and mesoscale structures provide information about *syn-*
 81 emplacement processes such as the force F of impact of clasts onto block surfaces and the clast velocity for
 82 making impact marks ([Clavero et al., 2002](#)).

84 3. Analytical methods

85 From the field observations on the debris-avalanche units, we have described the textural variations of the
 86 block lithofacies assemblages and assessed their relationships to avalanche fault zones. A semi-quantitative
 87 sedimentological analysis was conducted to characterize block distributions ([Table 2](#)). From these data, we
 88 were able to differentiate the block lithofacies in each zone associated with cataclastic gradient between the
 89 avalanche units and pyroclastic density current deposits ([Samaniego et al., 2015](#); [Valderrama et al., 2016](#)). To
 90 facilitate the reading of this study, we provide a list of the acronyms in [Table 1](#).

93 3.1. Field observations and outcrop analysis

94 The lithology of different outcrops were identified from proximal to distal zones to characterize the
 95 discontinuous block-rich lithofacies, related to interactions between volcanic avalanche and pyroclastic
 96 density current deposits. From field observations and Google Earth imagery, the block-rich avalanche units
 97 were described and mapped according to stratigraphic and geomorphological context and avalanche
 98 structures ([Samaniego et al., 2015](#); [Valderrama et al., 2016](#)).

99 Quantitative morphological data such as area (S), thickness (T) and volume ($V = ST$; [Table 1](#)) on the surface
 100 avalanche deposits are calculated from the mapped surfaces and georeferenced Google Earth images
 101 ([Samaniego et al., 2015](#); [Valderrama et al., 2016](#)). These morphological data are compared to other avalanche
 102 deposits worldwide such as those emplaced around Mount Saint Helens and Mount Shasta in the USA
 103 ([Crandell et al., 1984](#); [Glicken, 1986](#)), Bezymianni in Kamchatka ([Siebert et al., 1987](#)), Parinacota in Chile
 104 ([Clavero et al., 2002](#)), Soufrière in Guadeloupe ([Boudon et al., 1984](#)) and Mont Dore in French Massif

106 Central (Bernard and van Wyk de Vries, 2017). From these examples, we correlate the morphological data
 107₁ with the structural units of avalanche deposits, implying interactions between lava dome sector collapse and
 108₂ pyroclastic density currents. The contacts between the block lithofacies and matrix textures of volcanic
 109₃ debris-avalanche deposits with interstratified PDC were analyzed. Lithostratigraphic sections were
 110₄ established and correlated with textural variations.

111₅ The use of the Shape Preferred Orientation 2003 software (Fig. 1A, SPO, Launeau and Robin, 2005)
 112₆ provided a semi-quantitative description of block avalanche units, allowing us to estimate imbrication of 508
 113₇ blocks and block axial distributions with the inertia and intercepts method. Image analysis of the block
 114₈ lithofacies and mesoscale structures provide relative information because photographs can be affected by
 115₉ perspective. Two-dimensional shape parameters of blocks, such as the a/b ratio (the largest axis / minor axis)
 116₁₀ and sectional ellipse values from system of linear equations (see Launeau and Robin, 2005 for mathematical
 117₁₁ definitions), have been calculated, to characterize block fabric related to *syn*-emplacement structures
 118₁₂ (Bernard, 2015; Bernard and van Wyk de Vries, 2017; Bernard et al., 2019), together with striations and
 119₁₃ grooves in blocks. Ellipse/ a/b values contribute to establish textural classes of avalanche fault zones (~2.14
 120₁₄ for the plane collapse, 1.75 to 2 for the crushing, $a < 1.7$ for the thermal effect of fragmentation, Bernard et
 121₁₅ al., 2019). Mesostructures such as fractures and striations from 2 mm to 20 cm were also analyzed.

122₁₆ 3.2. Sedimentary analysis

123₁₇ From SPO analysis (Launeau and Robin, 2005) of the blocks, the fractal distributions were used to compare
 124₁₈ transport and cataclastic process acting on each avalanche unit. Each cumulative frequency is plotted *versus*
 125₁₉ clast long-axis on double-logarithmic graphs. Fractal dimensions h and D of size distributions were estimated
 126₂₀ from the power regressions (Table 4; see Supplemental File 1; Suzuki-Kamata et al., 2009). The cumulative
 127₂₁ curves of the clast-size distributions *vs.* a/b (Fig. 8) were compared to distinguish the block avalanche units
 128₂₂ from proximal to distal zones. The calculated block-size distributions estimated from 41 outcrop photographs
 129₂₃ with the inertia and intercepts methods using the SPO analysis (from metric-size blocks to clasts >10 cm;
 130₂₄ Fig. 8B; Launeau and Robin, 2005). The longest axis of 404 block outlines were measured and counted per
 131₂₅ image area from the photographs. The normalized frequency histograms (Launeau and Robin, 2005) were
 132₂₆ produced by grouping the longest axis of blocks (cm) into 100-cm bins (number of size intervals) and
 133₂₇ normalizing the number of occurrences in each bin to the total number of measurements from automatic
 134₂₈ image analysis. The sectional effects have been considered (Launeau and Robin, 2005). These data contribute
 135₂₉ to differentiate the effect of cataclasis between each fraction correlated with different structural units from
 136₃₀ proximal to distal zones. The subdued blocks and clasts below 10 cm are not considered related to resolution
 137₃₁ limits.

138₃₂ The shape analysis using the ImageJ Plugin “Gold morph” has been applied to 404 blocks and 635 striations

141 of the avalanche units to compute minor and major axis length, [Feret's diameter defined as the longest](#)
 142 [distance between two parallel tangential lines](#), perimeter and convex perimeter, radii of the smallest inscribed
 143 [and largest circumscribed circles](#) ([Fig. 1B](#); [Table 3](#); [Crawford and Mortensen, 2009](#)). From these data, we
 144 [calculate the \$a/b\$ ratio, the roundness defined as the ratio of the perimeter to convex perimeter, and the Riley's](#)
 145 [circularity, the square root of the ratio of the diameter of the largest inscribed circle to the diameter of the](#)
 146 [smallest circumscribed circle of the volcanic clast](#) ([Table 3](#), [Blott and Pye, 2008](#); [Bernard, 2015](#)). [The values](#)
 147 [of Riley's circularity are less than 1 for the non-spherical volcanic clasts](#) ([Table 5](#)).

148 [To characterize the two-dimensional shape of mesoscale structures, we took 5.9 megapixel photographs of](#)
 149 [abraded flat surfaces of two blocks with a digital camera. A digital camera \(6.2-18.6 mm lens, 35-105 mm](#)
 150 [focal length\) image at a camera distance of <20 cm had a standard error for mean distortion around \$\sim 10^{-3}\$.](#) All
 151 [the striations observed in the median zone have been quantified by using high-resolution images \(3648 X](#)
 152 [2736 pixels\) of two block faces. Abraded flat surfaces of the two megablocks on these scales contribute to](#)
 153 [preserve geometries of these grooves and striations with circular depressions \(\$\sim 1\$ -5 cm depth, 2-3 mm wide\).](#)
 154 [These are enough to generate semi-quantitative analysis using the ImageJ Plugin "Gold morph" and SPO](#)
 155 [\(566 mesoscale structures, \[Launeau and Robin, 2005\]\(#\); \[Blott and Pye, 2008\]\(#\); \[Crawford and Mortensen, 2009\]\(#\)\).](#)
 156 [The roundness, the Riley's circularity, the \$a/b\$ ratio, ellipse, fractal \$D\$ -values of each mesoscale structure have](#)
 157 [been calculated. The calculated standard errors characterize the shape variations between the blocks rather](#)
 158 [than the measurements' uncertainty. Moreover, the calculated standard errors for image analysis are between](#)
 159 [0.03 and 0.3 for \$a/b\$ ratio and around \$\pm 0.9\$ for ellipse values](#) ([Launeau and Robin, 2005](#); [Table 5](#)).

160 [Several statistical regressions \(Eqs. 1-21 in \[Figs. 2\]\(#\) and \[8-10\]\(#\)\) have been established to characterize the](#)
 161 [evolution of block shape and striations related to cataclastic processes between the volcanic debris-avalanche](#)
 162 [units and pyroclastic density current deposits. Figure 9 shows the evolution of the roundness with Feret's](#)
 163 [diameter for block lithofacies and striations. Figure 10 shows the evolution of the roundness with Feret's](#)
 164 [diameter for block clusters. The intersecting points between few regressions indicate similar values of shape](#)
 165 [parameters related to the inherited clast shape for lava blocks and co-genetic relationships between block](#)
 166 [lithofacies.](#)

167 [Statistical and shape parameters were compared with those from other avalanche units in the Andean Central](#)
 168 [Volcanic Zone such as the Pichu Pichu debris avalanche deposit, and the matrix of the ridges from the](#)
 169 [Tutupaca volcanic debris-avalanche deposits](#) ([Bernard, 2015](#); [Valderrama et al., 2016](#); [Bernard et al., 2019](#)).

170 [The impact of clasts onto block surfaces](#) ([Clavero et al., 2002](#)) can be approximated as $r = 0.5a^2/h$ with r ,
 171 [radius of spherical portion of clasts; \$a\$, radius of hemispherical damage zone, and \$h\$, distance that penetrated](#)
 172 [into the block. The force \$F\$ of impact is given by Clavero et al. \(2002\):](#)

$$173 F = \Pi a^2 \rho_0$$

174 [where \$\rho_0\$ is the hardness of the material. The clast velocity for making impact marks can be estimated by](#)
 175 [using \$V = \(0.5 \Pi \rho_0 / Mr\)^{1/2} a^2\$ with \$M\$, the mass of the rock](#) ([Clavero et al., 2002](#)). The avalanche velocity in the

176 middle zone is considered by using $v = (2gH)^{1/2}$.

177 1 A combination of several semi-quantitative methods has been used to determine (Table 1): (1) the links
 178 2 between the different block-rich units related to the debris avalanche and the associated pyroclastic density
 179 3 currents; (2) the quantitative sedimentary comparisons of the block lithofacies to define the conditions
 180 4 generating these deposits; (3) the in-motion controls and the dynamic cataclasis during the differential
 181 5 sedimentary emplacement between the volcanic debris-avalanche units and the pyroclastic density current
 182 6 deposits.

183 7 184 8 **4. Geological and geomorphological context of the study area**

185 9 186 10 *4.1. Tutupaca volcanic complex and the geomorphological context*

187 11
 188 12 The Tutupaca volcanic complex (~5815 m on above sea level, Fig. 3) is composed by three edifices: an
 189 13 eroded basal edifice (Lower to Middle Pleistocene, Marino et al., 2021) with strong hydrothermal alteration;
 190 14 the Western Tutupaca peak, which was eroded by the late Pleistocene glaciers, and the Holocene Eastern peak
 191 15 composed of seven coalescing lava domes (Holocene, domes I to VII, Fig. 3B, Samaniego et al., 2015;
 192 16 Valderrama et al., 2016; Marino et al., 2021), constructed on the older hydrothermally-altered basal edifice.
 193 17 The activity of the recent domes is historic (about 218 ± 14 calBP), and little altered by the arid, stable, cold
 194 18 climate, or by human activity, apart from a few small tracks and limited mining exploration excavations. The
 195 19 area is mostly wild, and in its natural state. The lava domes of the Eastern Tutupaca peak are cut by a
 196 20 horseshoe-shaped amphitheater open to the northeast, with an orthogonal direction to the N140° regional
 197 21 faults. From this, debris avalanche and pyroclastic density current deposits extend, are preserved with very
 198 22 little modification from their initial state (there is some limited frost shattering, and ice related solifluxion).

199 23 Geomorphological parameters on the surface avalanche deposits associated with PDC are calculated and
 200 24 compared to other avalanche deposits worldwide such as those emplaced around Mount Saint Helens and
 201 25 Mount Shasta in the USA (Crandell et al., 1984; Glicken, 1986), Bezymianni in Kamchatka (Siebert et al.,
 202 26 1987), Soufrière in Guadeloupe (Boudon et al., 1984). Impact marks of Parinacota debris avalanche in Chile
 203 27 (Clavero et al., 2002) and pseudotachylite impact in French Massif Central (Bernard and van Wyk de Vries,
 204 28 2017) are considered. A relationship between area (A) and volume (V) is calculated for the Tutupaca units
 205 29 with $A = 28.07 V^{1.01}$ (Eq. 1 in Fig. 2). These are compared to the power regressions of other volcanic debris-
 206 30 avalanche deposits (Eqs. 2-4 in Fig. 2, Glicken, 1986; Clavero et al., 2002; Legros, 2002; Bernard and van
 207 31 Wyk de Vries, 2017). We differentiate an intersecting point A with area around ~ 140 and 180 km^2 and volume
 208 32 between 5 and 7 km^3 .

209 33 210 34 *4.2. The Paipatja debris-avalanche deposits*

211 35
 212 36
 213 37
 214 38
 215 39

211

212 1 Samaniego et al. (2015) described the Paipatja debris avalanche, exposed in the northeastern part of the
 213 2 Tutupaca volcano between the amphitheater and the Paipatja plain ($L = 6-8$ km, $S = 12-13$ km², $T = 25-40$ m,
 214 4 5 Samaniego et al., 2015; Valderrama et al., 2016). Stratigraphic and textural variations are correlated to the
 215 6 7 syn-emplacement structures. The hydrothermally rich debris avalanche deposit (HA-DAD, $L = 6-8$ km, $V < 1$
 216 8 9 km³; $H/L = 0.17-0.23$, Samaniego et al., 2015), that involved large quantities of the basal edifice, is
 217 10 characterized by torevas ($H = 20-40$ m, $L = 1.5$ km), long lateral levees ($L = 1.5$ km) and hummocky-
 218 11 12 structures ($L = 200-800$ m, $H = 20-40$ m) up to 4-6 km from the scar (Samaniego et al., 2015; Valderrama et
 219 13 14 al., 2016).

220 15 16 Block ridge structures and levees are observed between 2 and 6 km from the amphitheater (Valderrama et al.,
 221 17 18 2016). In the median zone, elongated and sub-parallel ridge structures ($w = 5-10$ m, $H = 2-5$ m, $L = 150-400$
 222 19 20 m, Fig. 3A), regularly spaced, are related to interstratified pyroclastic density current deposits between two
 223 21 22 avalanche units, implying a *syn-collapse* explosive eruption at Tutupaca volcano (Samaniego et al., 2015).
 224 23 The hydrothermally rich debris avalanche deposit is covered by Paipatja pyroclastic density current deposits
 225 24 25 (P-PDC, ~218 aBP, sections B to E in Fig. 3A).

226 26 27 A dome-rich debris-avalanche deposit (DR-DAD of Samaniego et al., 2015) overlain the P-PDC unit in the
 227 28 29 median zone (section B in Fig. 3). Cross-sections within the ridge structures reveal the dipping and
 228 30 31 undulating contacts between the P-PDC units and the DR-DAD (section B in Fig. 3A). The P-PDC, on the
 229 32 33 upper part of HA-DAD, appears thickest between the ridge structures and around the largest blocks
 230 34 (Valderrama et al., 2016). We have observed dome fragments (from centimeters to several meters in size),
 231 35 36 such as metric-size dacitic blocks and prismatic jointed blocks showing inherited jigsaw-cracks,
 232 37 38 cataclastic and shearing structures. The abraded and sub-rounded blocks are subdued in the underlying
 233 39 40 avalanche deposit and PDC.

234 41 The Tutupaca volcanic debris-avalanche deposits show different units with specific granular assemblages
 235 42 43 (30% of HA-DAD and 70% of DR-DAD, Valderrama et al., 2016). Dense blocks (3-20 cm in diameter) and
 236 44 45 bombs from the P-PDC unit (20-40%) have highly similar chemical content (~65-68 wt.% SiO₂, Samaniego
 237 46 47 et al., 2015), similar to the brecciated lava domes. A progressive decrease in block-size is observed with
 238 48 49 distance. Large blocks (~0.5-1 m in diameter) are occasional. The few distal blocks (>1 m in length)
 239 50 51 surrounded by P-PDC unit are associated to the underlying avalanche deposit.

240 52

241 53

241 54 4.3. The syn-emplacement block lithofacies

242 55

242 56

243 57 58 Using the Google Earth imagery, we differentiate different block lithofacies from proximal to distal zones.

244 59 60 The eastern flank collapse of the Tutupaca volcano shows at the summit two brecciated zones related to lava
 245 61 62 dome collapse (domes V to VII in Fig. 3B, Fig. 4A). We observe along the East crest (1 in Fig. 4A) angular

245 63

245 64

245 65

246 dome fragments adjacent to the PDC (in red in Figs. 3A and 4A) without preferential orientation, and on the
 247 1 west side (2 in Fig. 4A) an impacted and crushed zone showing imbricated block clusters with tabular planar
 248 2 surfaces. The long axis of 56 blocks are tilted N112E. In the median zone, block ridge structures show an
 249 4 isolated polyhedral block (white arrow in Fig. 4B), which exhibits planar surfaces with angular edges. We
 250 6 observe in downstream sigmoid fish of clasts, which appears disaggregated and truncated in N40E, related to
 251 8 the interactions between avalanche and the blast-generated the PDC (Fig. 4B). The isolated distal blocks (>1
 252 10 m in length, Fig. 4C) surrounded by P-PDC unit are transverse with extensional lateral spreading (N176E,
 253 12 Fig. 4C).

254 13 The textural and sedimentological variations of the block avalanche lithofacies (HA-DAD and DR-DAD) are
 255 15 described with associated volcanic deposits to correlate *syn*-emplacement process between volcanic debris-
 256 17 avalanche units and pyroclastic density current deposits.

257 19 258 21 259 23 5. Results

260 24
261 26 The SPO analysis of the block lithofacies contribute to a semi-quantitative description of block deposits. The
 262 28 comparison of each block lithofacies with cumulative curves and fractal distributions helps to distinguish the
 263 30 deposits. The analysis of the block shapes has enabled us to identify the inherited structures and the
 264 32 relationships between the proximal and distal block clusters.

265 33 266 35 5.1. Block lithofacies

267 37
268 39 In the Paipatja DAD, we have observed block clusters and block avalanche lithofacies with a specific
 269 41 distribution on and between blocks. From proximal to distal zones, the block characteristics were quantified
 270 43 using the software ImageJ and SPO analysis (>400 blocks, Launeau and Robin, 2005). We characterized the
 271 45 localized mesoscale structures observed on few blocks associated with the ridged structures.

272 46 273 48 5.1.1. Block clusters lithofacies of DR-DAD

274 50 Imbricated block clusters are localized under the collapse scar (A in Figs. 3A and 4A). The dacitic dome
 275 52 fragments (from centimeters to several meters in size) present similar chemical characteristics (64.5-65.9 wt.
 276 54 % SiO₂, Samaniego et al., 2015). We observed impacted blocks with planar fractures and undulated borders
 277 56 (Fig. 5A), and tilted blocks in imbricated piles. Inherited clasts are observed with jigsaw-fractured breccias
 278 58 showing polymodal distribution of the clasts and ellipse/ a/b = 5.1 (Fig. 5B). Block-rich ridge structures of the
 279 59 Paipatja DAD (B in Fig. 3A) contain abraded and sub-rounded blocks, which are also found in the underlying
 280 61 avalanche deposit and P-PDC (ellipse/ a/b = 2.3-2.6 in Fig. 5C). There are also impacted blocks (Fig. 5D)

281 showing polymodal distribution of the clasts. In the Paipatja plain, abraded and sub-rounded blocks are
 282 ¹ found isolated at the front of P-PDC (Fig. 3). Along the lateral levee, in the proximal zone, we have observed
 283 ² large blocks with sigmoidal jigsaw-breccias (Fig. 5E) and a bimodal clast distribution. Angular lava blocks
 284 ⁴ ⁵ (~1 m in length) are impacted between aligned and subdued blocks (Fig. 5F), which exhibit planar surface
 285 ⁶ ⁷ with conchoidal fractures or abraded surface with striations. We differentiate block clusters and ridged
 286 ⁸ ⁹ avalanche units (ellipse/ a/b = 2.3-2.5, DR-DAD, Fig. 5G) from imbricated block clusters (ellipse/ a/b = 1.74)
 287 ¹⁰ and subdued and tilted blocks in the distal zone (ellipse/ a/b ~2.12, PDC, Fig. 5H).

289 ¹³ 5.1.2. Block avalanche lithofacies

290 ¹⁵ Some transverse blocks appear isolated or aligned in N30° (DR-DAD, Figs. 3B and 6A), parallel to the
 291 ¹⁷ ¹⁸ elongated depressions. We observed sub-rounded faces with striations in upstream and planar faces with
 292 ¹⁹ ²⁰ conchoidal fractures in downstream. Along the lateral levee, we described quenched and cracked surfaces in
 293 ²¹ the upper part with jigsaw-fit texture and imbricated subangular clasts along basal contact of blocks (Fig.
 294 ²² ²³ 6B). A large polyhedral block (~3 m high and ~5 m length, HA-DAD, Fig. 6C) on the ridge crest presents an
 295 ²⁴ ²⁵ oriented abrasion: sub-rounded face in the front and planar face in the downstream. In the PDC deposits, a
 296 ²⁶ ²⁷ bimodal distribution of the surrounded clasts is quantified. The sub-rounded lava block displays two distinct
 297 ²⁸ ²⁹ surfaces: a quenched and cracked surface in the upper part and an altered vitreous phase in the lower part. A
 298 ³⁰ ³¹ distal sub-rounded block, surrounded by the P-PDC deposits, appears isolated (Fig. 6D) with bimodal
 299 ³² ³³ distribution of the surrounded clasts related to the PDC deposits. Subdued blocks exhibit abraded surfaces
 300 ³⁴ with striations.

302 ³⁷ 5.1.3. Grooves and striations

303 ³⁹ ⁴⁰ At 5.5 km from the collapse scar, a few blocks associated with the ridge structures (Fig. 7A; Valderrama et
 304 ⁴¹ ⁴² al., 2016) exhibit grooves and striations with roughly circular depressions on the upstream, abraded face.
 305 ⁴³ ⁴⁴ These localized mesoscale structures are often irregular and grouped in the lower part of the abraded and
 306 ⁴⁵ ⁴⁶ striated surfaces. The largest striations (>3 cm wide) are parallel to each other (at 3.19°, Fig. 7) and observed
 307 ⁴⁷ ⁴⁸ in the upper part of the block face. There are small striations perpendicular to the grooves (Fig. 7B). Grooves
 308 ⁴⁹ ⁵⁰ or furrows 1-5 cm depth ranged from roughly circular (<5 cm in diameter) to elliptic (~8-15 cm for longest
 309 ⁵¹ ⁵² axis) in shape. Fractal D values, calculated from exponent h of power regressions (100 striations, Table 4;
 310 ⁵³ ⁵⁴ Suzuki-Kamata et al., 2009), are 1.09 in the 8.4-46.4 cm mark-size range.

311 ⁵⁴ ⁵⁵ The macroscopic characteristics of grooves and striations with circular depressions were used for the shape
 312 ⁵⁶ ⁵⁷ analysis with the software ImageJ and SPO analysis (566 mesoscale structures, Launeau and Robin, 2005).
 313 ⁵⁸ ⁵⁹ Grooves and striations show polymodal distributions, with ellipse/ a/b around ~5.1-5.9 (Fig. 7A-B). In the
 314 ⁶⁰ ⁶¹ lower part of the block face, basal striations (~2-3 mm wide) with perpendicular diaclasis are differentiated.
 315 ⁶² ⁶³ Fractal D values, calculated from exponent h of power regressions (90 striations, Table 4, Suzuki-Kamata et
 316 ⁶⁴ ⁶⁵

316 al., 2009), are 0.67 in the 5.2-20.96 cm mark-size range.

317 1
318 2
319 4 5.2. *Sedimentary characteristics of block lithofacies*

320 6
321 8 Sedimentary characteristics of block lithofacies were compared with fractal D values to distinguish textures
322 9 in the block avalanche units (HA-DAD, DR-DAD) and PDC deposits from proximal to distal zones. Block
323 10 lithofacies of HA-DAD are hydrothermalized and cataclased with jigsaw-cracks. These are angular to
324 11 subangular in PDC (20-30% of HA-DAD, [Samaniego et al., 2015](#)). We differentiate imbricated blocks with
325 12 jigsaw structures in zones A and C ([Fig. 3A](#)), the abraded and subdued blocks observed in ridges structures
326 13 and the distal zone (F in [Fig. 3A](#)), and the dacitic block lithofacies in zones D and E. The cumulative curves
327 14 of block-size distributions *vs.* a/b are compared to distinguish block lithofacies in different zones, which are
328 15 characterized by five logarithmic regressions (Eqs. 5-9 with $R^2 > 0.9$ in [Fig. 8A](#)). These are compared to the
329 16 logarithmic regressions of the impact breccias in French Massif Central (Eq. 12 in [Fig. 8A](#); [Mont Dore](#),
330 17 [Bernard and van Wyk de Vries, 2017](#)). The intersecting points a to d with a/b between 2.5 and 4.7 imply a co-
331 18 evolution between the grooves and striations (Eqs. 10-11 with $R^2 > 0.9$ in [Fig. 8A](#)) and the ridged debris-
332 19 avalanche unit (Eq. 6), in accordance with the field observations. We differentiated the hydrothermalized
333 20 matrix (HA-DAD) from the breccia matrix (DR-DAD) showing sandy-gravel lithofacies of the red matrix
334 21 with few angular clasts ($< \text{cm}$, [Bernard, 2015](#); [Valderrama et al., 2016](#)).

335 22 The effect of cataclasis is shown by a decrease in the content of the smallest fractions ($< 100 \text{ cm}$, [Fig. 8B](#)) of
336 23 block lithofacies ($< 18\%$), an increase in the striation ratio (25 to 45%), together with a concomitant high ratio
337 24 in amount of block clusters (~ 20 to 40%). The variations of these data are correlated with different structural
338 25 units from proximal to distal zones. The basal striations appear differentiated ([Table 4](#)). A specific clast-size
339 26 fractal distribution is calculated in the range between 6.7 and 539 cm. The mean fractal D value, calculated
340 27 from exponent h of power regressions, is around ~ 1.28 in the 11.4-40.3 cm clast-size range ([Table 4](#); see
341 28 [Supplemental File 1](#); [Suzuki-Kamata et al., 2009](#)). The distal block lithofacies present the highest D values
342 29 around ~ 1.83 compared to the proximal ridged deposits around ~ 1.64 . These are differentiated from the
343 30 surrounded matrix between 0.64 and 2.84 in the 0.0016-6.4 clast-size range. The mean fractal D value of
344 31 striations is around ~ 0.62 in a range from 5.9 to 44.6 cm.

345 32
346 33 5.3. *Block shape parameters*

347 34
348 35 Shape analysis using the software ImageJ and SPO analysis (404 blocks from the HA-DAD and DR-DAD,
349 36 635 striations; [Launeau and Robin, 2005](#); [Blott and Pye, 2008](#); [Crawford and Mortensen, 2009](#)) has been
350 37 applied to compare shape parameters of blocks from proximal to distal zones, together with striations and

351 38
352 39
353 40
354 41
355 42
356 43
357 44
358 45
359 46
360 47
361 48
362 49
363 50
364 51
365 52

351 grooves in blocks. This comparison is intended to characterize the cataclastic evolution with co-genetic
 352 1 relationships between volcanic debris-avalanche units and P-PDC, including the inherited clast shape for lava
 353 2 blocks. The mean values of a/b ratio and ellipse ($\sim 1.7 \pm 0.03$ and 3.5 ± 0.15 , Table 5) are different from the
 354 3 clasts observed in the matrix of ridged units (DR-DAD, $\sim 1.69 \pm 0.05$ and 2.72 ± 0.09 , 1891 clasts from SPO
 355 4 analysis, Bernard, 2015). The calculated standard errors indicate the measurement errors and the sum of
 356 5 internal variability between the block shape parameters. These values imply distinct evolution between the
 357 6 avalanche block lithofacies and PDC.

358 7 5.3.1. Avalanche block lithofacies

360 8 We distinguish an inherited clast shape for lava blocks with $a/b = 0.9$ and ellipse = -3.5 implying textural
 361 9 relationships between the block lithofacies of HA-DAD and DR-DAD. Three regressions characterize the
 362 10 roundness vs. maximum Feret's diameter (Eqs. 13-17 in Fig. 9) for the block lithofacies. Two regressions
 363 11 (Eqs. 14-15 in Fig. 9) characterize the block lithofacies observed in the proximal and median zones. These
 364 12 values are compared to the breccias forming the ridged avalanche matrix (HA-DAD and DR-DAD) and the
 365 13 distal lobe of the Pichu Pichu debris-avalanche deposit (Eqs. 14-15 and 17 in Fig. 9; Bernard, 2015).

366 14 5.3.2. Distal block lithofacies

367 15 Three points of intersection indicate similar values of roundness for different zones of cataclasis ($a-c$ in Fig.
 368 16 9A). We distinguish an inherited clast shape with roundness around ~ 0.9 (a , Fig. 9), indicating textural
 369 17 relationships between the tilted distal blocks (PDC) and the blocks from the ridges, close to those of the
 370 18 sheared lava breccias in the distal lobe of the Pichu Pichu debris-avalanche deposit. The intersecting points b
 371 19 and c with roundness between 1.05 and 1.08 imply a co-evolution between the impacted blocks (Eq. 14)
 372 20 observed in the proximal and distal zones and the sheared sigmoid along the lateral levee (Eq. 15 in Fig. 9).

373 21 5.3.3. Grooves and striations

374 22 The values of $a/b = 3.2$ and ellipse = 15 are correlated to a co-genetic evolution between the grooves and
 375 23 striations, the blocks from ridges and the distal, impacted blocks (PDC). The mean values increase for
 376 24 roundness from 1 to 1.7 and ellipse/ a/b from 0.2 to 2.7 (Table 5), while the values of Riley's circularity
 377 25 decrease. A regression characterizes the roundness vs. maximum Feret's diameter (Eq. 13 in Fig. 9) for the
 378 26 striations. The intersecting point c (Eqs. 13-14 in Fig. 9) with Feret's diameter < 0.05 m and roundness around
 379 27 ~ 1.05 characterizes the inherited clast shape of the proximal block lithofacies generating striations and
 380 28 impact marks in the ridged debris-avalanche unit. We observed decreasing values of Riley's circularity related
 381 29 to Feret's diameter (Table 5).

382 30 5.4. Block clusters and shape variations

383 31
 384 32
 385 33
 386 34
 387 35

386

387 More than six cluster structures have been described with the shape analysis using the software ImageJ and
 388 SPO analysis from 312 blocks in the unconsolidated avalanche matrix from the HA-DAD (Fig. 10). Lava
 389 block clusters (~30-70 vol.%) from 40 cm to 5 m in diameter are impacted and thrust in unconsolidated
 390 avalanche matrix. The a/b ratio related to ellipse values show increasing values for the impacted jigsaw-
 391 clusters; and for the tilted block in the distal zone. Similar characteristics appear for the striated blocks from
 392 the ridges and the distal clusters. Similar ellipse values are calculated between proximal jigsaw breccias and
 393 the tilted and impacted blocks in the distal zone (ellipse = 0.7); between distal clusters (ellipse = 1-1.8) or
 394 between tilted blocks in the distal zone (ellipse = 2.7). *Syn-cataclastic* emplacement of block clusters with a
 395 co-genetic evolution of shape parameters may be envisaged.

396 The **roundness** is high (>1) for the block clusters, close to those of the experimental crushed stones (Janoo,
 397 1998). Four regressions characterize the **roundness** vs. Feret's **diameter** (Eqs. 18-21 in Fig. 10) between 0.05
 398 and 1 m. The increasing macro-**roundness** reflects the effects of clast crushing due to the collisional transport
 399 and cataclastic sorting between the proximal and distal zones. We have highlighted a power regression for the
 400 imbricated block clusters in the proximal zone with **roundness** >1 (Eq. 18 in Fig. 10). Two categories of
 401 regressions are identified for the impacted and tilted block clusters in the distal zone with **roundness** between
 402 0.9 and 1.08 (Eqs. 19-20 in Fig. 10). Three points of intersection ($a-c$ in Fig. 10) indicate similar values of
 403 block **roundness** for cluster structures characterized by different regressions: between impacted and tilted
 404 blocks in distal zone ($a = 1.05$, Eqs. 19-20); between distal clusters and the striated blocks from the ridges (b
 405 ~1, Eqs. 18-20) or proximal breccias with jigsaw features. We distinguish an inherited block shape for lava
 406 blocks with **roundness** around ~0.9 and Feret's **diameter** = 0.05 m (c in Fig. 10), implying textural
 407 relationships between these block clusters and sheared contact of the Pichu Pichu volcanic debris-avalanche
 408 deposit.

409 The Riley's circularity of block clusters shows decreasing values from the proximal to distal zones (Table 5,
 410 see Supplemental File 2) related to Feret's diameter, implying textural relationships between the block
 411 clusters with the run-out distance.

412

413

414 6. Discussion

415

416 From field observations, we used complementary methods to describe surface and internal structures of the
 417 Paipatja volcanic debris-avalanche deposits of the Tutupaca volcano and the associated pyroclastic density
 418 currents. The quantitative sedimentary analysis contributes to correlate the block clusters, the block
 419 avalanche lithofacies and mesoscale structures with different stages of cataclastic flow regime between the
 420 DR-DAD and the associated pyroclastic density currents from proximal to distal zones. Quantitative

421

422

423

421 morphological and sedimentological parameters are correlated and compared to other avalanche deposits
 422 worldwide, showing that the brecciation have recorded the collisional interactions between lava dome sector
 423 collapse and pyroclastic density currents.

424 425 6.1. Classification of volcanic debris-avalanche deposits

426
427 The volcanic debris avalanche deposits are commonly associated with PDC. The area and volume of the
 428 volcanic debris avalanche deposits associated with PDC are compared to Bezymianny eruptive sequence
 429 (Siebert et al., 1987) showing lava dome collapses with hydrothermally alteration interacted with the blast-
 430 generated the PDC (Fig. 2): Mount Saint Helens in the USA (Glicken, 1986), Bezymianni in Kamchatka
 431 (Siebert et al., 1987), Soufrière in Guadeloupe (Boudon et al., 1984). A relationship between the area (A) and
 432 volume (V) for the Tutupaca units is compared to the power regressions of other volcanic debris-avalanche
 433 deposits such as Mount Shasta and Mount Saint Helens in the USA (Fig. 2, Glicken, 1986; Siebert et al.,
 434 1987; Legros, 2002). The fault breccias have recorded the propagation of impact waves. The Tutupaca
 435 volcanic debris-avalanche deposits with H/L around $\sim 0.15-0.2$ ($12-13 \text{ km}^2$, $<1 \text{ km}^3$, $L = 6-8 \text{ km}$, Samaniego
 436 et al., 2015; Valderrama et al., 2016) show different units characterized by granular segregation and fingering
 437 instabilities (Figs. 3-4, Valderrama et al., 2018). A power regression (Eq. 2 in Fig. 2) characterizes the
 438 Tutupaca units compared to the proximal scar of the Mount Saint Helens deposits showing striations of the
 439 bedrock and the impacted distal zone in French Massif Central. This co-evolution of geomorphological
 440 parameters may be related to digitate shape of the avalanche deposits (Samaniego et al., 2015). The largest
 441 volcanic avalanche deposits (Mount Shasta, Legros, 2002) appears different from other volcanic debris-
 442 avalanche deposits in accordance with field observations, on ridge structures, striations, and block clusters.
 443 The geomorphological parameters of the largest avalanche units tend toward similar values (Eqs. 1-4 in Fig.
 444 2). We differentiate the intersecting point A (Fig. 2) with an area around ~ 140 and 180 km^2 and volume
 445 between 5 and 7 km^3 , implying a convergent evolution between the largest structural units with run-out
 446 distance of over 22 km (Mount Saint Helens in the USA and Parinacota in Chili, Fig. 2; Siebert and Roverato,
 447 2020) and the high velocity of volcanic debris avalanche associated with the blast lateral collapse and
 448 fluidization.

449 For the Tutupaca volcanic debris-avalanche deposits, the mean values of a/b ratio and ellipse, around ~ 1.7
 450 and ~ 3.5 respectively (Table 5) are between the Rio Chili, tilted block-rich debris-avalanche deposits in Peru
 451 and the lateral levee from the Mont Dore in French Massif Central (Bernard, 2015; Bernard et al., 2017). The
 452 mean ellipse/ a/b values around 1.88 characterize the crushing effects (Table 5, Bernard et al., 2019). We
 453 differentiate the thermal effect of fragmentation in proximal zone with ellipse/ a/b between 0.23 and 1.7 and
 454 the transfer of the plane collapse in the median zone showing ridge structures (ellipse/ $a/b = 2.04-2.78$). For
 455 the Tutupaca example, we have a dome collapse with a cataclastic gradient and a granular segregation during

456 a lateral spreading over ~1 km (Fig. 3). These statistical comparisons with other volcanic debris-avalanche
 457 1 units contribute to establish a geomorphological classification of the volcanic debris-avalanche deposits
 458 2 related to kinematic process. Secondary reworking of the Paipatja volcanic debris-avalanche deposits with
 459 3 impact waves and fingering instabilities during flow propagation of the pyroclastic density current must be
 460 4 considered. Successive collapses of the volcanic edifice contribute to the discontinuous units of the debris-
 461 5 avalanche deposits.

462 6
 463 7
 464 8
 465 9
 466 10
 467 11
 468 12
 469 13
 470 14
 471 15
 472 16
 473 17
 474 18
 475 19
 476 20
 477 21
 478 22
 479 23
 480 24
 481 25
 482 26
 483 27
 484 28
 485 29
 486 30
 487 31
 488 32
 489 33
 490 34
 491 35
 492 36
 493 37
 494 38
 495 39
 496 40
 497 41
 498 42
 499 43
 500 44
 501 45
 502 46
 503 47
 504 48
 505 49
 506 50
 507 51
 508 52
 509 53
 510 54
 511 55
 512 56
 513 57
 514 58
 515 59
 516 60
 517 61
 518 62
 519 63
 520 64
 521 65

6.2. Granular flow regime between the debris avalanche and pyroclastic density currents

Field observations show a reverse grading of the lithofacies assemblage (Socompa, van Wyk de Vries et al.,
 2001; Davies et al., 2010): the HA-DAD is overlain by the DR-DAD interstratified with pyroclastic density
 current deposits (Samaniego et al., 2015). A similar block-size distribution of the avalanche deposits and the
 regressions (Eqs. 5-12 in Fig. 8) indicate a similar cataclastic origin with a co-genetic evolution of block
 lithofacies linked with a sequential *syn*-cataclastic emplacement (Samaniego et al., 2015; Valderrama et al.,
 2016).

The comparison of each block size-fractions with cumulative curves and histograms (Figs. 8-10) help to
 identify the block lithofacies from proximal impact and cataclastic gradient with granular segregation in
 flowing mass (Valderrama et al., 2016). Sedimentary parameters show a co-genetic brecciation of block
 lithofacies (Eqs. 5-12, Fig. 8), which are compared to the impact breccia in French Massif Central. The lava
 dome brecciations have recorded the propagation of impact waves. The *roundness* vs. Feret's *diameter*
 suggests a co-genetic evolution between the proximal clusters, the abraded and striated blocks in the ridges
 and the distal block clusters (Eqs. 19-22 in Fig. 10A) due to differentiated breakage during collisional
 transport.

6.2.1. Cyclic impact waves and block clusters

The dome collapse with explosion is associated with a specific granular flow regime between avalanche and
 pyroclastic density currents with secondary reworking. The succession of slide blocks is associated to frontal
 propagation of cyclic impact wave in an extensional context during primary shear propagation generating a
 clastic matrix (PDC, Mount Saint Helens, Glicken, 1986). Inherited jigsaw-fit textures have recorded the
 initial dilation of the collapsed edifice (Mount Saint Helens, Glicken, 1986). The inherited shapes of the
 block lithofacies ($a/b = 1.2-2$, ellipse = 0.2-2.5) indicate the reworking by impact waves. Imbricated block
 clusters with jigsaw-fit texture and planar fractures are impacted under the collapse scar (A in Figs. 3A and
 4A). Proximal imbricated block clusters may be generated during impact waves (Cox et al., 2019). Cyclic
 impact waves and initial dilation contribute to block cluster growth with jigsaw-fit texture during the first
 stage of avalanche emplacement. Clusters are disaggregated during shock propagation (Fig. 4A). The rock

491 fragmentation during the proximal impact wave increases the **roundness** (>1 , Fig. 10; Szabo et al., 2015). The
 492 1 propagation of the impact wave with granular oscillatory stress (Bernard and van Wyk de Vries, 2017; Cox et
 493 2 al., 2019) may contribute to produce the imbricated block clusters. Waves during cyclic impact may be
 494 3 considered to cause block cluster growth.

495 4 Blocks are split into clusters of smaller aggregates during transport (Palmer et al., 1991). Stick-slip
 496 5 oscillations (Sandnes et al., 2011) and an oscillatory relative speed may be considered during impact waves
 497 6 and dilation, which change the apparent coefficient of friction in the proximal zone. The isolated sub-rounded
 498 7 blocks and impacted blocks ($D \sim 1.64-2.83$ and ellipse/ $a/b = 1.7-1.8$, Tables 4 and 5) may be related to cluster
 499 8 disaggregation (Fig. 8B) during shock propagation generating the polymodal clast distributions with a thinner
 500 9 clastic matrix related to polymodal striations of the blocks from the ridges (ellipse/ $a/b = 1.7-1.8$, Eqs. 9-12,
 501 10 Fig. 8, Table 5). The cataclastic finer fractions increase the particle-to-particle interactions during flow
 502 11 propagation (Dennen et al., 2014) generating grooves and striations on the abraded surface of the impacted
 503 12 blocks. Textural relationships appear between proximal blocks and the striated blocks from the ridges (Table
 504 13 5) with decreasing values of Riley's circularity.

505 14 6.2.2. An upper collisional regime

506 15 Differentiated velocities related to transitional regime must be considered between the matrix-rich facies and
 507 16 the block facies ($v_1 < v_2$; Glicken, 1998; Caballero and Capra, 2011). Formation of the elongated ridges is
 508 17 attributed to granular segregation and differential block velocities in the flowing mass (Dufresne and Davies,
 509 18 2009). The bimodal clast distributions in the medial zone (ellipse/ $a/b \sim 1.7$) differentiate the transverse
 510 19 blocks, the elongated ridges and lateral levee with sigmoidal jigsaw-breccias (Fig. 6B-D). The DR-DAD
 511 20 lithofacies contribute to decreasing run-out velocity with localized secondary flow (Socompa, Kelfoun et al.,
 512 21 2008; Mont Dore in French Massif Central, Bernard and van Wyk de Vries, 2017) and segregation waves to
 513 22 the flow front (Gray, 2013).

514 23 A multidirectional switch of mass spreading may be considered, with segregation waves to the flow front
 515 24 (Glicken, 1998). Transverse orientations of blocks in the medial zone implicate a quick stop attributed to a
 516 25 compressive context. The lack of propagation of the proximal conditions contribute to plug flow and granular
 517 26 segregation, generating lateral levees and ridges in the upper collisional flow regime for the median zone
 518 27 (Shea and van Wyk de Vries, 2008; Valderrama et al., 2016). Along lateral levee, rafted blocks with sigmoidal
 519 28 jigsaw-breccias are related to transport by traction in shearing context, generating secondary fractures.

520 29 We differentiate the parent dome volcanic processes from the breakage due to collisional transport, which
 521 30 increases the **roundness** from 1 to 1.7, related to the frontal reworking by impact wave (Table 5). An upper
 522 31 collisional regime for block lithofacies generating impact marks is differentiated from basal frictional regime
 523 32 with striations (e.g. Parinacota and Ollagüe in Chile, Clavero et al., 2002, Clavero et al., 2004; El Zagan,
 524 33 Mexico, Caballero and Capra, 2011). Collisional abrasion may be associated with the dispersive pressure

526 generated by the subsequent pyroclastic density current. Shock and brecciation of blocks limit the mixture of
527 1 lithofacies (*e.g.* Pichu Pichu in Peru, [Legros et al., 2000](#); El Zagan, Mexico, [Caballero and Capra, 2011](#)).
528 2 Stick-slip motion at the front of lobe and high-speed of blocks may also be considered ([Bartali et al., 2015](#)).
529 3 Each of the block avalanche deposits and striations present a specific regression for the **roundness** vs. Feret's
530 4 **diameter** diagram (Eqs. 13-17 with $R^2 > 0.5$ in [Fig. 9](#)), implying a differentiated evolution of the breakage
531 5 during collisional transport and granular segregation. Inherited clast shapes with **roundness** between 0.9 and
532 6 1.2 are related to a same cataclastic origin. The impact of clasts onto block surfaces ($r = 0.5a^2/h$, [Clavero et](#)
533 7 [al., 2002](#)) can be approximated with $a < 5$ cm radius of hemispherical damage zone, and $h \sim 1-5$ cm distance
534 8 that penetrated into the block. Calculated r values between 2.5 and 12.5 cm is in accordance with the
535 9 surrounded clasts. The impact force F has a value of about 15.7×10^{10} N by using $F = \Pi a^2 \rho_0$ with a typical
536 10 ρ_0 value around $\sim 2.10^9$ Pa ([Clavero et al., 2002](#)). The clast velocity for making impact marks can be
537 11 estimated around ~ 8.86 m.s⁻¹ by using $V = (0.5 \Pi \rho_0 / Mr)^{1/2} a^2$ with $M \sim 10^3$ kg, $a < 5$ cm and r values between
538 12 2.5 and 12.5 cm ([Clavero et al., 2002](#)), in accordance with impact marks analysis on clast faces of Panum
539 13 block lithofacies (Mono Craters, CA, [Dennen et al., 2014](#)). The avalanche velocity in the middle zone
540 14 (around ~ 3 and 6 km from source, [Clavero et al., 2002](#)) is considered between 15.5 and 39.6 m.s⁻¹ by using v
541 15 $= (2gH)^{1/2}$. Localized striations and grooves can be attributed to the peak velocity at the flow front. The
542 16 inherited shapes of the lava blocks and the co-genetic evolution between the blocks from the ridges and
543 17 striations may be associated to secondary fracturing with partial decompression during run-out propagation
544 18 ([Bernard et al., 2019](#)).

545 19 The dome collapse is associated with a specific granular flow regime between avalanche and pyroclastic
546 20 density currents: cyclic impact waves with disaggregation during shock propagation, and secondary flow
547 21 with segregation waves. Basal frictional regime with striations is differentiated from higher collisional and
548 22 cataclastic flow regime generating clast breakage and impact marks (*e.g.* Parinacota and Ollagüe in Chile,
549 23 [Clavero et al., 2002](#), [Clavero et al., 2004](#); El Zagan, Mexico, [Caballero and Capra, 2011](#)).

550 24

551 25 6.3. The frontal reworking

552 26
553 27 Logarithmic regressions of the abraded and sub-rounded block lithofacies in the median and distal zones (d
554 28 $\sim 1.64-1.83$; ellipse/ $a/b \sim 2.7$, Eqs. 7-11 in [Fig. 8A](#)) are close to those of the impact breccias along avalanche
555 29 fault zone in French Massif Central (Eq. 12 in [Fig. 8A](#), [Bernard and van Wyk de Vries, 2017](#)). The Riley's
556 30 circularity ([Table 5](#), see [Supplemental File 2](#)) shows that the polyhedral blocks with conchoidal fractures and
557 31 striations of the ridge structures differentiated from sub-rounded blocks in the distal zone. These may be
558 32 associated to an oriented abrasion and thermal shock generating tilted blocks with cracked surface. The clast
559 33 breakage with striations due to collisional transport decreases the Riley's circularity ([Table 5](#)). These block
560 34 lithofacies may be associated to crushing impact with frictional temperature during oscillatory stress

561 35
562 36
563 37
564 38
565 39

561 (Bernard and van Wyk de Vries, 2017) related to decompression in rotational shearing, and matrix
 562 1 segregation.

563 2 The inherited shapes of the blocks ($a/b = 1.2-2$; ellipse = 0.2-2.5; Riley's circularity ~ 0.6 in Table 5; Eq. 14
 564 3 and $a \sim 0.9$ in Fig. 9) implied the reworking by impact wave (Cox et al., 2019) and similar processes of
 565 4 abrasion between the imbricated block clusters in the proximal zone, the striated blocks from ridges and the
 566 5 tilted distal blocks. These are close to those of the sheared lava breccias observed along the Pichu Pichu
 567 6 debris-avalanche deposit. Flow traction may contribute to block piles (Cox et al., 2019) up to a point where
 568 7 flows are not competent. Fractal D -values of the surrounded matrix between 0.6 and 2.8 are associated to an
 569 8 extensional disaggregation and granular transport (Table 4, Blekinsop and Fernandes, 2000). A *syn*-
 570 9 cataclastic emplacement of the blocks with a co-genetic evolution is differentiated between the proximal and
 571 10 median zones and between the striated blocks from ridges and the distal, impacted blocks.

572 11 573 12 7. Conclusions

574 13 Field observations together with quantitative sedimentological analyses help to characterize textural
 575 14 variations of the Paipatja avalanche deposits and the associated pyroclastic density current deposits from
 576 15 Tutupaca volcano in southern Peru. A typical lithofacies assemblage with a reverse grading shows jigsaw
 577 16 breccias, impacted block clusters and striations associated with the interaction between the debris avalanche
 578 17 and the subsequent pyroclastic density currents.

580 18 Cyclic impact waves and initial dilation of the Tutupaca lava dome have contributed to produce jigsaw
 581 19 breccias and imbricated block clusters during the first stage of avalanche emplacement. Cluster
 582 20 disaggregation during shock propagation contribute to an upper collisional regime, generating isolated blocks
 583 21 with striations. Transverse blocks, lateral levee and ridges are associated to a switch of mass spreading with
 584 22 granular segregation. The frontal reworking by impact wave with extensional disaggregation contributes to
 585 23 generate impacted block clusters in distal zone. From the statistical dataset, a few regressions have been
 586 24 established indicating the same cataclastic origin with a co-genetic evolution of block lithofacies.

587 25 Sequential events of *syn*-emplacement processes during impact waves have been established related to
 588 26 volcanic debris-avalanche units and pyroclastic density current deposits. These observations help to constrain
 589 27 the collisional shearing contact between avalanche units and associated pyroclastic density currents, and help
 590 28 to explain the block cluster growth and the block disaggregation correlated to sequential *syn*-emplacement
 591 29 processes of debris avalanche units with associated pyroclastic deposits.

592 30 The deposits at Tutupaca are exceptional for their freshness and clarity, and lack of disturbance. This area is
 593 31 an important record of lava dome collapse and debris avalanche and pyroclastic flow interaction.

594 32 595 33 Acknowledgments

596 34
597 35
598 36
599 37
600 38

596 The fieldwork in Peru trip has been funded by the “Institut de la Recherche pour le Développement” support
 597 1 (O. Roche and P. Samaniego, IRD) for Tutupaca volcano. The geoheritage context is provided through the
 598 2 UNESCO International Geosciences Program project 692, Geoheritage for Resilience.
 599 3

599 4
 600 5

600 6 **References**

601 7
 602 8
 603 9

602 10 Andrade, S.D., van Wyk de Vries, B., 2010. Structural analysis of the early stages of catastrophic strato-
 603 11 volcano flank-collapse using analogue models. *Bull. Volcanol.* 72, 771-789.

604 12 Bartali, R., Sarocchi, D., Nahmad-Molinari, Y., 2015. Stick-slip motion and high speed ejecta in
 605 13 granular avalanches detected through a multi-sensors flume. *Eng. Geol.* 195, 248-257.
 606 14

606 15 Bernard, K., 2015. Quelques aspects sédimentaires des avalanches de débris volcaniques. Ph.D.
 607 16 Thesis, Univ. Clermont-Auvergne, France (Unpub., in French). Available at: <NNT : _____

608 17 <[2015CLF22624](https://nnt.bibliotheque.univ-clermont.fr/2015CLF22624)>.<[tel-01330779](tel:01330779)>.
 609 18
 610 19

609 20 Bernard, K., van Wyk de Vries, B., 2017. Volcanic avalanche fault zone with pseudotachylite and gouge
 610 21 in French Massif Central. *J. Volcanol. Geotherm. Res.* 347, 112-135.
 611 22

611 23 Bernard, K., Thouret, J-C., van Wyk de Vries, B., 2017. Emplacement and transformations of volcanic debris
 612 24 avalanches - A case study at El Misti volcano, Peru. *J. Volcanol. Geotherm. Res.* 340, 68-91.
 613 25

613 26 Bernard, K., van Wyk de Vries, B., Thouret, J-C., 2019. Fault textures in volcanic debris-avalanche
 614 27 deposits and transformations into lahars: The Pichu Pichu thrust lobes in south Peru compared to
 615 28 worldwide avalanche deposits. *J. Volcanol. Geotherm. Res.* 371, 116-136.
 616 29

616 30 Blekinsop, T.G., Fernandes, T.R.C., 2000. Fractal characterization of particle size distributions in
 617 31 chromitites from the Great Dyke, Zimbabwe. *Pure Appl. Geophys.* 157, 505-521.
 618 32

618 33 Blott, S.J., Pye, K., 2008. Particle shape: a review and new methods of characterization and classification.
 619 34 *Sedimentology* 55, 31–63.
 620 35

620 36 Boudon, G., Semet, M.P., Vincent, P.M., 1984. Flank-failure-directed blast eruption at Soufrière,
 621 37 Guadeloupe, French West Indies: A 3000-yr-old Mt. St. Helens? *Geology* 12, 350-353.
 622 38

622 39 Caballero, L., Capra, L., 2011. Textural analysis of particles from El Zaguán debris avalanche deposit,
 623 40 Nevado de Toluca volcano, Mexico: Evidence of flow behavior during emplacement. *J. Volcanol.*
 624 41 *Geotherm. Res.* 200, 75-82.
 625 42

625 43 Clavero, J.E., Sparks, R.S.J., Huppert, H.E., 2002. Geological constraints on the emplacement mechanism
 626 44 of the Parinacota avalanche, northern Chile. *Bull. Volcanol.* 64, 40–54.
 627 45

627 46 Clavero, J.E., Polanco, E., Godoy, E., Aguilar, G., Sparks, R.S.J., van Wyk de Vries, B., Perez de Arce, C.,
 628 47 Matthews, S., 2004. Substrata influence in the transport and emplacement mechanism of the Ollagüe
 629 48 debris avalanche (northern Chile). *Acta Vulc.* 16, 59–76.
 630 49

630 50 Cox, R., O'Boyle, L., Cytrynbaum, J., 2019. Imbricated coastal boulder deposits are formed by storm
 631 51
 632 52
 633 53
 634 54
 635 55

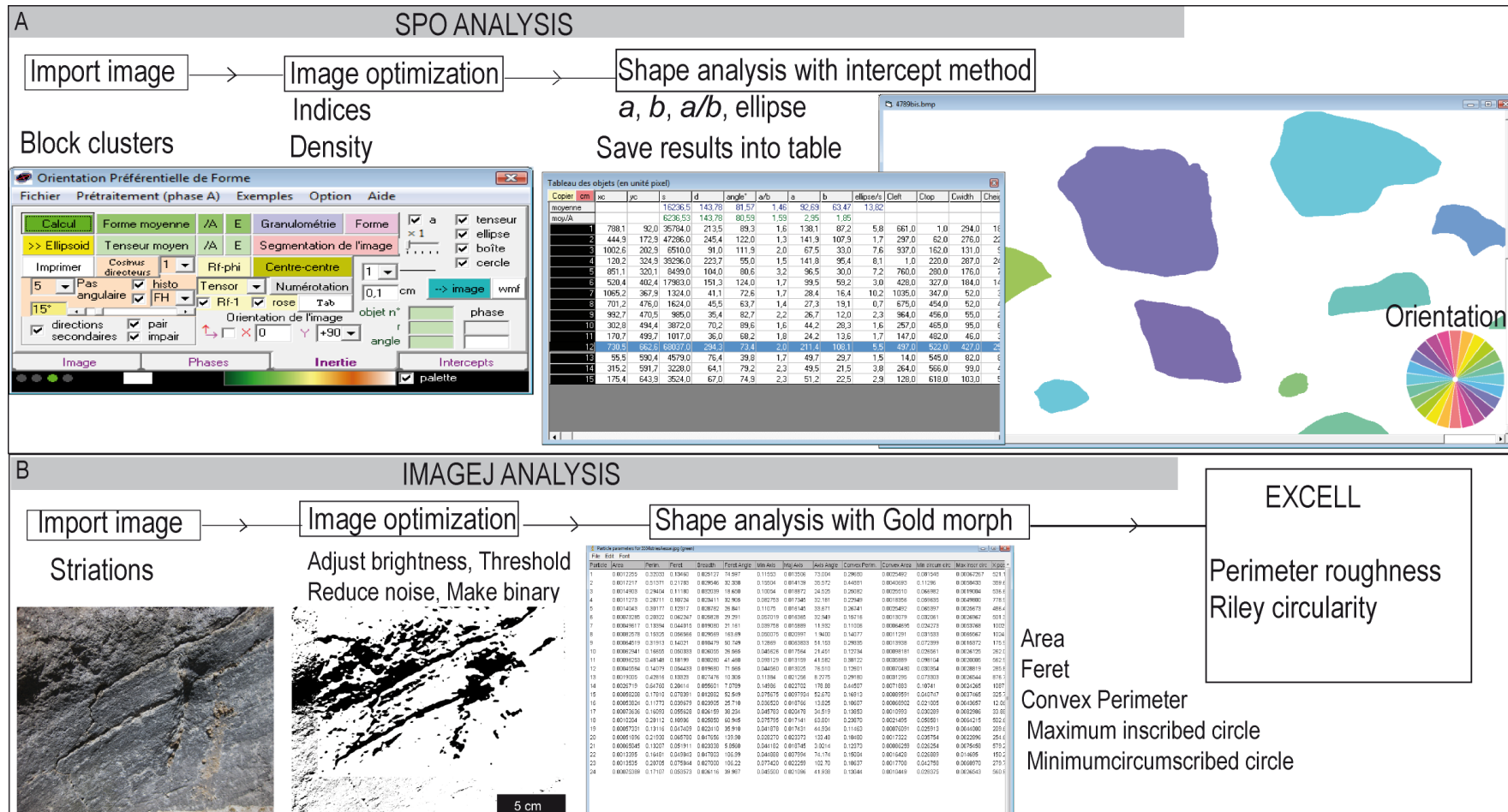
- 631 waves, and can preserve a long-term storminess record. *Sci. Rep.* 9, 10784.
- 632 1 Crandell, D.R., Miller, C.D., Glicken, H.X., Christiansen, R.L., Newhall, C.G., 1984. Catastrophic debris
633 2 avalanche from ancestral Mount Shasta volcano, California. *Geology* 12, 143-146.
- 634 4 Crawford, E., Mortensen, K., 2009. An Image J plugin for the rapid morphological characterization of
635 5 separated particle sand an initial application to placergold analysis. *Comput. Geosci.* 35, 347–359.
- 636 8 Davies, T.R., McSaveney, M.M., Kelfoun, K., 2010. Runout of the Socompa volcanic debris avalanche,
637 9 Chile: a mechanical explanation for low basal shear resistance. *Bull. Volcanol.* 72, 933-944.
- 638 11 Dennen, R.L., Bursik, M.I., Roche, O., 2014. Dome collapse mechanisms and block-and-ash flow
639 12 emplacement dynamics inferred from deposit and impact mark analysis, Mono Craters, CA.
640 13 *J. Volcanol. Geotherm. Res.* 276, 1-9.
- 641 15 Dufresne, A., Davies, T., 2009. Longitudinal ridges in mass movement deposits. *Geomorphology* 105, 171-
642 16 181. DOI:10.1016/j.geomorph.2008.09.009.
- 643 17 Glicken, H., 1986. Rockslide-debris avalanche of May 18, 1980, Mount Saint Helens Volcano,
644 18 Washington. Ph.D. Thesis, Univ. Calif. Santa Barbara, p. 303.
- 645 20 Glicken, H., 1998. Rockslide-debris avalanche of May 18, 1980, Mount St. Helens Volcano, Washington
646 21 *Bull. Geol. Surv. Jpn.* 49, 55-106.
- 647 23 Gray, J.M.N.T., 2013. A hierarchy of particle-size segregation models: from polydisperse mixture
648 24 to depth-averaged theories. *AIP Conf. Proc.*, 1542, 66-73.
- 649 26 Guilbaud, M-N., Chedeville, C., Molina-Guadarrama, A-N., Siebe, C., 2022. Volcano-sedimentary
650 27 processes at Las Derrumbadas rhyolitic twin domes, Serdan-Oriental Basin, Eastern Trans-
651 28 mexican Volcanic Belt. *Geol. Soc. Spec. Publ.*, 520, 31.
- 652 30 Janoo, V., 1998. Quantification of Shape, Angularity, and Surface Texture of Base Course Materials.
653 31 U.S. Army Corps of Engineers, Cold Regions Research & Engineering Laboratory, Hanover NH,
654 32 pp. 1-22 (Special Report).
- 655 34 Kelfoun, K., Druitt, T., van Wyk de Vries, B., Guilbaud, M-N., 2008. Topographic reflection of the
656 35 Socompa debris avalanche, Chile. *Bull. Volcanol.* 70, 1169-1187.
- 657 37 Launeau, P., Robin, Y.F., 2005. Determination of fabric and strain ellipsoids from measured sectional
658 38 ellipses - Implementation and applications. *J. Struct. Geol.* 27, 2223-2233.
- 659 40 Legros, J.F., Cantagrel, J.M., Devouard, B., 2000. Pseudotachylite (Frictionite) at the base of
660 41 the Arequipa Volcanic landslide (Peru): Implications for emplacement mechanisms. *J.*
661 42 *Geol.* 108, 601-611.
- 662 44 Legros, J.F., 2002. The mobility of long-runout landslides. *Eng. Geol.* 63, 301–331.
- 663 46 Mariño, J., Samaniego, P., Manrique, N., Valderrama, P., Roche, O., van Wyk de Vries, B., Guillou, H.,
664 47 Zerathe, S., Arias, C., Liorzou, C., 2021. The Tutupaca volcanic complex (Southern Peru):
665 48 Eruptive chronology and successive destabilization of a dacitic dome complex. *J. S. Am. Earth*
666 49
667 50
668 51
669 52
670 53
671 54
672 55
673 56
674 57
675 58
676 59
677 60
678 61
679 62
680 63
681 64
682 65

- 666 Sci., 109, 103-227.
- 667 1 Mehl, K.W., Schmincke, H.U., 1999. Structure and emplacement of the Pliocene Roque Nublo
668 2 debris avalanche deposit, Gran Canaria, Spain. *J. Volcanol. Geotherm. Res.* 94, 105-134.
- 669 4 Naranjo, J.A., Francis, P., 1987. High velocity debris avalanche at Lastaria volcano in the north Chilean
670 5 Andes. *Bull. Volcanol.* 49, 509-514.
- 671 8 Palmer, B.A., Alloway, B.V., Neall, V.E., 1991. Volcanic-debris avalanche deposits in New Zealand:
672 9 lithofacies organization in unconfined, wet-avalanche flows. In: Fisher, R.V., Smith G.A;
673 10 (Eds.), *Sedimentation in volcanic setting*. SEPM Spec. Pub. vol. 45, pp. 89-98.
- 674 13 Samaniego, P., Valderrama, P., Mariño, J., van Wyk de Vries, B., Roche, O., Manrique, N., Chedeville, C.,
675 14 Fidel, L., Malnati, J., 2015. The historical (218 ± 14 aAP) explosive eruption of Tutupaca volcano
676 15 (Southern Peru). *Bull. Volcanol.* 77, 51.
- 677 17 Sandnes, B., Flekkoy, E.G., Knudsen, H.A., Maloy, K.J., See, H., 2011. Patterns and flow in frictional fluid
678 18 dynamic. *Nat. Commun.* 2, 288.
- 679 23 Shea, T., van Wyk de Vries, B., 2008. Structural analysis and analogue modeling of the kinematics and
680 24 dynamics of rockslide avalanches. *Geosphere* 4, 657–686.
- 681 27 Siebe, C., Komorowski, J-C., Sheridan, M-F., 1992. Morphology and emplacement collapse of an
682 28 unusual debris avalanche deposit at Jocotitlán Volcano, Central Mexico. *Bull. Volcanol.* 54, 573-589.
- 683 30 Siebert, L., Roverato, M., 2020. A Historical Perspective on Lateral Collapse and Volcanic Debris
684 31 Avalanche. In: Roverato, M., Dufresne, A., Procter, J., (Eds.), *Volcanic Debris Avalanches from
685 32 Collapse to Hazards*. Springer, pp. 11-50.
- 686 36 Siebert, L., Glicken, H., Ui, T., 1987. Volcanic hazards from Bezymianny- and Bandai-type eruptions. *Bull.*
687 37 *Volcanol.* 49, 435-459.
- 688 39 Suzuki-Kamata, K., Kusano, T., Yamasaki, K., 2009. Fractal analysis of the fracture strength of lava
689 40 dome material based on the grain size distribution of block-and-ash flow deposits at Unze
690 41 volcano, Japan. *Sedim. Geol.* 220, 162-168.
- 691 45 Szabo, I., Domokos, G., Grotzinger, J.P., Douglas, J.J., 2015. Reconstructing the transport history of
692 46 pebbles on Mars. *Nat. Commun.* 6: 8366.
- 693 49 Valderrama, P., 2016. Origin and dynamics of volcanic debris avalanches: surface structure analysis
694 50 of Tutupaca volcano (Peru). *Earth Sciences. Univ. Blaise Pascal-Clermont-Ferrand II*.
- 695 52 Valderrama, P., Roche, O., Samaniego, P., van Wyk de Vries, B., Bernard, K., Marino J., 2016. Dynamic
696 53 implications of ridges on a debris avalanche deposit at Tutupaca volcano (southern Peru). *Bull.*
697 54 *Volcanol.* 78, 14.
- 698 56 Valderrama, P., Roche, O., Samaniego, P., Van Wyk de Vries, B., Araujo, G., 2018. Granular fingering as
699 57 a mechanism for ridge formation in debris avalanche deposits: laboratory experiments and
700 58 implications for Tutupaca volcano, Peru. *J. Volcanol. Geotherm. Res.* 349, 409-418.

- 701 Van Wyk de Vries, B., Self, S., Francis, P.W., Keszthelyi, L., 2001. A gravitational spreading origin for the
702 1 Socompa debris avalanche. *J. Volcanol. Geotherm. Res.* 105, 225-247.
703 2
- 703 3 Voight, B., Glicken, H., Janda, R.J., Douglass, P.M., 1981. Catastrophic rockslide-avalanche of May 18.
704 4
704 5 In: Lipman, P. W., Mullineaux, D.R. (Eds.), *The 1980 eruptions of Mount St. Helens, Washington.*
705 6
705 7 *U.S. Geol. Surv. Prof. Pap.* vol. 1250, pp. 347-371.
- 706 8
706 9 Zernack, A., Procter, J., Cronin S., 2009. Sedimentary signatures of cyclic growth and destruction of
707 10 stratovolcanoes: a case study from Mt Taranaki, New Zealand. *Sediment. Geol.* 220, 288-305.
707 11
707 12
707 13
707 14
707 15
707 16
707 17
707 18
707 19
707 20
707 21
707 22
707 23
707 24
707 25
707 26
707 27
707 28
707 29
707 30
707 31
707 32
707 33
707 34
707 35
707 36
707 37
707 38
707 39
707 40
707 41
707 42
707 43
707 44
707 45
707 46
707 47
707 48
707 49
707 50
707 51
707 52
707 53
707 54
707 55
707 56
707 57
707 58
707 59
707 60
707 61
707 62
707 63
707 64
707 65

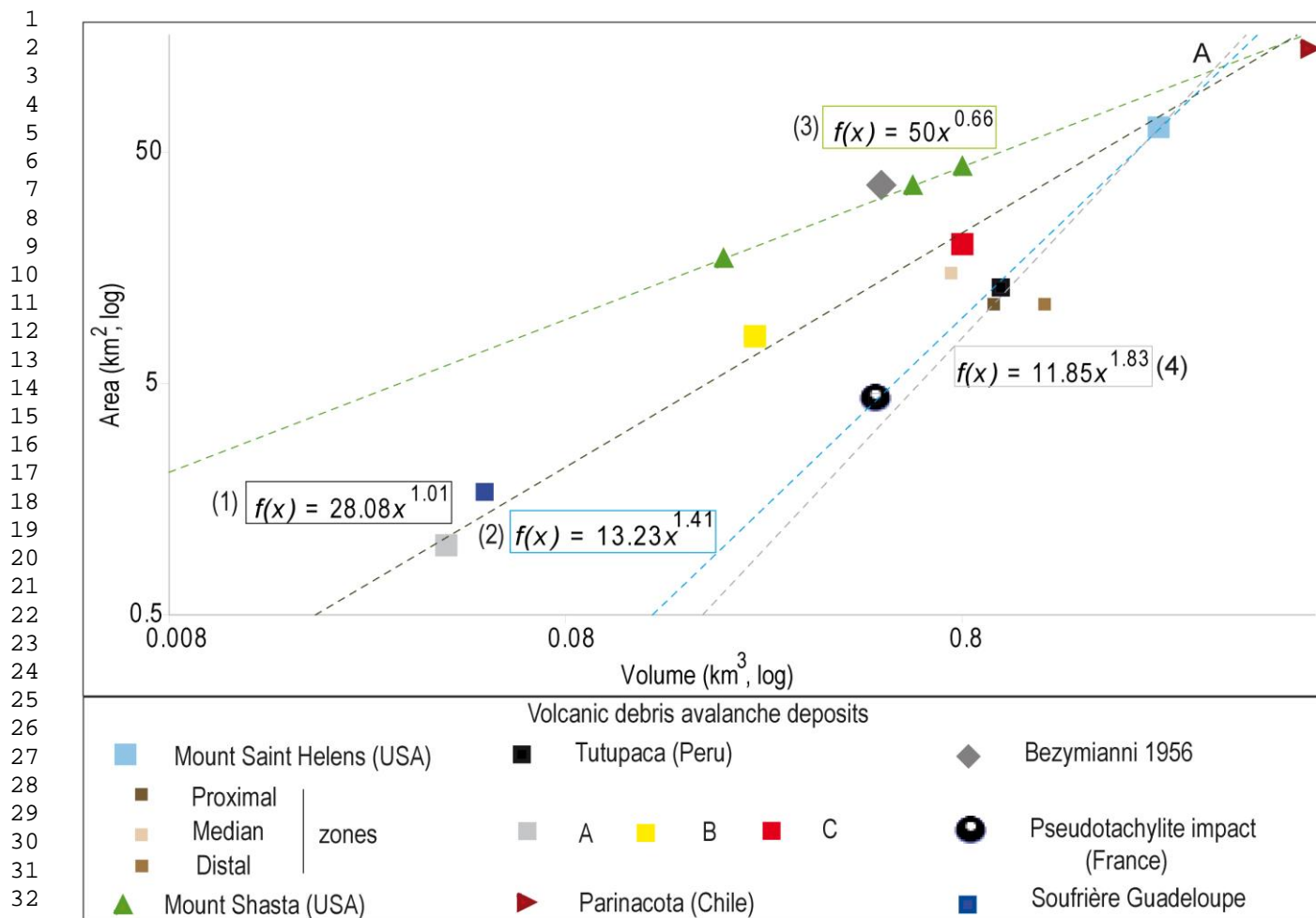
16
17
18
19
20
21
22
23
24
25
26
27
28
29
30
31
32
33
34
35
36
37
38
39
40
41
42
43
44
45
46
47
48
49
50
51
52
53
54
55
56
57
58
59
60
61
62
63
64
65

08 **Figures and Tables**



Revised Fig. 1. The flow chart for image analysis. A. The SPO analysis (Launeau and Robin, 2005) of block clusters with the inertia and intercepts method; B. The shape analysis of striations using the ImageJ Plugin “Gold morph” (Crawford and Mortensen, 2009).

712



71334

35
36 **Fig. 2.** Area (km^2) vs. volume (km^3) of volcanic debris avalanche deposits on double log graph: Mount
37 Shasta and Mount Saint Helens in the USA (Glicken, 1986; Siebert et al., 1987); Bezymianni in Kamchatka
38 (Siebert et al., 1987); Parinacota in Chile (Clavero et al., 2002; Legros, 2002); Tutupaca in Peru (Samaniego
39 et al., 2015; Valderrama et al., 2016); Soufrière in Guadeloupe (Boudon et al., 1984) and Mont Dore in
40 French Massif Central (Bernard and van Wyk de Vries, 2017). A. The proximal zone; B. The ridged unit; C.
41 The distal zone.
42
43
44
45
46
47

72047

48

49

50

51

52

53

54

55

56

57

58

59

60

61

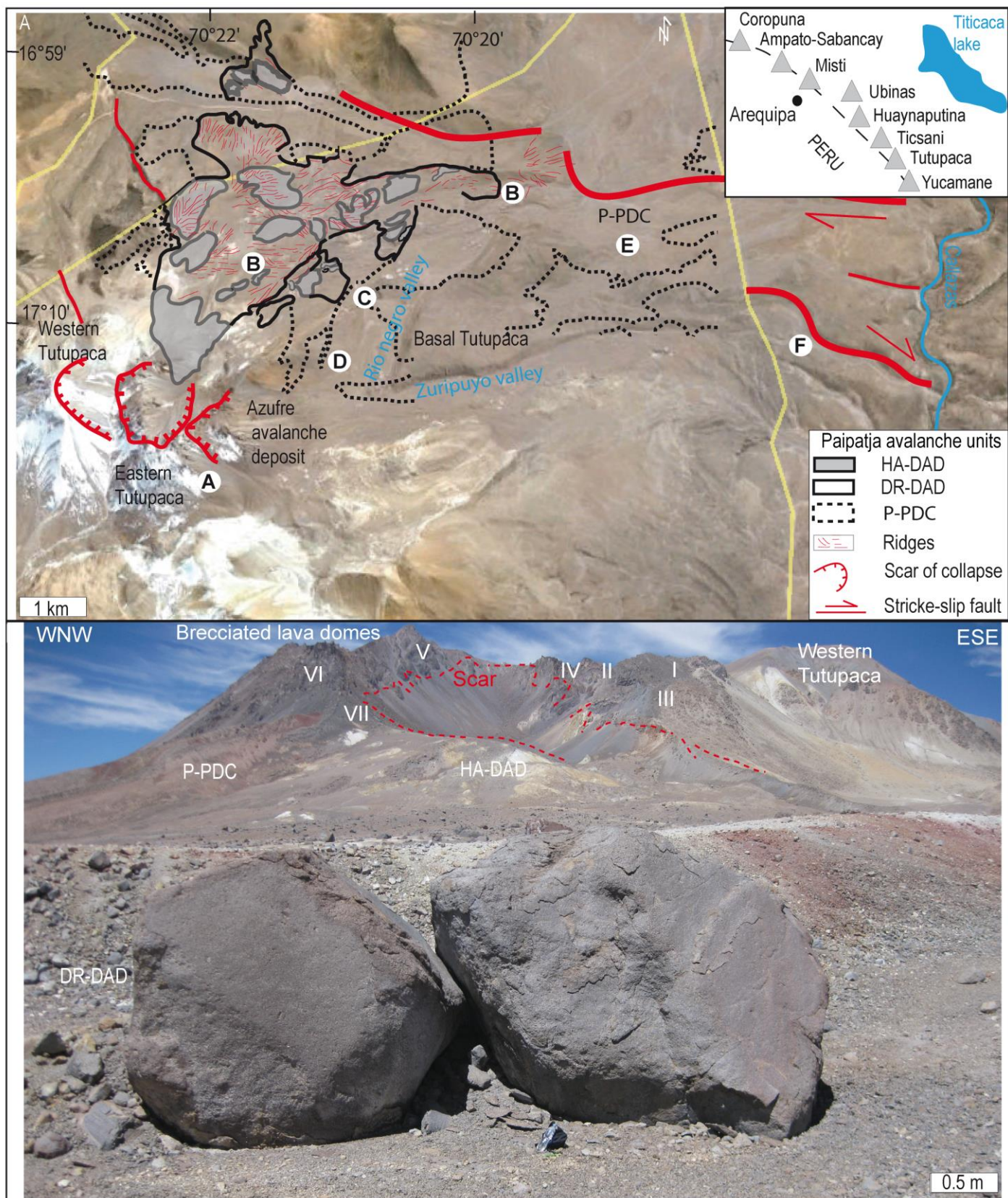
62

63

64

65

721



722

723

724

725

726

727

728

729

730

731

732

Revised Fig. 3. Geological setting of the Paipatja avalanche deposits exposed in the northeastern part of Tutupaca volcanic complex (Southern Peru, modified from Samaniego et al., 2015; Valderrama et al., 2016). A. Landforms of the avalanche deposits and structures at the North East of the brecciated lava domes from Google Earth with stratigraphic sections. We differentiate the hydrothermal rich avalanche deposit (HA-

733

734

735

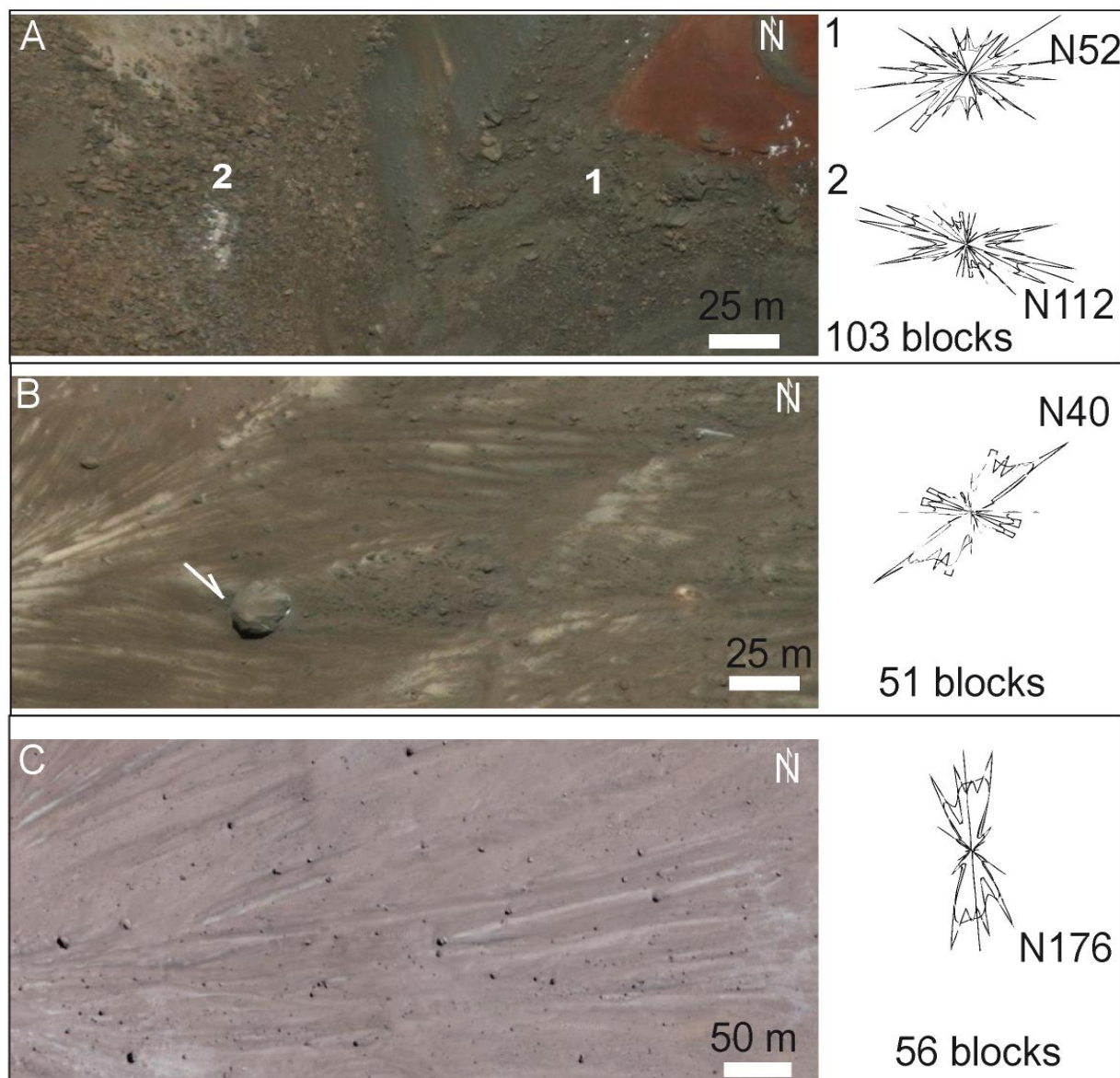
736

727 DAD, $L = 6-8$ km, $V < 1$ km³; $H/L = 0.23-0.17$, [Samaniego et al., 2015](#)); a dome rich debris-avalanche deposit
728 ¹ (DR-DAD); the Paipatja pyroclastic density current deposits (P-PDC, $\sim 218 \pm 14$ aBP). The right-top inset
729 ² shows the location of Pleistocene volcanoes in the Andean Central Volcanic Zone. The white points indicate
730 ⁴ the outcrop locations of the clusters and the block lithofacies. A. Under the erosional amphitheater of collapse
731 ⁶ scar in proximal zone; B. Transverse alignment of blocks and ridge structures; C. Extensional fault zone with
732 ⁸ abrasion and jigsaw-fractured lithofacies; D. Shear zone along lateral levee; E. Impact and lava bombs; F.
733 ¹⁰ Buried blocks and abrasion. B. Panoramic view of the northeast of Tutupaca volcano, showing the horseshoe-
734 ¹² shape amphitheater and lava domes (I to VI) and DR-DAD with transverse alignment of blocks. Most of the
735 ¹³ domes are constructed on the older hydrothermally altered basal edifice ([Samaniego et al., 2015](#); [Valderrama](#)
736 ¹⁵ [et al., 2016](#)).

737 ¹⁷
738 ¹⁸
739 ¹⁹

20
21
22
23
24
25
26
27
28
29
30
31
32
33
34
35
36
37
38
39
40
41
42
43
44
45
46
47
48
49
50
51
52
53
54
55
56
57
58
59
60
61
62
63
64
65

739



740

741 **Fig. 4.** The syn-emplacement block lithofacies and block orientations (SPO, [Launeau and Robin, 2005](#)) from
 742 proximal to distal zones using georeferenced Google Earth imagery. A. Proximal brecciated zones under the
 743 scar between domes V to VII: 1. An impacted and crushed zone showing imbricated block clusters without
 744 preferential orientation; 2. A tilted zone with N112E angular dome fragments adjacent to the PDC in red; B.
 745 Isolated polyhedral block (white arrow) of ridge structures in the median zone showing in downstream N40E
 746 disaggregated clasts; C. The transverse and isolated blocks (>1 m in length, N176E) surrounded by P-PDC
 747 unit in distal zone.

748

749

750

751

752

753

754

755

756

757

758

759

760

761

762

763

764

765

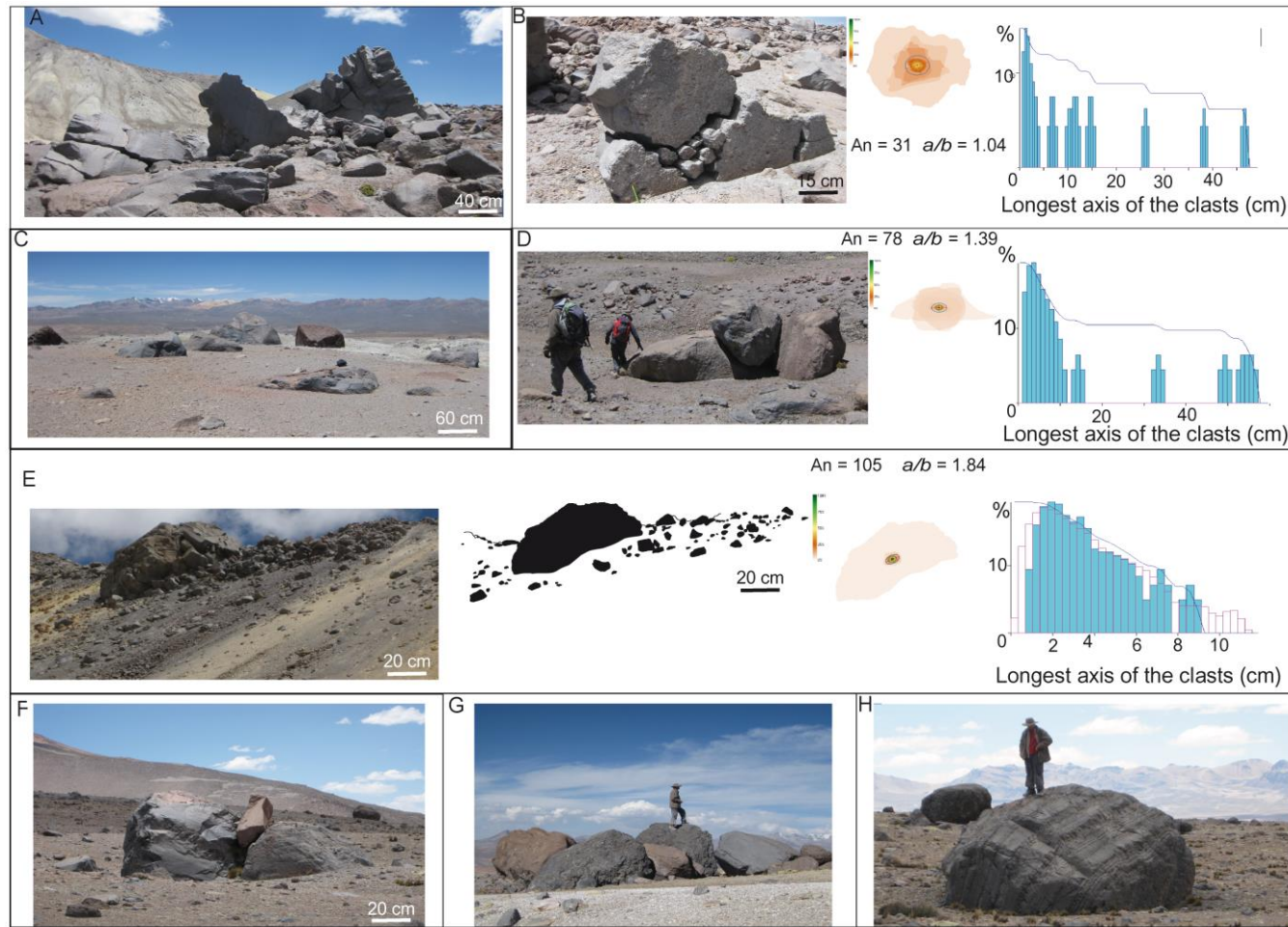


Fig. 5. Block clusters of DR-DAD from SPO analysis (Launeau and Robin, 2005). A. Vertical impact of blocks with abraded surface and undulated fractured borders under the erosional amphitheater of collapse scar; B. Impacted jigsaw-clusters with polymodal clast distribution; C. Subdued blocks in transverse ridges; D. Impacted blocks in distal zone with polymodal distribution of the clasts; E. Block along lateral levee with sigmoidal jigsaw-breccias showing a bimodal clast distribution; F. Angular and impacted block between aligned and subdued blocks; G. Block cluster in distal zone; H. Subdued and tilted blocks.

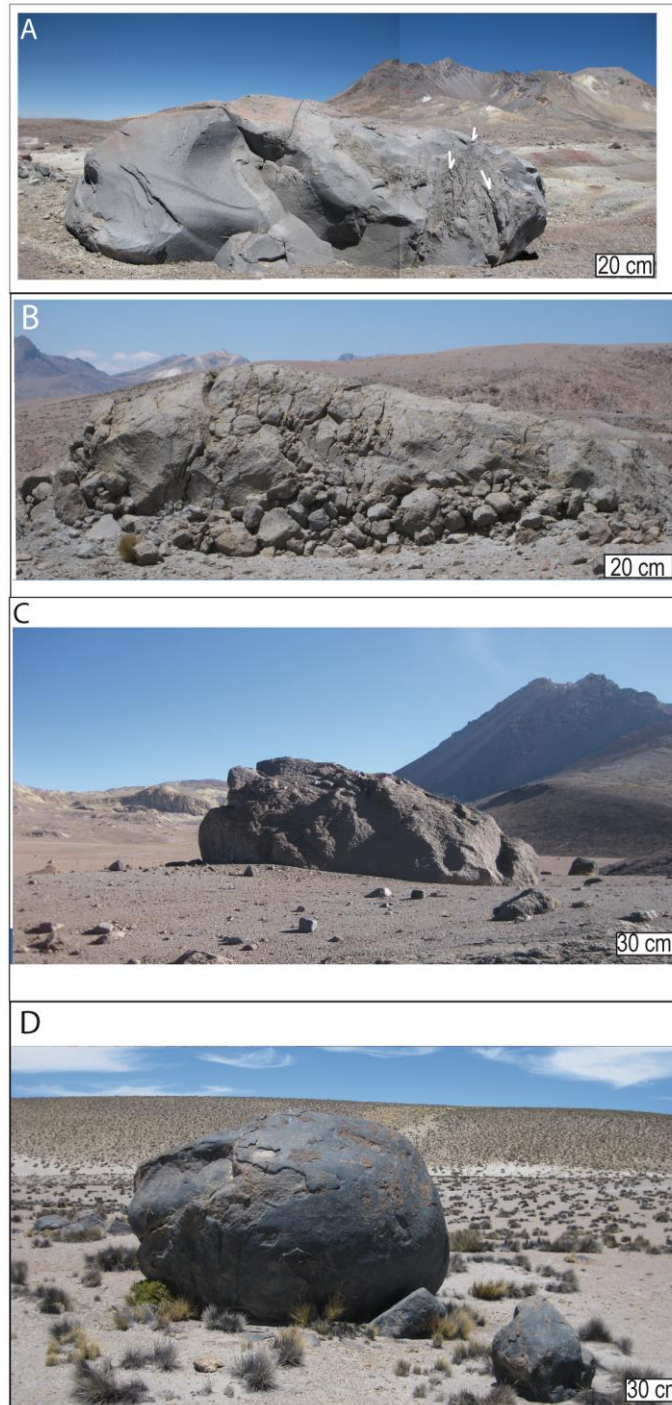


Fig. 6. Textural gradient of block lithofacies of the Paipatja avalanche deposits. A. Transverse blocks with an oriented abrasion: *white arrows* show striations on upstream sub-rounded faces and planar faces with conchoidal fractures in downstream; B. Large polyhedral block (~3 m high and ~5 m length) with an oriented abrasion, quenched and cracked surface in upper part and sub-rounded lava in altered vitreous phase in lower part; C. Transversal alignment of abraded blocks with bimodal clast distribution from SPO analysis (Launeau and Robin, 2005) related to pyroclastic density current deposits; D. Polymodal clast distribution (SPO analysis, Launeau and Robin, 2005) of pyroclastic density current deposits around a distal sub-rounded block.

763
764
765
766
4
5
6
7
8
9
10
11
12
13
14
15
16
17
18
19
20
21
22
23
24
25
26
27
28
29
30
31
32
33
34
35
36
37
38
39
40
41
42
43
44
45
46
47
48
49
50
51
52
53
54
55
56
57
58
59
60
61
62
63
64
65

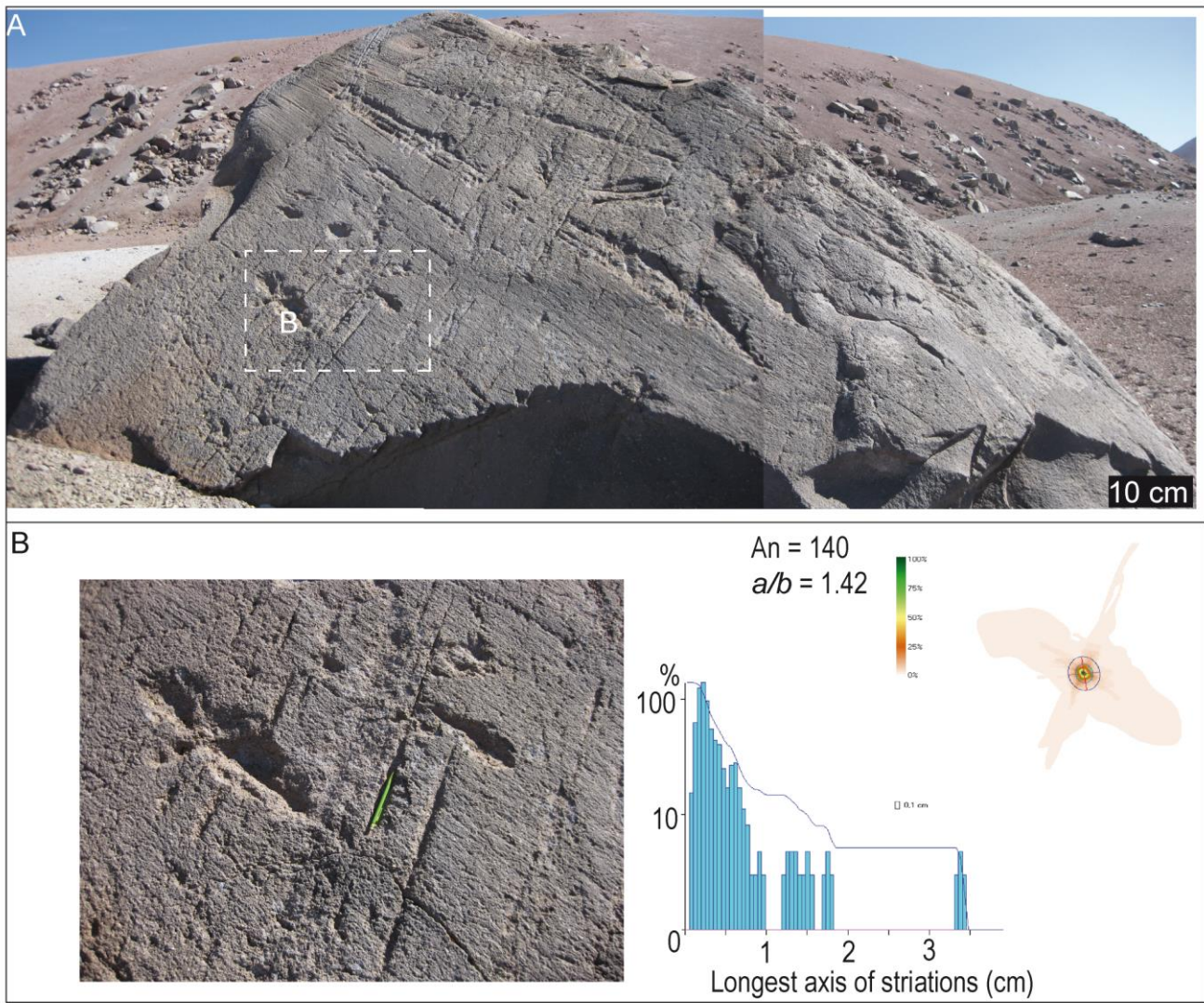
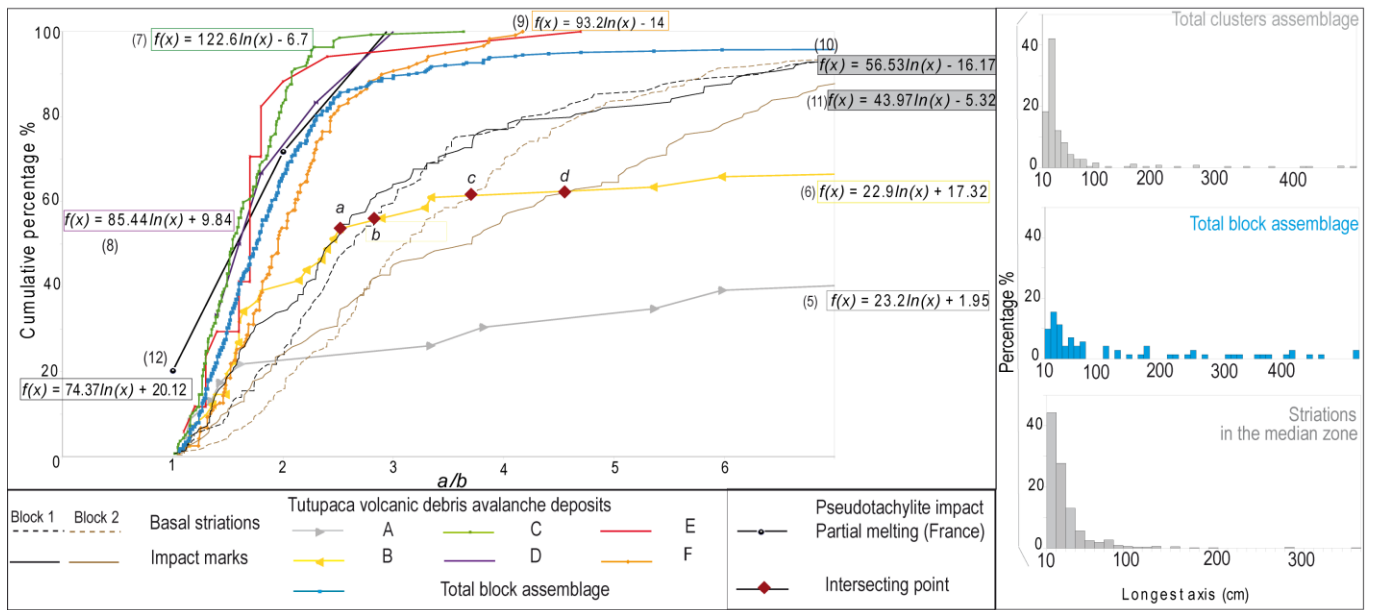
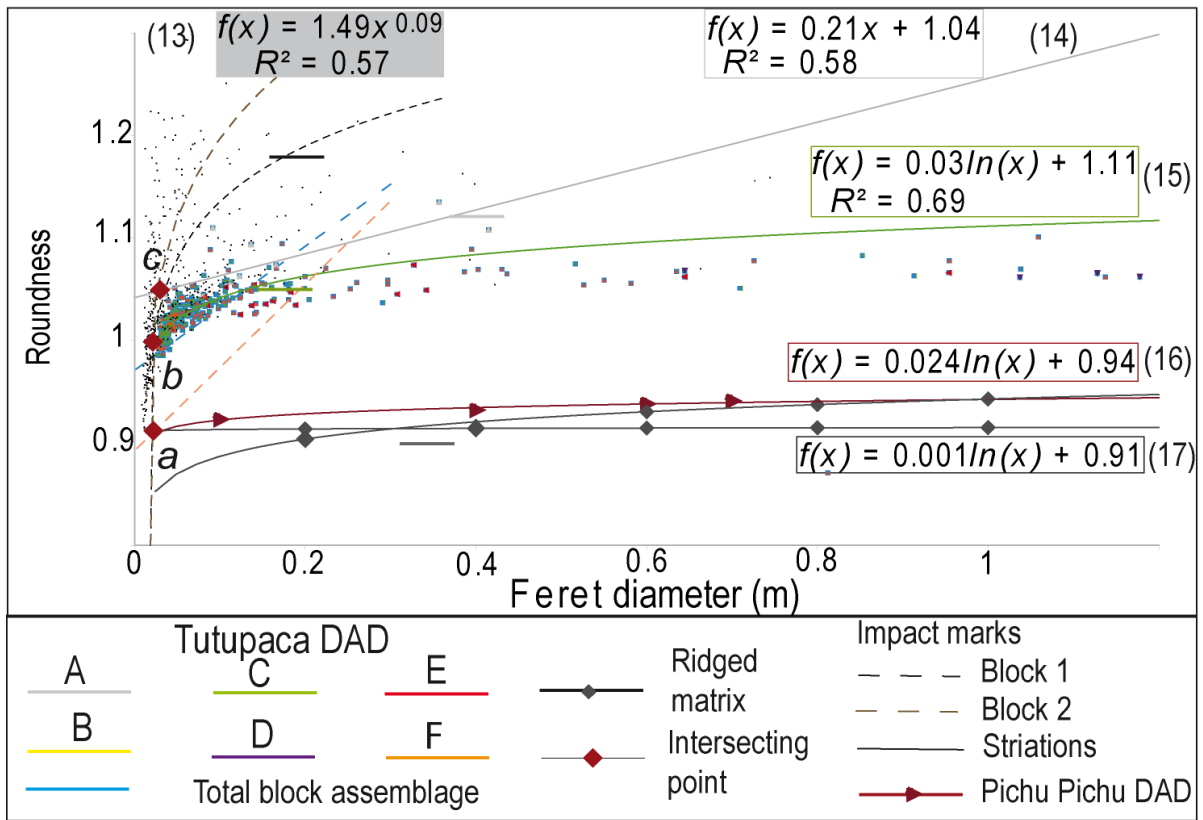


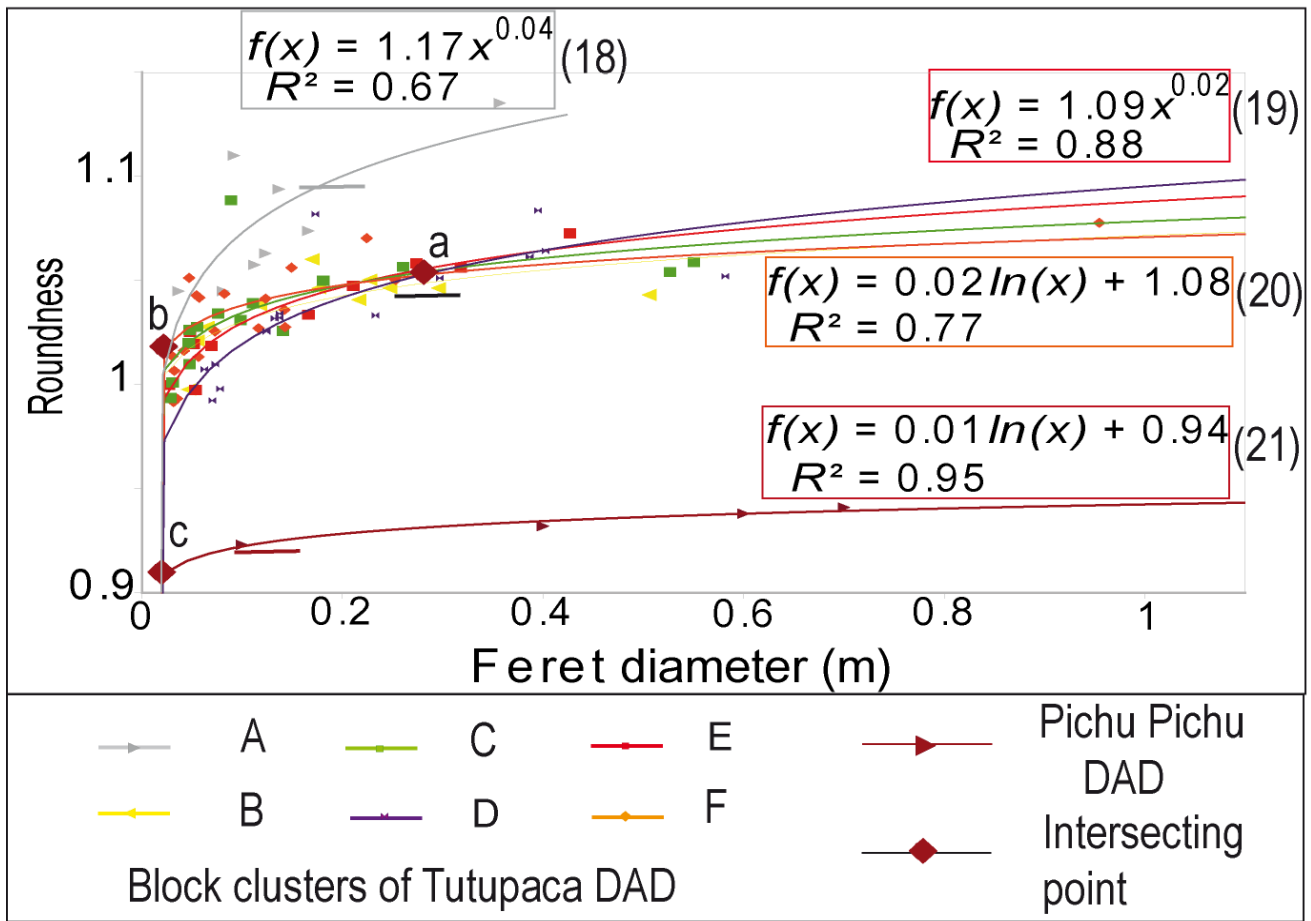
Fig. 7. Striations and grooves of ridged blocks from SPO analysis (635 striations, [Launeau and Robin, 2005](#)). A. Subdued block (~2 m high and 1.6 m length) with abraded planar surfaces, grooves and striations with circular depressions (~1-5 cm depth, ~2-3 mm wide); B. Detailed analysis of grooves and striations showing polymodal distribution related to the P-PDC interactions ($An = 140$ striations, $a/b = 1.42$).



Revised Fig. 8. Sedimentological analysis of block lithofacies of the Paipatja avalanche deposits from proximal to distal zones. A. Cumulative curves of block lithofacies vs. a/b from SPO analysis (404 blocks, 635 striations and impact marks; Launeau and Robin, 2005); B. Histograms.



Revised Fig. 9. Roundness vs. Feret's diameter (m) of block lithofacies and striations in different zones from shape analysis using the software ImageJ (404 blocks, 635 striations and impact marks; [Blott and Pye, 2008](#); [Crawford and Mortensen, 2009](#)). The horizontal lines indicate the Feret's diameter at which roundness stopped increasing. Error bars are smaller than the symbols.



Revised Fig. 10. Roundness vs. Feret's diameter (m) of block clusters from shape analysis using the software ImageJ (Blott and Pye, 2008; Crawford and Mortensen, 2009). The horizontal lines indicate the Feret's diameter at which roundness stopped increasing. Error bars are smaller than the symbols (see Supplemental File 2).

830 **Revised Table 1.** List of acronyms and their definitions.

831

1

2

3

4

5

6

7

8

9

10

11

12

13

14

15

16

17

18

19

20

21

22

23

24

25

26

27

28

29

30

31

32

33

34

35

36

37

38

39

40

41

42

43

44

45

46

47

48

49

50

51

52

53

54

55

56

57

58

59

60

61

62

63

64

65

	Acronyms	Definitions
	<i>A</i>	Area
	<i>a/b</i>	the largest axis / minor axis
	<i>D</i>	Fractal dimension
	<i>d</i>	Depth
	<i>E</i>	Ellipse
	Ellipse/ <i>a/b</i>	The ratio of the ellipse to the <i>a/b</i>
	<i>FD</i>	Feret's Diameter
Quantitative parameters	<i>H</i>	Height
	<i>h</i>	Exponent of the power regressions
	<i>H/L</i>	Apparent friction
	<i>L</i>	Length
	<i>S</i>	Surface
	<i>T</i>	Thickness
	<i>v</i>	Velocity
	<i>V</i>	Volume
	<i>W</i>	Width
	DR-DAD	Dome-rich debris-avalanche deposit
Lithofacies	HA-DAD	Hydrothermally-rich debris avalanche deposit
	P-PDC	Paipatja pyroclastic density current deposit

832

833

834

835

836

837

838

839

840

841

842

843

844

845

846

847

848

849

850

851

852

853

854

855

Revised Table 2. Methodology for block laboratory analysis.

Outcrop map and observations	Google Earth imagery, landforms, faults, orientations, lateral and vertical variations in block lithofacies and lithostratigraphy, textures.
Grain size analysis	Image analysis and Feret's diameter measurement. Clast size distribution: cumulative curves, fractal distributions, statistical parameters.
Shape analysis	Shape analysis with texture of blocks, preferred orientation of block largest axis and

shape parameters.

Revised Table 3. Clast shape parameters with Feret's Diameter (*FD*), Riley's circularity (*R_c*) and Roundness (*R*, Blott and Pye, 2008; Crawford and Mortensen, 2009; Bernard, 2015).

<p>The diagram shows a grey shaded irregular clast. Two parallel blue lines are tangent to the top and bottom of the clast, with a double-headed arrow between them labeled 'FD'. A dashed black circle is inscribed within the clast, labeled 'Di'. A solid black circle is circumscribed around the clast, labeled 'Dc'. The perimeter of the clast is labeled 'P', and the perimeter of the circumscribed circle is labeled 'Pc'.</p>	<p>Feret's Diameter (<i>FD</i>)</p> <p>The longest distance between two parallel tangential lines</p>
	<p>Riley's circularity (<i>R_c</i>, Riley, 1941)</p> $R_c = \sqrt{Di / Dc}$ <p><i>Di</i> the largest inscribed circle <i>Dc</i> the smallest circumscribed circle</p>
	<p>Roundness (<i>R</i>)</p> $R = P / Pc$ <p><i>P</i> Perimeter <i>Pc</i> Convex perimeter</p>

861
862
863
864
865
866
867
868
869
870
871
872
873
874
875
876
877
878
879
880
881
882
883
884
885
886
887
888
889
890
891
892
893
894
895
896
897
898
899
900

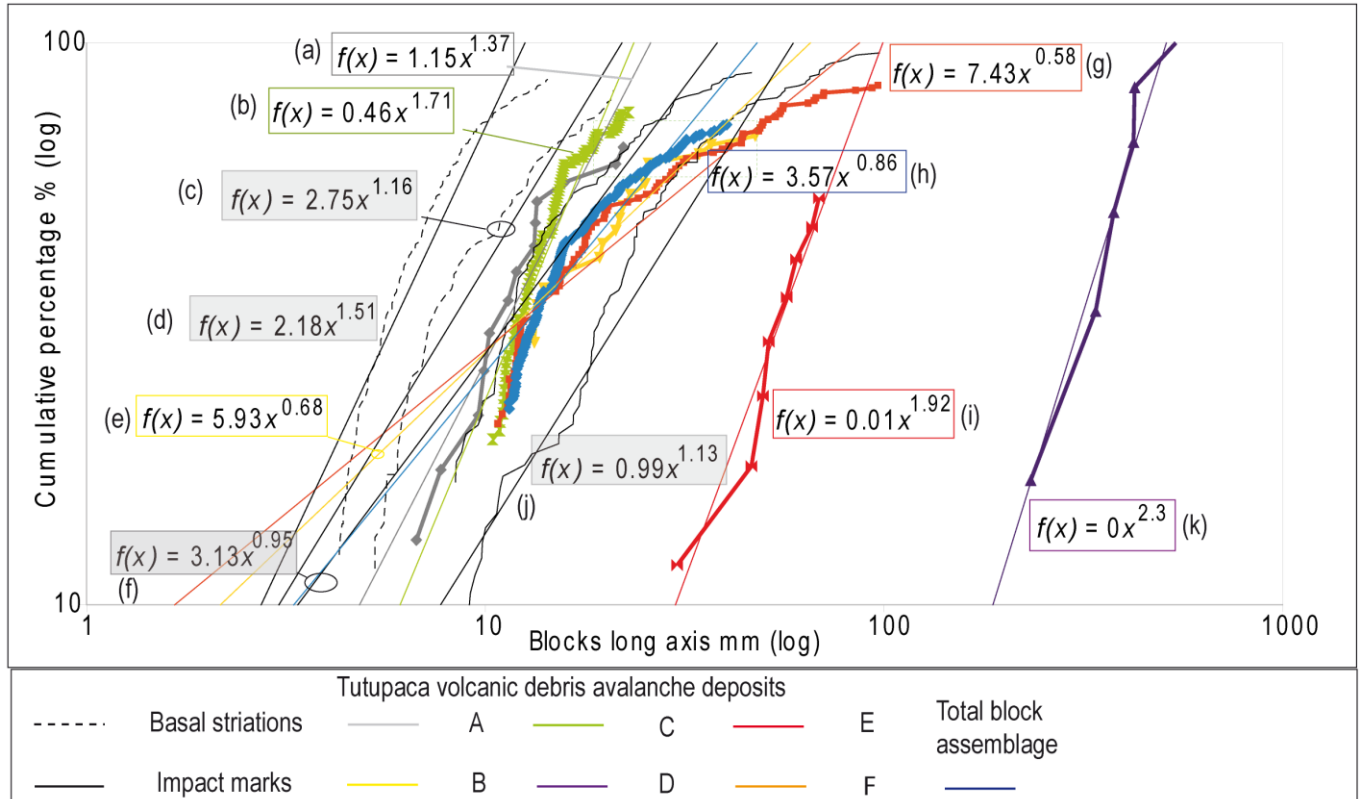
Revised Table 4. Fractal results of block lithofacies in different zones and striations compared to the surrounded matrix of the Paipatja avalanche deposits and P-PDC (see [Supplemental File 1](#); [Suzuki-Kamata et al., 2009](#)).

	<i>h</i>	<i>D</i>	Correlation coefficient	Range of the clast size (cm)	Number of clasts
A	1,37	0,26	0,9	6.7-22.1	14
B	0,67	1,66	0,9	13.2-47.5	18
C	1,7	-	0,9	10.4-22.9	78
D	2,29	-	0.95	233.4-539.5	7
E	1,92	-	0.93	30.3-68.7	9
F	0,58	1,83	0,9	10.7-96.5	120
All zones	0,86	1,28	0,9	11.4-40.3	137
Surrounded matrix	0.07-1.16	0.67-2.84	0.91-0.98	0.001-6.4	-
Striations	1.18	0.6	0.9	5.94-44.68	265

Revised Table 5. Mean values of block shape parameters and striations from SPO and shape analysis using the software ImageJ (404 blocks, see [Supplemental File 2](#); [Launeau and Robin, 2005](#); [Blott and Pye, 2008](#); [Crawford and Mortensen, 2009](#); [Bernard, 2015](#)). These shape data have been associated with the correspondent standard errors.

	Roundness	Riley's circularity	<i>a/b</i>	Ellipse	Ellipse/ <i>a/b</i>
A	1.07±0.01	0.73±0.03	1.68±0.14	3.61±0.74	2.29±0.54
B	1±0.02	0.69±0.02	1.88±0.38	3.2±0.65	1.7±0.24

C	1.02±0.001	0.68±0.006	1.63±0.3	3.34±0.25	2.04±0.15
D	1.13±0.07	0.64±0.05	1.91±0.26	5.15±2.18	2.7±0.59
E	1±0.02	0.64±0.02	1.8±0.2	5.01±1.25	2.78±0.33
F	1.05±0.03	0.63±0.01	2.1±0.06	3.95±0.24	1.88±0.35
Mean	1.23±0.009	0.66±0.005	1.7±0.03	3.5±0.15	2.05±0.1
Striations	0.9±0.01	0.3±0.007	3.69±0.1	21.9±1.57	5.82±0.5



Supplemental File 1

Cumulative % vs. long clast-axis on double log graph. The exponent h of size distributions were estimated from the power regressions (a-k) by the methods of the least squares ($R^2 > 0.9$ in Table 4, Eq. 6 in Suzuki-Kamata et al., 2009). The h values obtained for each structural unit ranged from 6.7 to 537.9 cm for block lithofacies and from 5.94 to 44.68 cm for striations. From following equation $2h + D = 3$ (Eq. 7 in Suzuki-Kamata et al., 2009), we translate the h -values into fractal D values in Table 4. The h -values for the block lithofacies and striations range from 0.58 to 2.29 (Table 4). Substitution of these values into the previous equation (Eq. 7 in Suzuki-Kamata et al., 2009), gives corresponding fractal D -values of 0.26 to 1.83. The negative values of fractal dimension have not been considered in Table 4.

893

894

~~900~~

3

4

5

6

7

8

9

10

11

12

13

14

15

16

17

18

19

20

21

22

23

24

25

26

27

28

29

30

31

32

33

34

35

36

37

38

39

40

41

42

43

44

45

46

47

48

49

50

51

52

53

54

55

56

57

58

59

60

61

62

63

64

65

Manuscript

Number:

VOLGEO-D-21-00343R2

Collisional interactions and the transition between lava dome sector collapse and pyroclastic density currents at Tutupaca volcano (Southern Peru).

Dear Karine Bernard,

Thank you for submitting your manuscript to Journal of Volcanology and Geothermal Research. I have received comments on your manuscript from two reviewers (accept and minor). Both reviewers found that you have significantly improved your manuscript. One of them asked for a minor revision and provided an edited file and some comments listed in the review. Both reviewers, though, mentioned some issues with figures 7 and 9. Therefore, I invite you to resubmit your manuscript after minor revision.

When revising your manuscript, please provide a 'response to the reviewers' that outlines every change made point-by-point in response to the reviewers' comments, stating clearly exactly what has been changed in the manuscript and providing line numbers wherever possible. Please also provide suitable rebuttals for any comments not addressed. Please note that your revised submission may need to be re-reviewed.

To submit your revised manuscript, please log in as an author at <https://www.editorialmanager.com/volgeo/>, and navigate to the "Submissions Needing Revision" folder.

NOTE: Upon submitting your revised manuscript, please upload the source files for your article. We cannot accommodate PDF manuscript files for production purposes. We also ask that when submitting your revision, you follow the journal formatting guidelines. For additional details regarding acceptable file formats, please refer to the Guide for Authors at: <https://www.elsevier.com/journals/journal-of-volcanology-and-geothermal-research/0377-0273/guide-for-authors>

Journal of Volcanology and Geothermal Research values your contribution and I look forward to receiving your revised manuscript.

Research Elements (optional)
This journal encourages you to share research objects - including your raw data, methods, protocols, software, hardware and more – which support your original research article in a Research Elements journal. Research Elements are open access, multidisciplinary, peer-reviewed journals which make the objects associated with your research more discoverable, trustworthy and promote replicability and reproducibility. As open access journals, there may be an Article Publishing Charge if your paper is accepted for publication. Find out more about the Research Elements journals at https://www.elsevier.com/authors/tools-and-resources/research-elements-journals?dgcid=ec_em_research_elements_email.

Kind regards,

Jose Luis Macias

Editor, Journal of Volcanology and Geothermal Research.
Editor and Reviewer comments:

Rebuttal letter

We thank the Chief Editor and all reviewers for their useful comments. The detailed and fair reviews, together with many insightful comments, have been greatly appreciated. We have taken account of the reviewer comments. Revised sentences, paragraphs, sections as well as changes in titles as recommended appear in blue. Below is a summary of our response to the comments of Editor-in-Chief Dr. Macias and

the two reviewers.

1
2 Comments of Chief Editor Dr. Macias:
3

4
5 Figures 9B and 10B with no clear correlations (with $R^2 \leq 0.5$) that we attributed to the shape variations of
6
7 block lithofacies and striations based on textural parameters have been removed according to reviewers 1
8
9 and 2. Supplementary files 1 and 2 focus on the original data used to calculate the fractal dimension, the
10
11 mean values and standard errors of the shape parameters. We have checked the format of revised
12
13 manuscript.
14
15

16 Reviewer #1: Dear Editor of JVGR,
17
18
19

20 After reading the new version of the manuscript "Collisional interactions and the transition between lava
21
22 dome sector collapse and pyroclastic density currents at Tutupaca volcano (Southern Peru)" by Bernard et
23
24 al., It is clear that the paper has been greatly improved. The comments made in previous reviews have
25
26 been mostly solved. Nevertheless, It still seems that the correlations shown in Figures 9 and 10B are low
27
28 to fully support all the inferences made from them. However, the detailed description of the Tutupaca
29
30 debris avalanche and the deep textural analysis shown in this work is novel and of clear relevance to the
31
32 scientific community and the study of debris avalanches. Based on this, I suggest approving the
33
34 manuscript for its publication by JVGR.

35
36 Figures 9B and 10B with no clear correlations (with $R^2 \leq 0.5$) with intersecting points that we attributed to
37
38 the shape variations of block lithofacies and striations based on textural parameters have been removed
39
40 according to reviewer 1. These paragraphs (lines 370-371, 527-529) related to Figs. 9B and 10B have
41
42 been removed. The comments have been considered related to table 5 and supplemental file 2.
43
44

45
46 Lines 408-410. The Riley's circularity of block clusters shows decreasing values from the proximal to
47
48 distal zones (Table 5, see Supplemental File 2) related to Feret's diameter, implying textural relationships
49
50 between the block clusters with the run-out distance.

51
52 Lines 502-503. Textural relationships appear between proximal blocks and the striated blocks from the
53
54 ridges (Table 5) with decreasing values of Riley's circularity.

55
56 Lines 540-543: The inherited shapes of the lava blocks and the co-genetic evolution between the blocks
57
58 from the ridges and striations may be associated to secondary fracturing with partial decompression
59
60 during run-out propagation (Bernard et al., 2019).

61
62 Lines 554-561. The Riley's circularity (Table 5, see Supplemental File 2) shows that the polyhedral blocks
63
64 with conchoidal fractures and striations of the ridge structures differentiated from sub-rounded blocks in
65

the distal zone. These may be associated to an oriented abrasion and thermal shock generating tilted blocks with cracked surface. The clast breakage with striations due to collisional transport decreases the Riley's circularity (Table 5). These block lithofacies may be associated to crushing impact with frictional temperature during oscillatory stress (Bernard and van Wyk de Vries, 2017) related to decompression in rotational shearing, and matrix segregation.

Reviewer #2: Dear Authors:

In this new review, I have found the paper more complete and with a better readability. I consider that it contains relevant information and the methodology used offers interesting ideas for the reader who works with avalanches. The new paragraphs added in the introduction and in the methodology, as well as the various changes and attachments that have been made, have improved the work significantly. The majority of the suggested changes have been made; however, the text is still perfectible (see added file with annotations) and two non-negligible issues remain and must be solved.

The first is related to figures 9 and 10, the ultimate meaning of which is still difficult for the reader to understand and which, from my point of view, could hide a background error. In fact, in the original figure you submitted, on the abscissa there was a parameter called "Ferret's Diameter" and it had a length in meters (m). With this grainsize parameter the graph made sense because it was a shape parameter (perimeter's roughness and Riley's Circularity) versus a grainsize. However, this parameter was poorly defined in the original text. In Table 2, where it appeared as the relationship between Feret max (a major diameter) and a Feret perpendicular to the former (an intermediate diameter), that is, a general form parameter. This error was pointed out in the first revision and the name was changed in Table 2 and in the figures. Anyhow, now the graph has a general form parameter on the ordinate (Max Feret diameter versus intermediate Feret diameter) and another general form parameter on the abscissa (Riley circularity). This being the case, it is autocorrelated data and does not provide useful information. This is a point that has to be unraveled.

The definitions and the figure of the shape parameters for the debris avalanche are described separately in Table 3. The Feret's diameter defined as the longest distance between two parallel tangential lines (Table 3) and roundness have been considered.

Lines 140-143. The shape analysis using the ImageJ Plugin "Gold morph" has been applied to 404 blocks and 635 striations of the avalanche units to compute minor and major axis length, Feret's diameter defined as the longest distance between two parallel tangential lines, perimeter and convex perimeter, radii of the smallest inscribed and largest circumscribed circles (Fig. 1B; Table 3; Crawford and Mortensen, 2009).

Lines 146-147. The values of Riley's circularity are less than 1 for the non-spherical volcanic clasts (Table 5).

Lines 156-157. The roundness, the Riley's circularity, the a/b ratio, ellipse, fractal D -values of each mesoscale structure have been calculated.

1
2
3
4
5
6
7
8
9
10
11
12
13
14
15
16
17
18
19
20
21
22
23
24
25
26
27
28
29
30
31
32
33
34
35
36
37
38
39
40
41
42
43
44
45
46
47
48
49
50
51
52
53
54
55
56
57
58
59
60
61
62
63
64
65

Figures 9B and 10B with no clear correlations (with $R^2 \leq 0.5$) that we attributed to the shape variations of block lithofacies and striations based on textural parameters have been removed according to reviewer 1.

These paragraphs (lines 370-371, 527-529) related to Figs. 9B and 10B have been removed. The comments are considered related to table 5 and supplemental file 2.

Lines 408-410. Riley's circularity of block clusters shows decreasing values from the proximal to distal zones (Table 5, see Supplemental File 2) related to Feret's diameter, implying textural relationships between the block clusters with the run-out distance.

Lines 502-503. Textural relationships appear between proximal blocks and the striated blocks from the ridges (Table 5) with decreasing values of Riley's circularity.

Lines 554-561. The Riley's circularity (Table 5, see Supplemental File 2) shows that the polyhedral blocks with conchoidal fractures and striations of the ridge structures differentiated from sub-rounded blocks in the distal zone. These may be associated to an oriented abrasion and thermal shock generating tilted blocks with cracked surface. The clast breakage with striations due to collisional transport decreases the Riley's circularity (Table 5). These block lithofacies may be associated to crushing impact with frictional temperature during oscillatory stress (Bernard and van Wyk de Vries, 2017) related to decompression in rotational shearing, and matrix segregation.

Another important point to clarify and solve, is related to the fractal analysis of the granulometries, carried out using the method of Suzuki -Kamata et al., 2009. Table 4 shows values of negative fractal dimension (distributions C, D and E), which can be originated by two causes, 1) having plotted the granulometric curves in reverse or 2) having an unrealistic granulometric distribution due to insufficient data or having used a non-rigorous methodology (see annotations in the attached file).

Considering the great effort provided in improving the manuscript, the increased readability and the important and interesting data presented, I believe that the paper can be ready for publication in JVGR after having satisfactorily resolved the two indicated points and realized the minor changes suggested.

A cordial greeting

Damiano Sarocchi

The negative values of fractal dimension have been removed in Table 4 (See Supplemental file 1) and the standard errors ($<10^{-3}$) related to photographic shot geometries have been considered (lines 138-140).

Supplemental File 1

Cumulative % vs. long clast-axis on double log graph. The exponent h of size distributions were estimated from the power regressions ($a-k$) by the methods of the least squares ($R^2 > 0.9$ in Table 4, Eq. 6 in Suzuki-Kamata et al., 2009). The h values obtained for each structural unit ranged from 6.7 to 537.9

cm for block lithofacies and from 5.94 to 44.68 cm for striations. From following equation $2h + D = 3$ (Eq. 7 in Suzuki-Kamata et al., 2009), we translate the h -values into fractal D values in Table 4. The h -values for the block lithofacies and striations range from 0.58 to 2.29 (Table 4). Substitution of these values into the previous equation (Eq. 7 in Suzuki-Kamata et al., 2009), gives corresponding fractal D -values of 0.26 to 1.83. The negative values of fractal dimension have not been considered in Table 4.

Lines 128-129

Where can these curves be found? are those the curves of figure 8? But they are only three curves. It is very important that all granulometries can be consulted, at least in supplementary material. The granulometries are those of figure 8? It should be noted that the curves are not complete, they have a bias towards the coarse clasts, completely missing the component of clasts below 10 cm for resolution limits. Explain somewhere how the granulometry was obtained. Are the percentages obtained by volumetric data (stereological method)? or are they just counts?

Lines 127-139. Fractal dimensions h and D of size distributions were estimated from the power regressions (Table 4, see Supplemental File 1, Suzuki-Kamata et al., 2009). The cumulative curves of the clast-size distributions *vs. a/b* (Fig. 8) were compared to distinguish the block avalanche units from proximal to distal zones. The calculated block-size distributions estimated from 41 outcrop photographs with the inertia and intercepts methods using the SPO analysis (from metric-size blocks to clasts >10 cm; Fig. 8B; Launeau and Robin, 2005). The longest axis of 404 block outlines were measured and counted per image area from the photographs. The normalized frequency histograms (Launeau and Robin, 2005) were produced by grouping the longest axis of blocks (cm) into 100-cm bins (number of size-intervals) and normalizing the number of occurrences in each bin to the total number of measurements from automatic image analysis. The sectional effects have been considered (Launeau and Robin, 2005). These data contribute to differentiate the effect of cataclasis between each fraction correlated with different structural units from proximal to distal zones. The subdued blocks and clasts below 10 cm are not considered related to resolution limits.

Line 136 : Are referring to Riley's value? This sentence is not clear

Line 146-147: The values of Riley's circularity are less than 1 for the non-spherical volcanic clasts (Table 5).

Lines 137-138. In this case, the resolution of the camera is not so important, what is rather important is how the photographs were taken, distance, geometry of the shot, objective used (the distortions in the image depend on this).

1 Lines 148-152. To characterize the two-dimensional shape of mesoscale structures, we took 5.9
2 megapixel photographs of abraded flat surfaces of two blocks with a digital camera. A digital camera
3 (6.2-18.6 mm lens, 35-105 mm focal length) image at a camera distance of <20 cm had a standard error
4 for mean distortion around $\sim 10^{-3}$. All the striations observed in the median zone have been quantified by
5 using high-resolution images (3648 X 2736 pixels) of two block faces.
6
7

8 Lines 150-152
9

10 If the Feret ratio is a measure of the general form, as it appears in the definition given in table 2, and the
11 Riley circularity is also a form factor related to the general form of the clasts, the graph does not make
12 much sense, and data in this case would be autocorrelated.
13
14

15 The Feret's diameter (m), defined as the longest distance between two parallel tangential lines (Table 3,
16 Figs. 9-10) have been considered.
17
18
19
20

21 Lines 162-164. Figure 9 shows the evolution of the roundness with Feret diameter for block lithofacies
22 and striations. Figure 10 shows the evolution of the roundness with Feret diameter for block clusters.
23
24
25

26 Line 205. This symbol has already been used twice, for the depth of the grooves and to define one of the
27 fractal dimensions. You have to change the symbols!
28
29

30 Lines 217-219. ... characterized by *torevas* ($H = 20-40$ m, $L = 1.5$ km), long lateral levees ($L = 1.5$ km)
31 and hummocky-structures ($L = 200-800$ m, $H = 20-40$ m) up to 4-6 km from the scar (Samaniego et al.,
32 2015; Valderrama et al., 2016).
33
34
35
36

37 Lines 326-331. : It would be important to be able to consult the log-log graphs with "cumulative mass of
38 fragments" vs "particle size" used to calculate the fractal dimension, as well as the original granulometries
39 and known the number of clasts used to obtain the distributions. Maybe in the supplementary material.
40
41
42

43 About the methodology used to obtain the granulometric distributions, see specific comment.
44

45 Supplementary file 1 focus on the original data used to calculate the fractal dimension. The number of
46 clasts used to obtain the distributions have been considered in Table 4. The negative values of fractal
47 dimension have been removed in table 3 (See Supplemental file 2) and the standard errors ($<10^{-3}$) related
48 to photographic shot geometries have been considered (lines 138-140).
49
50
51
52
53

54 Lines 338-340. A specific clast-size fractal distribution is calculated in the range between 6.7 and 539 cm.
55 The mean fractal D value, calculated from exponent h of power regressions, is around ~ 1.28 in the 11.4-
56 40.3 cm clast-size range (Table 4; see Supplemental File 1; Suzuki-Kamata et al., 2009).
57
58
59
60

61 Lines 342-343. I think it is the sum of internal variability and measurement errors.
62
63
64
65

Lines 354-356. The calculated standard errors indicate the measurement errors and the sum of internal variability between the block shape parameters. These values imply distinct evolution between the avalanche block lithofacies and PDC.

Line 371. It is necessary to fully understand which is the parameter on the abscissa. Is it a coarse-shape parameter, or the clast's diameter? You need to clarify this better, if it is a scatter-plot with two parameters describing a coarse shape in both axes. It makes no sense, it doesn't provide useful information.

Lines 376-382. The mean values increase for roundness from 1 to 1.7 and ellipse/ a/b from 0.2 to 2.7 (Table 5), while the values of Riley's circularity decrease. A regression characterizes the roundness vs. maximum Feret's diameter (Eq. 13 in Fig. 9) for the striations. The intersecting point c (Eqs. 13-14 in Fig. 9) with Feret's diameter <0.05 m and roundness around ~ 1.05 characterizes the inherited clast shape of the proximal block lithofacies generating striations and impact marks in the ridged debris-avalanche unit. We observed decreasing values of Riley's circularity related to Feret's diameter (Table 5).

revised Fig. 1. Eliminate Fourier Shape Analysis from the figure! This term has been removed.

Revised Fig. 3. These metric references, highlighted in pink, are not clear. Is it about blocks of 7-8 meters?? Based on this reference it would seem that they are 7-8 meters large. Anyway, if I'm not mistaken, in the foreground there is a 1.5 liter bottle of water, near a block. So the block would be no more than 2 m in diameter. These metric references have been considered in Figure 3.

revised Fig. 10: If the Feret ratio is a measure of the general form as it appears in table 2, and the Riley circularity is also a factor of the general form, the graph does not make much sense and the data in this case would be autocorrelated. The graph would make more sense if it was actually the Feret diameter. Or also the relationship between the Feret diameter of each particle and the Feret diameter i.e. of the largest particle present in the whole set (normalization), indicators of grain size. Revise this point or delete the figure. The Feret's diameter (m) have been considered. Figures 9B and 10B with no clear correlations (with $R^2 \leq 0.5$) that we attributed to the shape variations of block lithofacies and striations based on textural parameters have been removed according to reviewers 1 and 2.

It would be interesting to be able to consult the original data used to calculate the mean values and standard errors in supplementary material. See Supplemental file 2

revised Table 1. It seems to me that the same symbol has also been used for the depth of the grooves and also the height of the blocks! . In this case change symbols. These acronyms have been defined. The depth (d) of the grooves and striations are differentiated from the Height (H) of the blocks in Table 1.

revised Table 2. According to the definition of Feret Ratio in Tab.2, it is not a granulometry measurement, but rather a shape factor similar to elongation. [The Feret diameter has been considered.](#)

Revised Table 3. : The definition of Feret or Feret ratio, is one of the most important problems remaining in the paper. Observing the original figure, it is clear that it was a measurement of length in meters (m). Which makes much more sense than using a parameter in the x similar to the one in the y. See other comments and clarify this very important doubt. F_m . From the figure, it appears that F_m is half the Feret diameter at 90° of the Feret max.

[The Feret's Diameter \(\$FD\$ \), defined as the longest distance between two parallel tangential lines, has been considered in the figure of table 3.](#)

Perimeter roughness. This measure, determined by the relationship between the real perimeter and the convex hull perimeter, is not so sensitive to roughness and rather reflects irregularities in the order of roundness. [The Feret's Diameter \(\$FD\$ \), defined as the longest distance between two parallel tangential lines, has been considered in the figure of table 3. The roundness parameter has been considered.](#)

Revised Table 4 D. IMPORTANT!

Based on the methodology of Suzuki-Kamata et al. 2009, analyzing realistic granulometries, negative values of fractal dimension cannot come out. One possibility is that the distribution is inverted by mistake. Very abnormal granulometries for methodological reasons could also determine this type of results. Please check this very important point! It would be recommendable that at some point in the paper or in complementary material, details about the methodology used to construct the granulometric curves, would be given. Realistic and rigorous grain size, cannot be obtained from a photograph simply by measuring the apparent length of the major axis. It is necessary to use correct photographic shot geometries and a stereological method, such as Rosiwall intersection analysis, point

[Supplementary file 1 focus on the original data used to calculate the fractal dimension. The number of clasts used to obtain the distributions have been considered in Table 4. The negative values of fractal dimension have been removed in table 3 \(See Supplemental file 1\) and the standard errors \(\$<10^{-3}\$ \) related to photographic shot geometries have been considered \(lines 138-140\).](#)

revised Table 5. No Fourier analysis was performed in this work. Extraordinarily low values for being dimensionless shape parameters! Excellent! [This term has been removed. The standard errors of the scale and shape parameters have been considered. Supplementary file 2 focus on the original data used to calculate the mean values and standard errors of the shape parameters.](#)

My coauthors and I feel the revised manuscript is now ready for publication in JVGR.

K. Bernard, 21 August 2022

More information and support

FAQ: How do I revise my submission in Editorial Manager?

https://service.elsevier.com/app/answers/detail/a_id/28463/supporthub/publishing/

You will find information relevant for you as an author on Elsevier's Author Hub: <https://www.elsevier.com/authors>

FAQ: How can I reset a forgotten password?

https://service.elsevier.com/app/answers/detail/a_id/28452/supporthub/publishing/kw/editorial+manager/

For further assistance, please visit our customer service site: <https://service.elsevier.com/app/home/supporthub/publishing/>. Here you can search for solutions on a range of topics, find answers to frequently asked questions, and learn more about Editorial Manager via interactive tutorials. You can also talk 24/7 to our customer support team by phone and 24/7 by live chat and email.

#AU_VOLGEO#

To ensure this email reaches the intended recipient, please do not delete the above code

Highlights

A combined approach helps to correlate the block clusters of avalanche deposits.

Striations are associated with the subsequent pyroclastic density currents.

Abstract

We describe sedimentological variations of the block-rich debris avalanche deposits and associated pyroclastic density current deposits emplaced around AD 1802 from Tutupaca volcano in southern Peru. We use these exceptionally well-preserved features to document the collisional shearing contact between the avalanche and coeval pyroclastic density currents. Furthermore, we show how the first stages of the edifice collapse and *syn*-cataclastic emplacement process affect the block-size distributions.

With field observations, we describe imbricated block clusters, jigsaw cracks and striations related to elongated ridge structures on the deposit surface. Sedimentological and statistical methods (Fourier Shape analysis and Shape Preferred Orientation measured on 208 blocks and 566 mesoscale structures) help us to characterize the cataclastic gradient and establish the collisional relationships between different units. We determine that the proximal impacted deposits and block lithofacies from ridges may be related to distal block units around ~10 km run-out distance. Different block clusters indicate a kinematic transition between avalanche units to pyroclastic density currents. Block shape parameters help to differentiate rounded blocks resulting from matrix abrasion with and striated blocks from ridges related to proximal imbricated block clusters. From the statistical dataset, a few equations have been developed indicating a common cataclastic origin with a co-genetic evolution of block lithofacies during sequential *syn*-cataclastic emplacement.

The dome collapse is associated with a specific granular flow regime between avalanche and pyroclastic density currents with secondary reworking. Cyclic impact waves contribute to block cluster growth. Clusters are disaggregated during shock propagation. The inherited shapes of the block lithofacies with $a/b = 1.2-2$ and ellipse = 0.2-2.5 indicate the reworking by impact waves. A multidirectional switch to mass spreading in the median zone between 2 and 6 km may be considered with secondary flow and segregation waves. A basal frictional regime with striations is differentiated from collisional cataclastic flow, generating polymodal grooves during peak velocity at the flow front. Impact forces around $\sim 15.7 \times 10^{10}$ N are implied by suggested clast velocities around 8.86 m.s^{-1} and the transitional regime between avalanche units and pyroclastic density currents between 15.5 and 39.6 m.s^{-1} . An extensional disaggregation with the fractal dimensions (D) of the surrounded matrix between 0.6 and 2.8 characterizes the granular transport. A collisional shearing contact probably operated between avalanche units and pyroclastic density currents, which contribute to co-genetic evolution of block clusters from median to frontal distal zones. In the distal zone, abraded block clusters and tilted blocks are related to frontal reworking by impact wave.

The cataclastic gradient of avalanche units is correlated with the pyroclastic flow regime. Semi-quantitative analysis of block clusters provides information about *syn*-emplacement processes during

Conflict of Interest and Authorship Conformation Form

Please check the following as appropriate:

- All authors have participated in (a) conception and design, or analysis and interpretation of the data; (b) drafting the article or revising it critically for important intellectual content; and (c) approval of the final version.
- This manuscript has not been submitted to, nor is under review at, another journal or other publishing venue.
- The authors have no affiliation with any organization with a direct or indirect financial interest in the subject matter discussed in the manuscript
- The following authors have affiliations with organizations with direct or indirect financial interest in the subject matter discussed in the manuscript:

Author's name

Affiliation

Karine Bernard

LMV UCA OPGC, Campus Universitaire des Cézeaux, 6 avenue

Blaise Pascal, 63178 Aubière, France.

Benjamin van Wyk de Vries

LMV UCA OPGC, Campus Universitaire des Cézeaux, 6 avenue

Blaise Pascal, 63178 Aubière, France.

Pablo Samaniego

IRD, OPGC, Campus Universitaire des

Cézeaux, 6 avenue Blaise Pascal, 63178 Aubière, France.

Patricio Valderrama

Departemento de Ingenieria, Pontificia Univesidad

Catòlica del Perú, Lima, Perú.

Jersy Mariño

Instituto Geológico Minero y Metalúrgico (INGEMMET),

Observatorio Vulcanológico del Ingemmet, Barrio Magisterial Nro. 2 B-16, Umacollo, Arequipa, Perú.

AUTHORSHIP STATEMENT

Manuscript title: Collisional interactions and the transition between
lava dome sector collapse and pyroclastic density
currents at Tutupaca volcano (Southern Peru).

All persons who meet authorship criteria are listed as authors, and all authors certify that they have participated sufficiently in the work to take public responsibility for the content, including participation in the concept, design, analysis, writing, or revision of the manuscript. Furthermore, each author certifies that this material or similar material has not been and will not be submitted to or published in any other publication before its appearance in the *Hong Kong Journal of Occupational Therapy*.

Authorship contributions

Authorship contributions

Please indicate the specific contributions made by each author (list the authors' initials followed by their surnames, e.g., Y.L. Cheung). The name of each author must appear at least once in each of the three categories below.

Category 1

Conception and design of study: K. Bernard, B. van Wyk de Vries, P. Samaniego,
P. Valderrama, J. Mariño

acquisition of data: K. Bernard, B. van Wyk de Vries, P. Samaniego,
P. Valderrama, J. Mariño

analysis and/or interpretation of data: K. Bernard, B. van Wyk de Vries, P. Samaniego,
P. Valderrama, J. Mariño

Category 2

Drafting the manuscript: K. Bernard, B. van Wyk de Vries, P. Samaniego,
P. Valderrama, J. Mariño;

Category 3

Approval of the version of the manuscript to be published (the names of all authors must be listed):

K. Bernard, B. van Wyk de Vries, P.Samaniego,
P. Valderrama, J. Mariño
_____, _____, _____, _____, _____



Acknowledgements

All persons who have made substantial contributions to the work reported in the manuscript (e.g., technical help, writing and editing assistance, general support), but who do not meet the criteria for authorship, are named in the Acknowledgements and have given us their written permission to be named. If we have not included an Acknowledgements, then that indicates that we have not received substantial contributions from non-authors.

This statement is signed by all the authors (a photocopy of this form may be used if there are more than 10 authors):

Author's name (typed)	Author's signature	Date
K. Bernard	 K. BERNARD	22/04/2022
B. van Wyk de Vries	_____	_____
P.Samaniego	_____	_____
P. Valderrama	_____	_____
J. Mariño	_____	_____



[Click here to access/download](#)

Supplementary Material

shape parameters block clusters supplemental file 2.xls



1 **1. Introduction**

2

3 Volcanic debris-avalanche deposits are often associated with pyroclastic density currents and lahar deposits
4 (*i.e.* Mount Saint Helens in the USA, [Glicken, 1986](#)), suggesting interactions during flow propagation. The
5 stratigraphic relationships between the associated *syn*-eruptive volcanic deposits are described, implying
6 differential kinematic between the mass flow such as striations and grooves on clast faces related to dome-
7 collapse generating avalanche deposits interstratified between pyroclastic units (Mono Craters, CA, [Dennen
8 et al., 2014](#)); matrix transformations into lahar deposits (Misti in Peru, [Bernard et al., 2017](#)). Block lithofacies
9 are rarely used to characterize the differential movements inside the mass flow during *syn*-eruptive collapse.
10 A basal frictional regime with striations is differentiated from an upper collisional cataclastic flow for block
11 lithofacies (*e.g.* Parinacota and Ollagüe in Chile, [Clavero et al., 2002](#); [Clavero et al., 2004](#); El Zaguán,
12 Mexico, [Caballero and Capra, 2011](#)).

13 Lava dome extrusion produced block lithofacies may be mixed with matrix-rich debris-avalanche deposits
14 (Mount Saint Helens, [Glicken 1986](#); Parinacota in Chile, [Clavero et al., 2002](#); Tutupaca in Peru, [Samaniego
15 et al., 2015](#); [Valderrama et al., 2016](#)). Different avalanche structures are identified with such block
16 lithofacies: (1) *torevas* that are large blocks ($L > 100$ m), which occur in the proximal zones and could
17 constitute up to ~30% of the debris avalanche deposits (Socompa in Chile, [Davies et al., 2010](#)). (2) Type A
18 hummocks that are large cataclased blocks ($H < 80$ m, $w < 300$ m, $L < 400$ m, Mount Saint Helens, [Voight et
19 al., 1981](#); [Glicken, 1998](#); Jocotitlán in Central Mexico, [Siebe et al., 1992](#); Parinacota and Taapaca in Chile,
20 [Clavero et al., 2002](#); [Clavero et al., 2004](#)) with steep slopes. (3) Longitudinal or transverse ridges ($H = 10$ -30
21 m, [Shea and van Wyk de Vries, 2008](#); [Dufresne and Davies, 2009](#); [Andrade and van Wyk de Vries, 2010](#)),
22 that are attributed to deflection of the mass flow ([Valderrama et al., 2018](#)). The alignment of blocks or
23 isolated blocks between 0.01 and 1000 m can be observed in some debris avalanche deposits (Socompa, [van
24 Wyk de Vries et al., 2001](#); [Shea and van Wyk de Vries, 2008](#)). The frontal lobes thrust the large blocks in
25 distal zones (Jocotitlán, [Siebe et al., 1992](#)) showing fluidization with matrix transformations into lahars
26 (Perrier in French Massif Central, [Bernard and van Wyk de Vries, 2017](#)). Different mesoscale structures have
27 been described related to specific kinematic context such as gravitational flank collapse with an initial
28 dilation of jigsaw-fit textures (Mount Saint Helens, [Glicken, 1986](#)), abrasion and striations along fault planes
29 ([Mehl and Schmincke, 1999](#)), collisional textures during transport (El Zaguán in Mexico, [Caballero and
30 Capra, 2011](#)), and impact waves with pseudotachylite and gouge along avalanche fault zones (Pichu Pichu in
31 Peru, [Legros et al., 2000](#); Mont Dore in French Massif Central, [Bernard and van Wyk de Vries, 2017](#)).

32 *Syn*-eruptive collapses of a volcanic edifice and volcano-sedimentary processes have been well documented
33 at Las Derrumbadas Volcano, Mexico ([Guilbaud et al., 2022](#)), Panum Crater, (Mono Crater, CA, [Dennen et
34 al., 2014](#)) and Tutupaca volcano in southern Peru ([Samaniego et al., 2015](#); [Valderrama et al., 2016](#); [Mariño et
35 al. 2021](#)). This volcano hosts probably the well-preserved and displayed lava dome related debris avalanche

and pyroclastic density current features that are young and little altered by the climate or human interference. Two volcanic avalanche units exposed in the northeastern part of the Tutupaca collapsed edifice are interstratified with the pyroclastic density current deposits (Samaniego et al., 2015). Block-rich ridge structures have been attributed to granular segregation and differential block velocities in the flowing mass, suggesting the interactions between debris-avalanche units and the associated PDC deposits.

In this study, we show how semi-quantitative sedimentological analysis of the block lithofacies and mesoscale structures associated to these exceptionally well-preserved volcanic deposits provide information about *syn*-emplacement processes during a collapsing dome generating pyroclastic density currents. To facilitate the reading of this study, we provide a list of the acronyms in Table 1.

2. Collisional interactions between volcanic-debris avalanche and pyroclastic density currents: a State-of-the-Art

The volcanic debris avalanche deposits are commonly associated with PDC. Mount Saint Helens in the USA (Crandell et al., 1984; Glicken, 1986), Bezymianni in Kamchatka (Siebert et al., 1987), Soufrière in Guadeloupe (Boudon et al., 1984) show several sequences of lava dome collapses associated with decompression to the co-magmatic deposits in *syn*-eruptive sequences. The hot volcanic debris-avalanche deposits, gravitational mass spreading ($v = 50-70 \text{ m.s}^{-1}$) of the collapsed edifice, interacted with the blast-generated the PDC, transport of the fluidized mixture of clasts and gas ($v \geq 100 \text{ m.s}^{-1}$, Soufrière, Boudon et al., 1984; Mount Saint Helens 1980, Glicken, 1986; Bezymianni 1956, Saint Augustine, Siebert et al., 1987). The PDCs are interstratified between the debris avalanche units, related to cyclic volcanoclastic sedimentation. Cyclic phases can be differentiated: precursor stages with seismes and localized collapses with hydrothermal alteration, large collapse of altered lava-dome edifice with explosion and the blast-generated the PDC including an open conduit, and different post-collapse eruption. Volcanic lateral blast is associated to the successive shock waves during collapse, with ballistic clasts and sliding blocks generating internal shock structures. Transformations of the debris-avalanche deposits into lahars ($v = 30-40 \text{ m.s}^{-1}$) by dewatering have been observed during initiation of pyroclastic flow such as Mount Saint Helens (Glicken, 1986).

Deposit structures have been formed by interactions between the moving avalanche and the superposed PDC, implicating a strong frictional contact. We observed aggregation of lava block clusters (Taranaki, Zernack et al., 2009) with brecciation and curvilinear surfaces related to blocky morphology interactions, pyroclastic slump blocks with progressive disaggregation of blocks, fingering segregation related to ridge structures (Tutupaca, Samaniego et al., 2015; Valderrama et al., 2016), striations and flow bands (Lastaria in Chile, Naranjo and Francis, 1987) with distal digitations related to weak pyroclastic material.

Different generations of striations have been described related to sliding mode transport during interactions

71 between no-cohesive avalanche lithofacies and PDC: striations of the bedrock in scar (Mount Saint Helens,
72 [Glicken, 1986](#)); grooves and striations at the base and the underlying substratum; and parallel grooves and
73 furrow at the base and the upper part of faulted megablocks (Gran Canaria, Spain, [Mehl and Schmincke,](#)
74 [1999](#)). We differentiate an upper collisional regime with impact marks at the surface of block lithofacies
75 (Parinacota and Ollague in Chile, [Clavero et al., 2002](#); [Clavero et al., 2004](#)). Impact marks and linear trends
76 appear concentrated on one side of blocks, showing conchoidal fractures related to collisional interactions
77 between the blocks.

78 We examine how block lithofacies of volcanic debris avalanche deposits interact with PDC to generate block
79 clusters and grooves with striations related ridges structures. We show how semi-quantitative
80 sedimentological analysis of the block lithofacies and mesoscale structures provide information about *syn*-
81 emplacement processes such as the force F of impact of clasts onto block surfaces and the clast velocity for
82 making impact marks ([Clavero et al., 2002](#)).

84 **3. Analytical methods**

85
86 From the field observations on the debris-avalanche units, we have described the textural variations of the
87 block lithofacies assemblages and assessed their relationships to avalanche fault zones. A semi-quantitative
88 sedimentological analysis was conducted to characterize block distributions ([Table 2](#)). From these data, we
89 were able to differentiate the block lithofacies in each zone associated with cataclastic gradient between the
90 avalanche units and pyroclastic density current deposits ([Samaniego et al., 2015](#); [Valderrama et al., 2016](#)). To
91 facilitate the reading of this study, we provide a list of the acronyms in [Table 1](#).

93 *3.1. Field observations and outcrop analysis*

94
95 The lithology of different outcrops were identified from proximal to distal zones to characterize the
96 discontinuous block-rich lithofacies, related to interactions between volcanic avalanche and pyroclastic
97 density current deposits. From field observations and Google Earth imagery, the block-rich avalanche units
98 were described and mapped according to stratigraphic and geomorphological context and avalanche
99 structures ([Samaniego et al., 2015](#); [Valderrama et al., 2016](#)).

100 Quantitative morphological data such as area (S), thickness (T) and volume ($V = ST$; [Table 1](#)) on the surface
101 avalanche deposits are calculated from the mapped surfaces and georeferenced Google Earth images
102 ([Samaniego et al., 2015](#); [Valderrama et al., 2016](#)). These morphological data are compared to other avalanche
103 deposits worldwide such as those emplaced around Mount Saint Helens and Mount Shasta in the USA
104 ([Crandell et al., 1984](#); [Glicken, 1986](#)), Bezymianni in Kamchatka ([Siebert et al., 1987](#)), Parinacota in Chile
105 ([Clavero et al., 2002](#)), Soufrière in Guadeloupe ([Boudon et al., 1984](#)) and Mont Dore in French Massif

106 Central (Bernard and van Wyk de Vries, 2017). From these examples, we correlate the morphological data
107 with the structural units of avalanche deposits, implying interactions between lava dome sector collapse and
108 pyroclastic density currents. The contacts between the block lithofacies and matrix textures of volcanic
109 debris-avalanche deposits with interstratified PDC were analyzed. Lithostratigraphic sections were
110 established and correlated with textural variations.

111 The use of the Shape Preferred Orientation 2003 software (Fig. 1A, SPO, Launeau and Robin, 2005)
112 provided a semi-quantitative description of block avalanche units, allowing us to estimate imbrication of 508
113 blocks and block axial distributions with the inertia and intercepts method. Image analysis of the block
114 lithofacies and mesoscale structures provide relative information because photographs can be affected by
115 perspective. Two-dimensional shape parameters of blocks, such as the a/b ratio (the largest axis / minor axis)
116 and sectional ellipse values from system of linear equations (see Launeau and Robin, 2005 for mathematical
117 definitions), have been calculated, to characterize block fabric related to *syn*-emplacement structures
118 (Bernard, 2015; Bernard and van Wyk de Vries, 2017; Bernard et al., 2019), together with striations and
119 grooves in blocks. Ellipse/ a/b values contribute to establish textural classes of avalanche fault zones (~2.14
120 for the plane collapse, 1.75 to 2 for the crushing, $a < 1.7$ for the thermal effect of fragmentation, Bernard et
121 al., 2019). Mesostructures such as fractures and striations from 2 mm to 20 cm were also analyzed.

122

123 3.2. Sedimentary analysis

124

125 From SPO analysis (Launeau and Robin, 2005) of the blocks, the fractal distributions were used to compare
126 transport and cataclastic process acting on each avalanche unit. Each cumulative frequency is plotted *versus*
127 clast long-axis on double-logarithmic graphs. Fractal dimensions h and D of size distributions were estimated
128 from the power regressions (Table 4; see Supplemental File 1; Suzuki-Kamata et al., 2009). The cumulative
129 curves of the clast-size distributions *vs.* a/b (Fig. 8) were compared to distinguish the block avalanche units
130 from proximal to distal zones. The calculated block-size distributions estimated from 41 outcrop photographs
131 with the inertia and intercepts methods using the SPO analysis (from metric-size blocks to clasts >10 cm;
132 Fig. 8B; Launeau and Robin, 2005). The longest axis of 404 block outlines were measured and counted per
133 image area from the photographs. The normalized frequency histograms (Launeau and Robin, 2005) were
134 produced by grouping the longest axis of blocks (cm) into 100-cm bins (number of size intervals) and
135 normalizing the number of occurrences in each bin to the total number of measurements from automatic
136 image analysis. The sectional effects have been considered (Launeau and Robin, 2005). These data contribute
137 to differentiate the effect of cataclasis between each fraction correlated with different structural units from
138 proximal to distal zones. The subdued blocks and clasts below 10 cm are not considered related to resolution
139 limits.

140 The shape analysis using the ImageJ Plugin “Gold morph” has been applied to 404 blocks and 635 striations

141 of the avalanche units to compute minor and major axis length, Feret's diameter defined as the longest
 142 distance between two parallel tangential lines, perimeter and convex perimeter, radii of the smallest inscribed
 143 and largest circumscribed circles (Fig. 1B; Table 3; Crawford and Mortensen, 2009). From these data, we
 144 calculate the a/b ratio, the roundness defined as the ratio of the perimeter to convex perimeter, and the Riley's
 145 circularity, the square root of the ratio of the diameter of the largest inscribed circle to the diameter of the
 146 smallest circumscribed circle of the volcanic clast (Table 3, Blott and Pye, 2008; Bernard, 2015). The values
 147 of Riley's circularity are less than 1 for the non-spherical volcanic clasts (Table 5).

148 To characterize the two-dimensional shape of mesoscale structures, we took 5.9 megapixel photographs of
 149 abraded flat surfaces of two blocks with a digital camera. A digital camera (6.2-18.6 mm lens, 35-105 mm
 150 focal length) image at a camera distance of <20 cm had a standard error for mean distortion around $\sim 10^{-3}$. All
 151 the striations observed in the median zone have been quantified by using high-resolution images (3648 X
 152 2736 pixels) of two block faces. Abraded flat surfaces of the two megablocks on these scales contribute to
 153 preserve geometries of these grooves and striations with circular depressions (~ 1 -5 cm depth, 2-3 mm wide).
 154 These are enough to generate semi-quantitative analysis using the ImageJ Plugin "Gold morph" and SPO
 155 (566 mesoscale structures, Launeau and Robin, 2005; Blott and Pye, 2008; Crawford and Mortensen, 2009).
 156 The roundness, the Riley's circularity, the a/b ratio, ellipse, fractal D -values of each mesoscale structure have
 157 been calculated. The calculated standard errors characterize the shape variations between the blocks rather
 158 than the measurements' uncertainty. Moreover, the calculated standard errors for image analysis are between
 159 0.03 and 0.3 for a/b ratio and around ± 0.9 for ellipse values (Launeau and Robin, 2005; Table 5).

160 Several statistical regressions (Eqs. 1-21 in Figs. 2 and 8-10) have been established to characterize the
 161 evolution of block shape and striations related to cataclastic processes between the volcanic debris-avalanche
 162 units and pyroclastic density current deposits. Figure 9 shows the evolution of the roundness with Feret's
 163 diameter for block lithofacies and striations. Figure 10 shows the evolution of the roundness with Feret's
 164 diameter for block clusters. The intersecting points between few regressions indicate similar values of shape
 165 parameters related to the inherited clast shape for lava blocks and co-genetic relationships between block
 166 lithofacies.

167 Statistical and shape parameters were compared with those from other avalanche units in the Andean Central
 168 Volcanic Zone such as the Pichu Pichu debris avalanche deposit, and the matrix of the ridges from the
 169 Tutupaca volcanic debris-avalanche deposits (Bernard, 2015; Valderrama et al., 2016; Bernard et al., 2019).

170 The impact of clasts onto block surfaces (Clavero et al., 2002) can be approximated as $r = 0.5a^2/h$ with r ,
 171 radius of spherical portion of clasts; a , radius of hemispherical damage zone, and h , distance that penetrated
 172 into the block. The force F of impact is given by Clavero et al. (2002):

$$173 F = \Pi a^2 \rho_0$$

174 where ρ_0 is the hardness of the material. The clast velocity for making impact marks can be estimated by
 175 using $V = (0.5 \Pi \rho_0 / Mr)^{1/2} a^2$ with M , the mass of the rock (Clavero et al., 2002). The avalanche velocity in the

176 middle zone is considered by using $v = (2gH)^{1/2}$.

177 A combination of several semi-quantitative methods has been used to determine (Table 1): (1) the links
 178 between the different block-rich units related to the debris avalanche and the associated pyroclastic density
 179 currents; (2) the quantitative sedimentary comparisons of the block lithofacies to define the conditions
 180 generating these deposits; (3) the in-motion controls and the dynamic cataclasis during the differential
 181 sedimentary emplacement between the volcanic debris-avalanche units and the pyroclastic density current
 182 deposits.

183

184 **4. Geological and geomorphological context of the study area**

185

186 *4.1. Tutupaca volcanic complex and the geomorphological context*

187

188 The Tutupaca volcanic complex (~5815 m on above sea level, Fig. 3) is composed by three edifices: an
 189 eroded basal edifice (Lower to Middle Pleistocene, Marino et al., 2021) with strong hydrothermal alteration;
 190 the Western Tutupaca peak, which was eroded by the late Pleistocene glaciers, and the Holocene Eastern peak
 191 composed of seven coalescing lava domes (Holocene, domes I to VII, Fig. 3B, Samaniego et al., 2015;
 192 Valderrama et al., 2016; Marino et al., 2021), constructed on the older hydrothermally-altered basal edifice.
 193 The activity of the recent domes is historic (about 218 ± 14 calBP), and little altered by the arid, stable, cold
 194 climate, or by human activity, apart from a few small tracks and limited mining exploration excavations. The
 195 area is mostly wild, and in its natural state. The lava domes of the Eastern Tutupaca peak are cut by a
 196 horseshoe-shaped amphitheater open to the northeast, with an orthogonal direction to the N140° regional
 197 faults. From this, debris avalanche and pyroclastic density current deposits extend, are preserved with very
 198 little modification from their initial state (there is some limited frost shattering, and ice related solifluxion).

199 Geomorphological parameters on the surface avalanche deposits associated with PDC are calculated and
 200 compared to other avalanche deposits worldwide such as those emplaced around Mount Saint Helens and
 201 Mount Shasta in the USA (Crandell et al., 1984; Glicken, 1986), Bezymianni in Kamchatka (Siebert et al.,
 202 1987), Soufrière in Guadeloupe (Boudon et al., 1984). Impact marks of Parinacota debris avalanche in Chile
 203 (Clavero et al., 2002) and pseudotachylite impact in French Massif Central (Bernard and van Wyk de Vries,
 204 2017) are considered. A relationship between area (A) and volume (V) is calculated for the Tutupaca units
 205 with $A = 28.07 V^{1.01}$ (Eq. 1 in Fig. 2). These are compared to the power regressions of other volcanic debris-
 206 avalanche deposits (Eqs. 2-4 in Fig. 2, Glicken, 1986; Clavero et al., 2002; Legros, 2002; Bernard and van
 207 Wyk de Vries, 2017). We differentiate an intersecting point A with area around ~140 and 180 km² and volume
 208 between 5 and 7 km³.

209

210 *4.2. The Paipatja debris-avalanche deposits*

211

212 Samaniego et al. (2015) described the Paipatja debris avalanche, exposed in the northeastern part of the
 213 Tutupaca volcano between the amphitheater and the Paipatja plain ($L = 6-8$ km, $S = 12-13$ km², $T = 25-40$ m,
 214 Samaniego et al., 2015; Valderrama et al., 2016). Stratigraphic and textural variations are correlated to the
 215 syn-emplacement structures. The hydrothermally rich debris avalanche deposit (HA-DAD, $L = 6-8$ km, $V < 1$
 216 km³; $H/L = 0.17-0.23$, Samaniego et al., 2015), that involved large quantities of the basal edifice, is
 217 characterized by torevas ($H = 20-40$ m, $L = 1.5$ km), long lateral levees ($L = 1.5$ km) and hummocky-
 218 structures ($L = 200-800$ m, $H = 20-40$ m) up to 4-6 km from the scar (Samaniego et al., 2015; Valderrama et
 219 al., 2016).

220 Block ridge structures and levees are observed between 2 and 6 km from the amphitheater (Valderrama et al.,
 221 2016). In the median zone, elongated and sub-parallel ridge structures ($w = 5-10$ m, $H = 2-5$ m, $L = 150-400$
 222 m, Fig. 3A), regularly spaced, are related to interstratified pyroclastic density current deposits between two
 223 avalanche units, implying a *syn-collapse* explosive eruption at Tutupaca volcano (Samaniego et al., 2015).
 224 The hydrothermally rich debris avalanche deposit is covered by Paipatja pyroclastic density current deposits
 225 (P-PDC, ~218 aBP, sections B to E in Fig. 3A).

226 A dome-rich debris-avalanche deposit (DR-DAD of Samaniego et al., 2015) overlain the P-PDC unit in the
 227 median zone (section B in Fig. 3). Cross-sections within the ridge structures reveal the dipping and
 228 undulating contacts between the P-PDC units and the DR-DAD (section B in Fig. 3A). The P-PDC, on the
 229 upper part of HA-DAD, appears thickest between the ridge structures and around the largest blocks
 230 (Valderrama et al., 2016). We have observed dome fragments (from centimeters to several meters in size),
 231 such as metric-size dacitic blocks and prismatic jointed blocks showing inherited jigsaw-cracks,
 232 cataclastic and shearing structures. The abraded and sub-rounded blocks are subdued in the underlying
 233 avalanche deposit and PDC.

234 The Tutupaca volcanic debris-avalanche deposits show different units with specific granular assemblages
 235 (30% of HA-DAD and 70% of DR-DAD, Valderrama et al., 2016). Dense blocks (3-20 cm in diameter) and
 236 bombs from the P-PDC unit (20-40%) have highly similar chemical content (~65-68 wt.% SiO₂, Samaniego
 237 et al., 2015), similar to the brecciated lava domes. A progressive decrease in block-size is observed with
 238 distance. Large blocks (~0.5-1 m in diameter) are occasional. The few distal blocks (>1 m in length)
 239 surrounded by P-PDC unit are associated to the underlying avalanche deposit.

240

241 4.3. The syn-emplacement block lithofacies

242

243 Using the Google Earth imagery, we differentiate different block lithofacies from proximal to distal zones.
 244 The eastern flank collapse of the Tutupaca volcano shows at the summit two brecciated zones related to lava
 245 dome collapse (domes V to VII in Fig. 3B, Fig. 4A). We observe along the East crest (1 in Fig. 4A) angular

246 dome fragments adjacent to the PDC (in red in Figs. 3A and 4A) without preferential orientation, and on the
247 west side (2 in Fig. 4A) an impacted and crushed zone showing imbricated block clusters with tabular planar
248 surfaces. The long axis of 56 blocks are tilted N112E. In the median zone, block ridge structures show an
249 isolated polyhedral block (white arrow in Fig. 4B), which exhibits planar surfaces with angular edges. We
250 observe in downstream sigmoid fish of clasts, which appears disaggregated and truncated in N40E, related to
251 the interactions between avalanche and the blast-generated the PDC (Fig. 4B). The isolated distal blocks (>1
252 m in length, Fig. 4C) surrounded by P-PDC unit are transverse with extensional lateral spreading (N176E,
253 Fig. 4C).

254 The textural and sedimentological variations of the block avalanche lithofacies (HA-DAD and DR-DAD) are
255 described with associated volcanic deposits to correlate *syn*-emplacement process between volcanic debris-
256 avalanche units and pyroclastic density current deposits.

257

258

259 5. Results

260

261 The SPO analysis of the block lithofacies contribute to a semi-quantitative description of block deposits. The
262 comparison of each block lithofacies with cumulative curves and fractal distributions helps to distinguish the
263 deposits. The analysis of the block shapes has enabled us to identify the inherited structures and the
264 relationships between the proximal and distal block clusters.

265

266 5.1. Block lithofacies

267

268 In the Paipatja DAD, we have observed block clusters and block avalanche lithofacies with a specific
269 distribution on and between blocks. From proximal to distal zones, the block characteristics were quantified
270 using the software ImageJ and SPO analysis (>400 blocks, Launeau and Robin, 2005). We characterized the
271 localized mesoscale structures observed on few blocks associated with the ridged structures.

272

273 5.1.1. Block clusters lithofacies of DR-DAD

274 Imbricated block clusters are localized under the collapse scar (A in Figs. 3A and 4A). The dacitic dome
275 fragments (from centimeters to several meters in size) present similar chemical characteristics (64.5-65.9 wt.
276 % SiO₂, Samaniego et al., 2015). We observed impacted blocks with planar fractures and undulated borders
277 (Fig. 5A), and tilted blocks in imbricated piles. Inherited clasts are observed with jigsaw-fractured breccias
278 showing polymodal distribution of the clasts and ellipse/ a/b = 5.1 (Fig. 5B). Block-rich ridge structures of the
279 Paipatja DAD (B in Fig. 3A) contain abraded and sub-rounded blocks, which are also found in the underlying
280 avalanche deposit and P-PDC (ellipse/ a/b = 2.3-2.6 in Fig. 5C). There are also impacted blocks (Fig. 5D)

281 showing polymodal distribution of the clasts. In the Paipatja plain, abraded and sub-rounded blocks are found
 282 isolated at the front of P-PDC (Fig. 3). Along the lateral levee, in the proximal zone, we have observed large
 283 blocks with sigmoidal jigsaw-breccias (Fig. 5E) and a bimodal clast distribution. Angular lava blocks (~1 m
 284 in length) are impacted between aligned and subdued blocks (Fig. 5F), which exhibit planar surface with
 285 conchoidal fractures or abraded surface with striations. We differentiate block clusters and ridged avalanche
 286 units (ellipse/ a/b = 2.3-2.5, DR-DAD, Fig. 5G) from imbricated block clusters (ellipse/ a/b = 1.74) and
 287 subdued and tilted blocks in the distal zone (ellipse/ a/b ~2.12, PDC, Fig. 5H).

288 289 *5.1.2. Block avalanche lithofacies*

290 Some transverse blocks appear isolated or aligned in N30° (DR-DAD, Figs. 3B and 6A), parallel to the
 291 elongated depressions. We observed sub-rounded faces with striations in upstream and planar faces with
 292 conchoidal fractures in downstream. Along the lateral levee, we described quenched and cracked surfaces in
 293 the upper part with jigsaw-fit texture and imbricated subangular clasts along basal contact of blocks (Fig.
 294 6B). A large polyhedral block (~3 m high and ~5 m length, HA-DAD, Fig. 6C) on the ridge crest presents an
 295 oriented abrasion: sub-rounded face in the front and planar face in the downstream. In the PDC deposits, a
 296 bimodal distribution of the surrounded clasts is quantified. The sub-rounded lava block displays two distinct
 297 surfaces: a quenched and cracked surface in the upper part and an altered vitreous phase in the lower part. A
 298 distal sub-rounded block, surrounded by the P-PDC deposits, appears isolated (Fig. 6D) with bimodal
 299 distribution of the surrounded clasts related to the PDC deposits. Subdued blocks exhibit abraded surfaces
 300 with striations.

301 302 *5.1.3. Grooves and striations*

303 At 5.5 km from the collapse scar, a few blocks associated with the ridge structures (Fig. 7A; Valderrama et
 304 al., 2016) exhibit grooves and striations with roughly circular depressions on the upstream, abraded face.
 305 These localized mesoscale structures are often irregular and grouped in the lower part of the abraded and
 306 striated surfaces. The largest striations (>3 cm wide) are parallel to each other (at 3.19°, Fig. 7) and observed
 307 in the upper part of the block face. There are small striations perpendicular to the grooves (Fig. 7B). Grooves
 308 or furrows 1-5 cm depth ranged from roughly circular (<5 cm in diameter) to elliptic (~8-15 cm for longest
 309 axis) in shape. Fractal D values, calculated from exponent h of power regressions (100 striations, Table 4;
 310 Suzuki-Kamata et al., 2009), are 1.09 in the 8.4-46.4 cm mark-size range.

311 The macroscopic characteristics of grooves and striations with circular depressions were used for the shape
 312 analysis with the software ImageJ and SPO analysis (566 mesoscale structures, Launeau and Robin, 2005).
 313 Grooves and striations show polymodal distributions, with ellipse/ a/b around ~5.1-5.9 (Fig. 7A-B). In the
 314 lower part of the block face, basal striations (~2-3 mm wide) with perpendicular diaclasis are differentiated.
 315 Fractal D values, calculated from exponent h of power regressions (90 striations, Table 4, Suzuki-Kamata et

316 al., 2009), are 0.67 in the 5.2-20.96 cm mark-size range.

317

318

319 5.2. Sedimentary characteristics of block lithofacies

320

321 Sedimentary characteristics of block lithofacies were compared with fractal D values to distinguish textures
 322 in the block avalanche units (HA-DAD, DR-DAD) and PDC deposits from proximal to distal zones. Block
 323 lithofacies of HA-DAD are hydrothermalized and cataclased with jigsaw-cracks. These are angular to
 324 subangular in PDC (20-30% of HA-DAD, Samaniego et al., 2015). We differentiate imbricated blocks with
 325 jigsaw structures in zones A and C (Fig. 3A), the abraded and subdued blocks observed in ridges structures
 326 and the distal zone (F in Fig. 3A), and the dacitic block lithofacies in zones D and E. The cumulative curves
 327 of block-size distributions vs. a/b are compared to distinguish block lithofacies in different zones, which are
 328 characterized by five logarithmic regressions (Eqs. 5-9 with $R^2 > 0.9$ in Fig. 8A). These are compared to the
 329 logarithmic regressions of the impact breccias in French Massif Central (Eq. 12 in Fig. 8A; Mont Dore,
 330 Bernard and van Wyk de Vries, 2017). The intersecting points a to d with a/b between 2.5 and 4.7 imply a co-
 331 evolution between the grooves and striations (Eqs. 10-11 with $R^2 > 0.9$ in Fig. 8A) and the ridged debris-
 332 avalanche unit (Eq. 6), in accordance with the field observations. We differentiated the hydrothermalized
 333 matrix (HA-DAD) from the breccia matrix (DR-DAD) showing sandy-gravel lithofacies of the red matrix
 334 with few angular clasts ($< \text{cm}$, Bernard, 2015; Valderrama et al., 2016).

335 The effect of cataclasis is shown by a decrease in the content of the smallest fractions ($< 100 \text{ cm}$, Fig. 8B) of
 336 block lithofacies ($< 18\%$), an increase in the striation ratio (25 to 45%), together with a concomitant high ratio
 337 in amount of block clusters (~ 20 to 40%). The variations of these data are correlated with different structural
 338 units from proximal to distal zones. The basal striations appear differentiated (Table 4). A specific clast-size
 339 fractal distribution is calculated in the range between 6.7 and 539 cm. The mean fractal D value, calculated
 340 from exponent h of power regressions, is around ~ 1.28 in the 11.4-40.3 cm clast-size range (Table 4; see
 341 Supplemental File 1; Suzuki-Kamata et al., 2009). The distal block lithofacies present the highest D values
 342 around ~ 1.83 compared to the proximal ridged deposits around ~ 1.64 . These are differentiated from the
 343 surrounded matrix between 0.64 and 2.84 in the 0.0016-6.4 clast-size range. The mean fractal D value of
 344 striations is around ~ 0.62 in a range from 5.9 to 44.6 cm.

345

346 5.3. Block shape parameters

347

348 Shape analysis using the software ImageJ and SPO analysis (404 blocks from the HA-DAD and DR-DAD,
 349 635 striations; Launeau and Robin, 2005; Blott and Pye, 2008; Crawford and Mortensen, 2009) has been
 350 applied to compare shape parameters of blocks from proximal to distal zones, together with striations and

351 grooves in blocks. This comparison is intended to characterize the cataclastic evolution with co-genetic
 352 relationships between volcanic debris-avalanche units and P-PDC, including the inherited clast shape for lava
 353 blocks. The mean values of a/b ratio and ellipse ($\sim 1.7 \pm 0.03$ and 3.5 ± 0.15 , Table 5) are different from the
 354 clasts observed in the matrix of ridged units (DR-DAD, $\sim 1.69 \pm 0.05$ and 2.72 ± 0.09 , 1891 clasts from SPO
 355 analysis, Bernard, 2015). The calculated standard errors indicate the measurement errors and the sum of
 356 internal variability between the block shape parameters. These values imply distinct evolution between the
 357 avalanche block lithofacies and PDC.

358 5.3.1. Avalanche block lithofacies

360 We distinguish an inherited clast shape for lava blocks with $a/b = 0.9$ and ellipse = -3.5 implying textural
 361 relationships between the block lithofacies of HA-DAD and DR-DAD. Three regressions characterize the
 362 roundness vs. maximum Feret's diameter (Eqs. 13-17 in Fig. 9) for the block lithofacies. Two regressions
 363 (Eqs. 14-15 in Fig. 9) characterize the block lithofacies observed in the proximal and median zones. These
 364 values are compared to the breccias forming the ridged avalanche matrix (HA-DAD and DR-DAD) and the
 365 distal lobe of the Pichu Pichu debris-avalanche deposit (Eqs. 14-15 and 17 in Fig. 9; Bernard, 2015).

366 5.3.2. Distal block lithofacies

368 Three points of intersection indicate similar values of roundness for different zones of cataclasis ($a-c$ in Fig.
 369 9A). We distinguish an inherited clast shape with roundness around ~ 0.9 (a , Fig. 9), indicating textural
 370 relationships between the tilted distal blocks (PDC) and the blocks from the ridges, close to those of the
 371 sheared lava breccias in the distal lobe of the Pichu Pichu debris-avalanche deposit. The intersecting points b
 372 and c with roundness between 1.05 and 1.08 imply a co-evolution between the impacted blocks (Eq. 14)
 373 observed in the proximal and distal zones and the sheared sigmoid along the lateral levee (Eq. 15 in Fig. 9).

374 5.3.3. Grooves and striations

376 The values of $a/b = 3.2$ and ellipse = 15 are correlated to a co-genetic evolution between the grooves and
 377 striations, the blocks from ridges and the distal, impacted blocks (PDC). The mean values increase for
 378 roundness from 1 to 1.7 and ellipse/ a/b from 0.2 to 2.7 (Table 5), while the values of Riley's circularity
 379 decrease. A regression characterizes the roundness vs. maximum Feret's diameter (Eq. 13 in Fig. 9) for the
 380 striations. The intersecting point c (Eqs. 13-14 in Fig. 9) with Feret's diameter < 0.05 m and roundness around
 381 ~ 1.05 characterizes the inherited clast shape of the proximal block lithofacies generating striations and
 382 impact marks in the ridged debris-avalanche unit. We observed decreasing values of Riley's circularity related
 383 to Feret's diameter (Table 5).

384 5.4. Block clusters and shape variations

385

386

387 More than six cluster structures have been described with the shape analysis using the software ImageJ and
388 SPO analysis from 312 blocks in the unconsolidated avalanche matrix from the HA-DAD (Fig. 10). Lava
389 block clusters (~30-70 vol.%) from 40 cm to 5 m in diameter are impacted and thrust in unconsolidated
390 avalanche matrix. The a/b ratio related to ellipse values show increasing values for the impacted jigsaw-
391 clusters; and for the tilted block in the distal zone. Similar characteristics appear for the striated blocks from
392 the ridges and the distal clusters. Similar ellipse values are calculated between proximal jigsaw breccias and
393 the tilted and impacted blocks in the distal zone (ellipse = 0.7); between distal clusters (ellipse = 1-1.8) or
394 between tilted blocks in the distal zone (ellipse = 2.7). *Syn-cataclastic* emplacement of block clusters with a
395 co-genetic evolution of shape parameters may be envisaged.

396 The roundness is high (>1) for the block clusters, close to those of the experimental crushed stones (Janoo,
397 1998). Four regressions characterize the roundness vs. Feret's diameter (Eqs. 18-21 in Fig. 10) between 0.05
398 and 1 m. The increasing macro-roundness reflects the effects of clast crushing due to the collisional transport
399 and cataclastic sorting between the proximal and distal zones. We have highlighted a power regression for the
400 imbricated block clusters in the proximal zone with roundness >1 (Eq. 18 in Fig. 10). Two categories of
401 regressions are identified for the impacted and tilted block clusters in the distal zone with roundness between
402 0.9 and 1.08 (Eqs. 19-20 in Fig. 10). Three points of intersection ($a-c$ in Fig. 10) indicate similar values of
403 block roundness for cluster structures characterized by different regressions: between impacted and tilted
404 blocks in distal zone ($a = 1.05$, Eqs. 19-20); between distal clusters and the striated blocks from the ridges (b
405 ~ 1 , Eqs. 18-20) or proximal breccias with jigsaw features. We distinguish an inherited block shape for lava
406 blocks with roundness around ~ 0.9 and Feret's diameter = 0.05 m (c in Fig. 10), implying textural
407 relationships between these block clusters and sheared contact of the Pichu Pichu volcanic debris-avalanche
408 deposit.

409 The Riley's circularity of block clusters shows decreasing values from the proximal to distal zones (Table 5,
410 see Supplemental File 2) related to Feret's diameter, implying textural relationships between the block
411 clusters with the run-out distance.

412

413

414 6. Discussion

415

416 From field observations, we used complementary methods to describe surface and internal structures of the
417 Paipatja volcanic debris-avalanche deposits of the Tutupaca volcano and the associated pyroclastic density
418 currents. The quantitative sedimentary analysis contributes to correlate the block clusters, the block
419 avalanche lithofacies and mesoscale structures with different stages of cataclastic flow regime between the
420 DR-DAD and the associated pyroclastic density currents from proximal to distal zones. Quantitative

421 morphological and sedimentological parameters are correlated and compared to other avalanche deposits
 422 worldwide, showing that the brecciation have recorded the collisional interactions between lava dome sector
 423 collapse and pyroclastic density currents.

425 6.1. Classification of volcanic debris-avalanche deposits

426
 427 The volcanic debris avalanche deposits are commonly associated with PDC. The area and volume of the
 428 volcanic debris avalanche deposits associated with PDC are compared to Bezymianny eruptive sequence
 429 (Siebert et al., 1987) showing lava dome collapses with hydrothermally alteration interacted with the blast-
 430 generated the PDC (Fig. 2): Mount Saint Helens in the USA (Glicken, 1986), Bezymianni in Kamchatka
 431 (Siebert et al., 1987), Soufrière in Guadeloupe (Boudon et al., 1984). A relationship between the area (A) and
 432 volume (V) for the Tutupaca units is compared to the power regressions of other volcanic debris-avalanche
 433 deposits such as Mount Shasta and Mount Saint Helens in the USA (Fig. 2, Glicken, 1986; Siebert et al.,
 434 1987; Legros, 2002). The fault breccias have recorded the propagation of impact waves. The Tutupaca
 435 volcanic debris-avalanche deposits with H/L around $\sim 0.15-0.2$ ($12-13 \text{ km}^2$, $<1 \text{ km}^3$, $L = 6-8 \text{ km}$, Samaniego
 436 et al., 2015; Valderrama et al., 2016) show different units characterized by granular segregation and fingering
 437 instabilities (Figs. 3-4, Valderrama et al., 2018). A power regression (Eq. 2 in Fig. 2) characterizes the
 438 Tutupaca units compared to the proximal scar of the Mount Saint Helens deposits showing striations of the
 439 bedrock and the impacted distal zone in French Massif Central. This co-evolution of geomorphological
 440 parameters may be related to digitate shape of the avalanche deposits (Samaniego et al., 2015). The largest
 441 volcanic avalanche deposits (Mount Shasta, Legros, 2002) appears different from other volcanic debris-
 442 avalanche deposits in accordance with field observations, on ridge structures, striations, and block clusters.
 443 The geomorphological parameters of the largest avalanche units tend toward similar values (Eqs. 1-4 in Fig.
 444 2). We differentiate the intersecting point A (Fig. 2) with an area around ~ 140 and 180 km^2 and volume
 445 between 5 and 7 km^3 , implying a convergent evolution between the largest structural units with run-out
 446 distance of over 22 km (Mount Saint Helens in the USA and Parinacota in Chili, Fig. 2; Siebert and Roverato,
 447 2020) and the high velocity of volcanic debris avalanche associated with the blast lateral collapse and
 448 fluidization.

449 For the Tutupaca volcanic debris-avalanche deposits, the mean values of a/b ratio and ellipse, around ~ 1.7
 450 and ~ 3.5 respectively (Table 5) are between the Rio Chili, tilted block-rich debris-avalanche deposits in Peru
 451 and the lateral levee from the Mont Dore in French Massif Central (Bernard, 2015; Bernard et al., 2017). The
 452 mean ellipse/ a/b values around 1.88 characterize the crushing effects (Table 5, Bernard et al., 2019). We
 453 differentiate the thermal effect of fragmentation in proximal zone with ellipse/ a/b between 0.23 and 1.7 and
 454 the transfer of the plane collapse in the median zone showing ridge structures (ellipse/ $a/b = 2.04-2.78$). For
 455 the Tutupaca example, we have a dome collapse with a cataclastic gradient and a granular segregation during

456 a lateral spreading over ~1 km (Fig. 3). These statistical comparisons with other volcanic debris-avalanche
457 units contribute to establish a geomorphological classification of the volcanic debris-avalanche deposits
458 related to kinematic process. Secondary reworking of the Paipatja volcanic debris-avalanche deposits with
459 impact waves and fingering instabilities during flow propagation of the pyroclastic density current must be
460 considered. Successive collapses of the volcanic edifice contribute to the discontinuous units of the debris-
461 avalanche deposits.

462

463 6.2. Granular flow regime between the debris avalanche and pyroclastic density currents

464

465 Field observations show a reverse grading of the lithofacies assemblage (Socompa, van Wyk de Vries et al.,
466 2001; Davies et al., 2010): the HA-DAD is overlain by the DR-DAD interstratified with pyroclastic density
467 current deposits (Samaniego et al., 2015). A similar block-size distribution of the avalanche deposits and the
468 regressions (Eqs. 5-12 in Fig. 8) indicate a similar cataclastic origin with a co-genetic evolution of block
469 lithofacies linked with a sequential *syn*-cataclastic emplacement (Samaniego et al., 2015; Valderrama et al.,
470 2016).

471 The comparison of each block size-fractions with cumulative curves and histograms (Figs. 8-10) help to
472 identify the block lithofacies from proximal impact and cataclastic gradient with granular segregation in
473 flowing mass (Valderrama et al., 2016). Sedimentary parameters show a co-genetic brecciation of block
474 lithofacies (Eqs. 5-12, Fig. 8), which are compared to the impact breccia in French Massif Central. The lava
475 dome brecciations have recorded the propagation of impact waves. The roundness vs. Feret's diameter
476 suggests a co-genetic evolution between the proximal clusters, the abraded and striated blocks in the ridges
477 and the distal block clusters (Eqs. 19-22 in Fig. 10A) due to differentiated breakage during collisional
478 transport.

479

480 6.2.1. Cyclic impact waves and block clusters

481 The dome collapse with explosion is associated with a specific granular flow regime between avalanche and
482 pyroclastic density currents with secondary reworking. The succession of slide blocks is associated to frontal
483 propagation of cyclic impact wave in an extensional context during primary shear propagation generating a
484 clastic matrix (PDC, Mount Saint Helens, Glicken, 1986). Inherited jigsaw-fit textures have recorded the
485 initial dilation of the collapsed edifice (Mount Saint Helens, Glicken, 1986). The inherited shapes of the
486 block lithofacies ($a/b = 1.2-2$, ellipse = 0.2-2.5) indicate the reworking by impact waves. Imbricated block
487 clusters with jigsaw-fit texture and planar fractures are impacted under the collapse scar (A in Figs. 3A and
488 4A). Proximal imbricated block clusters may be generated during impact waves (Cox et al., 2019). Cyclic
489 impact waves and initial dilation contribute to block cluster growth with jigsaw-fit texture during the first
490 stage of avalanche emplacement. Clusters are disaggregated during shock propagation (Fig. 4A). The rock

491 fragmentation during the proximal impact wave increases the roundness (>1 , Fig. 10; Szabo et al., 2015). The
 492 propagation of the impact wave with granular oscillatory stress (Bernard and van Wyk de Vries, 2017; Cox et
 493 al., 2019) may contribute to produce the imbricated block clusters. Waves during cyclic impact may be
 494 considered to cause block cluster growth.

495 Blocks are split into clusters of smaller aggregates during transport (Palmer et al., 1991). Stick-slip
 496 oscillations (Sandnes et al., 2011) and an oscillatory relative speed may be considered during impact waves
 497 and dilation, which change the apparent coefficient of friction in the proximal zone. The isolated sub-rounded
 498 blocks and impacted blocks ($D \sim 1.64\text{-}2.83$ and ellipse/ $a/b = 1.7\text{-}1.8$, Tables 4 and 5) may be related to cluster
 499 disaggregation (Fig. 8B) during shock propagation generating the polymodal clast distributions with a thinner
 500 clastic matrix related to polymodal striations of the blocks from the ridges (ellipse/ $a/b = 1.7\text{-}1.8$, Eqs. 9-12,
 501 Fig. 8, Table 5). The cataclastic finer fractions increase the particle-to-particle interactions during flow
 502 propagation (Dennen et al., 2014) generating grooves and striations on the abraded surface of the impacted
 503 blocks. Textural relationships appear between proximal blocks and the striated blocks from the ridges (Table
 504 5) with decreasing values of Riley's circularity.

505 506 6.2.2. *An upper collisional regime*

507 Differentiated velocities related to transitional regime must be considered between the matrix-rich facies and
 508 the block facies ($v_1 < v_2$; Glicken, 1998; Caballero and Capra, 2011). Formation of the elongated ridges is
 509 attributed to granular segregation and differential block velocities in the flowing mass (Dufresne and Davies,
 510 2009). The bimodal clast distributions in the medial zone (ellipse/ $a/b \sim 1.7$) differentiate the transverse
 511 blocks, the elongated ridges and lateral levee with sigmoidal jigsaw-breccias (Fig. 6B-D). The DR-DAD
 512 lithofacies contribute to decreasing run-out velocity with localized secondary flow (Socompa, Kelfoun et al.,
 513 2008; Mont Dore in French Massif Central, Bernard and van Wyk de Vries, 2017) and segregation waves to
 514 the flow front (Gray, 2013).

515 A multidirectional switch of mass spreading may be considered, with segregation waves to the flow front
 516 (Glicken, 1998). Transverse orientations of blocks in the medial zone implicate a quick stop attributed to a
 517 compressive context. The lack of propagation of the proximal conditions contribute to plug flow and granular
 518 segregation, generating lateral levees and ridges in the upper collisional flow regime for the median zone
 519 (Shea and van Wyk de Vries, 2008; Valderrama et al., 2016). Along lateral levee, rafted blocks with sigmoidal
 520 jigsaw-breccias are related to transport by traction in shearing context, generating secondary fractures.

521 We differentiate the parent dome volcanic processes from the breakage due to collisional transport, which
 522 increases the roundness from 1 to 1.7, related to the frontal reworking by impact wave (Table 5). An upper
 523 collisional regime for block lithofacies generating impact marks is differentiated from basal frictional regime
 524 with striations (e.g. Parinacota and Ollagüe in Chile, Clavero et al., 2002, Clavero et al., 2004; El Zagan,
 525 Mexico, Caballero and Capra, 2011). Collisional abrasion may be associated with the dispersive pressure

526 generated by the subsequent pyroclastic density current. Shock and brecciation of blocks limit the mixture of
 527 lithofacies (*e.g.* Pichu Pichu in Peru, [Legros et al., 2000](#); El Zagan, Mexico, [Caballero and Capra, 2011](#)).
 528 Stick-slip motion at the front of lobe and high-speed of blocks may also be considered ([Bartali et al., 2015](#)).
 529 Each of the block avalanche deposits and striations present a specific regression for the roundness *vs.* Feret's
 530 diameter diagram (Eqs. 13-17 with $R^2 > 0.5$ in [Fig. 9](#)), implying a differentiated evolution of the breakage
 531 during collisional transport and granular segregation. Inherited clast shapes with roundness between 0.9 and
 532 1.2 are related to a same cataclastic origin. The impact of clasts onto block surfaces ($r = 0.5a^2/h$, [Clavero et](#)
 533 [al., 2002](#)) can be approximated with $a < 5$ cm radius of hemispherical damage zone, and $h \sim 1-5$ cm distance
 534 that penetrated into the block. Calculated r values between 2.5 and 12.5 cm is in accordance with the
 535 surrounded clasts. The impact force F has a value of about 15.7×10^{10} N by using $F = \Pi a^2 \rho_0$ with a typical
 536 ρ_0 value around $\sim 2.10^9$ Pa ([Clavero et al., 2002](#)). The clast velocity for making impact marks can be
 537 estimated around ~ 8.86 m.s⁻¹ by using $V = (0.5 \Pi \rho_0 / Mr)^{1/2} a^2$ with $M \sim 10^3$ kg, $a < 5$ cm and r values between
 538 2.5 and 12.5 cm ([Clavero et al., 2002](#)), in accordance with impact marks analysis on clast faces of Panum
 539 block lithofacies (Mono Craters, CA, [Dennen et al., 2014](#)). The avalanche velocity in the middle zone
 540 (around ~ 3 and 6 km from source, [Clavero et al., 2002](#)) is considered between 15.5 and 39.6 m.s⁻¹ by using v
 541 $= (2gH)^{1/2}$. Localized striations and grooves can be attributed to the peak velocity at the flow front. The
 542 inherited shapes of the lava blocks and the co-genetic evolution between the blocks from the ridges and
 543 striations may be associated to secondary fracturing with partial decompression during run-out propagation
 544 ([Bernard et al., 2019](#)).
 545 The dome collapse is associated with a specific granular flow regime between avalanche and pyroclastic
 546 density currents: cyclic impact waves with disaggregation during shock propagation, and secondary flow
 547 with segregation waves. Basal frictional regime with striations is differentiated from higher collisional and
 548 cataclastic flow regime generating clast breakage and impact marks (*e.g.* Parinacota and Ollagüe in Chile,
 549 [Clavero et al., 2002](#), [Clavero et al., 2004](#); El Zagan, Mexico, [Caballero and Capra, 2011](#)).

550

551 6.3. The frontal reworking

552

553 Logarithmic regressions of the abraded and sub-rounded block lithofacies in the median and distal zones (d
 554 $\sim 1.64-1.83$; ellipse/ $a/b \sim 2.7$, Eqs. 7-11 in [Fig. 8A](#)) are close to those of the impact breccias along avalanche
 555 fault zone in French Massif Central (Eq. 12 in [Fig. 8A](#), [Bernard and van Wyk de Vries, 2017](#)). The Riley's
 556 circularity ([Table 5](#), see [Supplemental File 2](#)) shows that the polyhedral blocks with conchoidal fractures and
 557 striations of the ridge structures differentiated from sub-rounded blocks in the distal zone. These may be
 558 associated to an oriented abrasion and thermal shock generating tilted blocks with cracked surface. The clast
 559 breakage with striations due to collisional transport decreases the Riley's circularity ([Table 5](#)). These block
 560 lithofacies may be associated to crushing impact with frictional temperature during oscillatory stress

561 (Bernard and van Wyk de Vries, 2017) related to decompression in rotational shearing, and matrix
562 segregation.

563 The inherited shapes of the blocks ($a/b = 1.2-2$; ellipse = 0.2-2.5; Riley's circularity ~ 0.6 in Table 5; Eq. 14
564 and $a \sim 0.9$ in Fig. 9) implied the reworking by impact wave (Cox et al., 2019) and similar processes of
565 abrasion between the imbricated block clusters in the proximal zone, the striated blocks from ridges and the
566 tilted distal blocks. These are close to those of the sheared lava breccias observed along the Pichu Pichu
567 debris-avalanche deposit. Flow traction may contribute to block piles (Cox et al., 2019) up to a point where
568 flows are not competent. Fractal D -values of the surrounded matrix between 0.6 and 2.8 are associated to an
569 extensional disaggregation and granular transport (Table 4, Blekinsop and Fernandes, 2000). A *syn*-
570 cataclastic emplacement of the blocks with a co-genetic evolution is differentiated between the proximal and
571 median zones and between the striated blocks from ridges and the distal, impacted blocks.

572

573 7. Conclusions

574

575 Field observations together with quantitative sedimentological analyses help to characterize textural
576 variations of the Paipatja avalanche deposits and the associated pyroclastic density current deposits from
577 Tutupaca volcano in southern Peru. A typical lithofacies assemblage with a reverse grading shows jigsaw
578 breccias, impacted block clusters and striations associated with the interaction between the debris avalanche
579 and the subsequent pyroclastic density currents.

580 Cyclic impact waves and initial dilation of the Tutupaca lava dome have contributed to produce jigsaw
581 breccias and imbricated block clusters during the first stage of avalanche emplacement. Cluster
582 disaggregation during shock propagation contribute to an upper collisional regime, generating isolated blocks
583 with striations. Transverse blocks, lateral levee and ridges are associated to a switch of mass spreading with
584 granular segregation. The frontal reworking by impact wave with extensional disaggregation contributes to
585 generate impacted block clusters in distal zone. From the statistical dataset, a few regressions have been
586 established indicating the same cataclastic origin with a co-genetic evolution of block lithofacies.

587 Sequential events of *syn*-emplacement processes during impact waves have been established related to
588 volcanic debris-avalanche units and pyroclastic density current deposits. These observations help to constrain
589 the collisional shearing contact between avalanche units and associated pyroclastic density currents, and help
590 to explain the block cluster growth and the block disaggregation correlated to sequential *syn*-emplacement
591 processes of debris avalanche units with associated pyroclastic deposits.

592 The deposits at Tutupaca are exceptional for their freshness and clarity, and lack of disturbance. This area is
593 an important record of lava dome collapse and debris avalanche and pyroclastic flow interaction.

594

595 Acknowledgments

596 The fieldwork in Peru trip has been funded by the “Institut de la Recherche pour le Développement” support
 597 (O. Roche and P. Samaniego, IRD) for Tutupaca volcano. The geoheritage context is provided through the
 598 UNESCO International Geosciences Program project 692, Geoheritage for Resilience.

599

600 **References**

601

602 Andrade, S.D., van Wyk de Vries, B., 2010. Structural analysis of the early stages of catastrophic strato-
 603 volcano flank-collapse using analogue models. *Bull. Volcanol.* 72, 771-789.

604 Bartali, R., Sarocchi, D., Nahmad-Molinari, Y., 2015. Stick-slip motion and high speed ejecta in
 605 granular avalanches detected through a multi-sensors flume. *Eng. Geol.* 195, 248-257.

606 Bernard, K., 2015. Quelques aspects sédimentaires des avalanches de débris volcaniques. Ph.D.

607 Thesis, Univ. Clermont-Auvergne, France (Unpub., in French). Available at: <NNT : _____
 608 [2015CLF22624](#)>.<tel-01330779>.

609 Bernard, K., van Wyk de Vries, B., 2017. Volcanic avalanche fault zone with pseudotachylite and gouge
 610 in French Massif Central. *J. Volcanol. Geotherm. Res.* 347, 112-135.

611 Bernard, K., Thouret, J-C., van Wyk de Vries, B., 2017. Emplacement and transformations of volcanic debris
 612 avalanches - A case study at El Misti volcano, Peru. *J. Volcanol. Geotherm. Res.* 340, 68-91.

613 Bernard, K., van Wyk de Vries, B., Thouret, J-C., 2019. Fault textures in volcanic debris-avalanche
 614 deposits and transformations into lahars: The Pichu Pichu thrust lobes in south Peru compared to
 615 worldwide avalanche deposits. *J. Volcanol. Geotherm. Res.* 371, 116-136.

616 Blekinsop, T.G., Fernandes, T.R.C., 2000. Fractal characterization of particle size distributions in
 617 chromitites from the Great Dyke, Zimbabwe. *Pure Appl. Geophys.* 157, 505-521.

618 Blott, S.J., Pye, K., 2008. Particle shape: a review and new methods of characterization and classification.
 619 *Sedimentology* 55, 31–63.

620 Boudon, G., Semet, M.P., Vincent, P.M., 1984. Flank-failure-directed blast eruption at Soufrière,
 621 Guadeloupe, French West Indies: A 3000-yr-old Mt. St. Helens? *Geology* 12, 350-353.

622 Caballero, L., Capra, L., 2011. Textural analysis of particles from El Zaguán debris avalanche deposit,
 623 Nevado de Toluca volcano, Mexico: Evidence of flow behavior during emplacement. *J. Volcanol.*
 624 *Geotherm. Res.* 200, 75-82.

625 Clavero, J.E., Sparks, R.S.J., Huppert, H.E., 2002. Geological constraints on the emplacement mechanism
 626 of the Parinacota avalanche, northern Chile. *Bull. Volcanol.* 64, 40–54.

627 Clavero, J.E., Polanco, E., Godoy, E., Aguilar, G., Sparks, R.S.J., van Wyk de Vries, B., Perez de Arce, C.,
 628 Matthews, S., 2004. Substrata influence in the transport and emplacement mechanism of the Ollagüe
 629 debris avalanche (northern Chile). *Acta Vulc.* 16, 59–76.

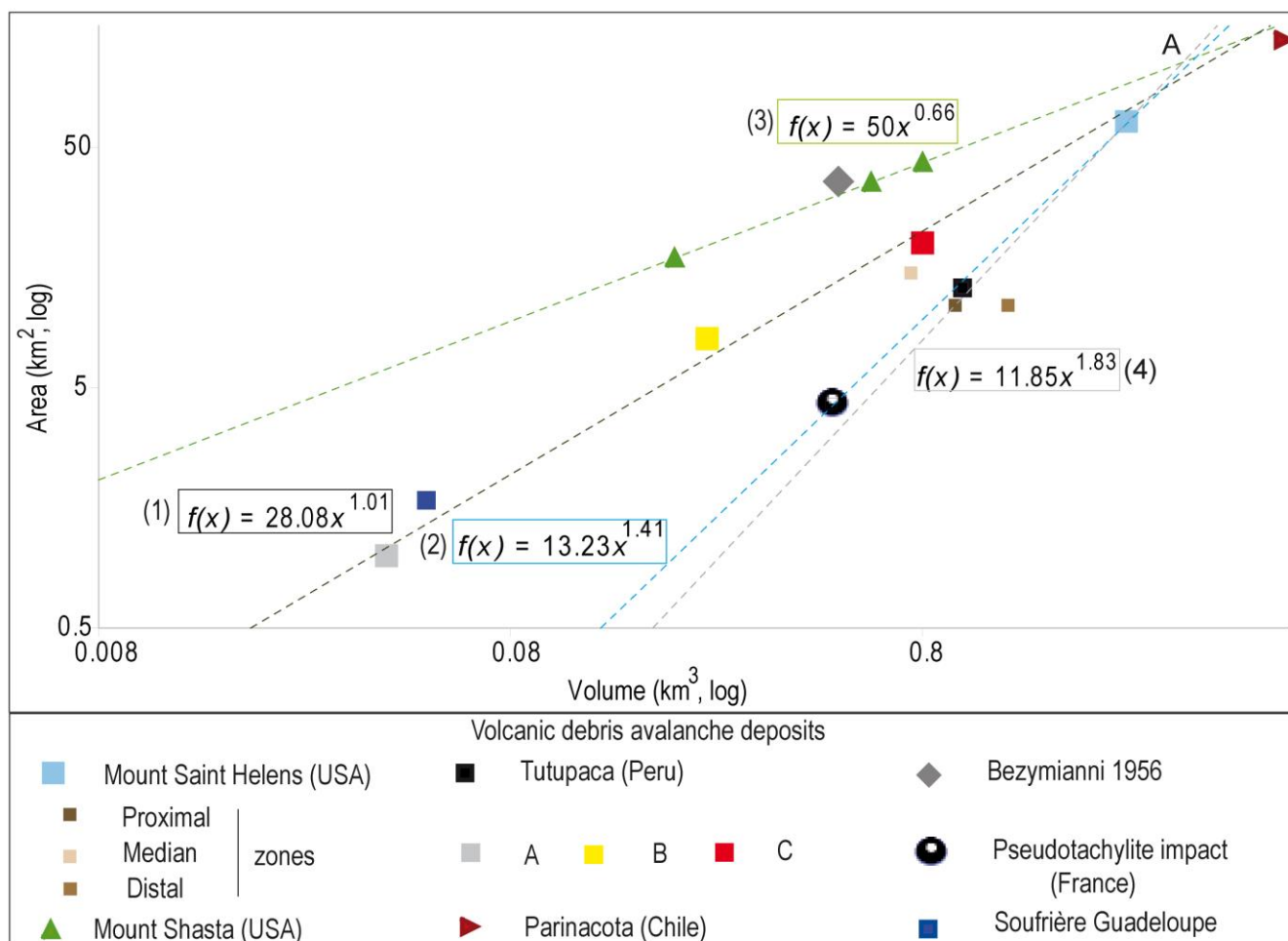
630 Cox, R., O'Boyle, L., Cytrynbaum, J., 2019. Imbricated coastal boulder deposits are formed by storm

- 631 waves, and can preserve a long-term storminess record. *Sci. Rep.* 9, 10784.
- 632 Crandell, D.R., Miller, C.D., Glicken, H.X., Christiansen, R.L., Newhall, C.G., 1984. Catastrophic debris
633 avalanche from ancestral Mount Shasta volcano, California. *Geology* 12, 143-146.
- 634 Crawford, E., Mortensen, K., 2009. An Image J plugin for the rapid morphological characterization of
635 separated particle sand an initial application to placergold analysis. *Comput. Geosci.* 35, 347–359.
- 636 Davies, T.R., McSaveney, M.M., Kelfoun, K., 2010. Runout of the Socompa volcanic debris avalanche,
637 Chile: a mechanical explanation for low basal shear resistance. *Bull. Volcanol.* 72, 933-944.
- 638 Dennen, R.L., Bursik, M.I., Roche, O., 2014. Dome collapse mechanisms and block-and-ash flow
639 emplacement dynamics inferred from deposit and impact mark analysis, Mono Craters, CA.
640 *J. Volcanol. Geotherm. Res.* 276, 1-9.
- 641 Dufresne, A., Davies, T., 2009. Longitudinal ridges in mass movement deposits. *Geomorphology* 105, 171-
642 181. DOI:10.1016/j.geomorph.2008.09.009.
- 643 Glicken, H., 1986. Rockslide-debris avalanche of May 18, 1980, Mount Saint Helens Volcano,
644 Washington. Ph.D. Thesis, Univ. Calif. Santa Barbara, p. 303.
- 645 Glicken, H., 1998. Rockslide-debris avalanche of May 18, 1980, Mount St. Helens Volcano, Washington
646 *Bull. Geol. Surv. Jpn.* 49, 55-106.
- 647 Gray, J.M.N.T., 2013. A hierarchy of particle-size segregation models: from polydisperse mixture
648 to depth-averaged theories. *AIP Conf. Proc.*, 1542, 66-73.
- 649 Guilbaud, M-N., Chedeville, C., Molina-Guadarrama, A-N., Siebe, C., 2022. Volcano-sedimentary
650 processes at Las Derrumbadas rhyolitic twin domes, Serdan-Oriental Basin, Eastern Trans-
651 mexican Volcanic Belt. *Geol. Soc. Spec. Publ.*, 520, 31.
- 652 Janoo, V., 1998. Quantification of Shape, Angularity, and Surface Texture of Base Course Materials.
653 U.S. Army Corps of Engineers, Cold Regions Research & Engineering Laboratory, Hanover NH,
654 pp. 1-22 (Special Report).
- 655 Kelfoun, K., Druitt, T., van Wyk de Vries, B., Guilbaud, M-N., 2008. Topographic reflection of the
656 Socompa debris avalanche, Chile. *Bull. Volcanol.* 70, 1169-1187.
- 657 Launeau, P., Robin, Y.F., 2005. Determination of fabric and strain ellipsoids from measured sectional
658 ellipses - Implementation and applications. *J. Struct. Geol.* 27, 2223-2233.
- 659 Legros, J.F., Cantagrel, J.M., Devouard, B., 2000. Pseudotachylite (Frictionite) at the base of
660 the Arequipa Volcanic landslide (Peru): Implications for emplacement mechanisms. *J.*
661 *Geol.* 108, 601-611.
- 662 Legros, J.F., 2002. The mobility of long-runout landslides. *Eng. Geol.* 63, 301–331.
- 663 Mariño, J., Samaniego, P., Manrique, N., Valderrama, P., Roche, O., van Wyk de Vries, B., Guillou, H.,
664 Zerathe, S., Arias, C., Liorzou, C., 2021. The Tutupaca volcanic complex (Southern Peru):
665 Eruptive chronology and successive destabilization of a dacitic dome complex. *J. S. Am. Earth*

- 666 Sci., 109, 103-227.
- 667 Mehl, K.W., Schmincke, H.U., 1999. Structure and emplacement of the Pliocene Roque Nublo
668 debris avalanche deposit, Gran Canaria, Spain. *J. Volcanol. Geotherm. Res.* 94, 105-134.
- 669 Naranjo, J.A., Francis, P., 1987. High velocity debris avalanche at Lastaria volcano in the north Chilean
670 Andes. *Bull. Volcanol.* 49, 509-514.
- 671 Palmer, B.A., Alloway, B.V., Neall, V.E., 1991. Volcanic-debris avalanche deposits in New Zealand:
672 lithofacies organization in unconfined, wet-avalanche flows. In: Fisher, R.V., Smith G.A.;
673 (Eds.), *Sedimentation in volcanic setting*. SEPM Spec. Pub. vol. 45, pp. 89-98.
- 674 Samaniego, P., Valderrama, P., Mariño, J., van Wyk de Vries, B., Roche, O., Manrique, N., Chedeville, C.,
675 Fidel, L., Malnati, J., 2015. The historical (218 ± 14 aAP) explosive eruption of Tutupaca volcano
676 (Southern Peru). *Bull. Volcanol.* 77, 51.
- 677 Sandnes, B., Flekkoy, E.G., Knudsen, H.A., Maloy, K.J., See, H., 2011. Patterns and flow in frictional fluid
678 dynamic. *Nat. Commun.* 2, 288.
- 679 Shea, T., van Wyk de Vries, B., 2008. Structural analysis and analogue modeling of the kinematics and
680 dynamics of rockslide avalanches. *Geosphere* 4, 657–686.
- 681 Siebe, C., Komorowski, J-C., Sheridan, M-F., 1992. Morphology and emplacement collapse of an
682 unusual debris avalanche deposit at Jocotitlán Volcano, Central Mexico. *Bull. Volcanol.* 54, 573-589.
- 683 Siebert, L., Roverato, M., 2020. A Historical Perspective on Lateral Collapse and Volcanic Debris
684 Avalanche. In: Roverato, M., Dufresne, A., Procter, J., (Eds.), *Volcanic Debris Avalanches from
685 Collapse to Hazards*. Springer, pp. 11-50.
- 686 Siebert, L., Glicken, H., Ui, T., 1987. Volcanic hazards from Bezymianny- and Bandai-type eruptions. *Bull.*
687 *Volcanol.* 49, 435-459.
- 688 Suzuki-Kamata, K., Kusano, T., Yamasaki, K., 2009. Fractal analysis of the fracture strength of lava
689 dome material based on the grain size distribution of block-and-ash flow deposits at Unze
690 volcano, Japan. *Sedim. Geol.* 220, 162-168.
- 691 Szabo, I., Domokos, G., Grotzinger, J.P., Douglas, J.J., 2015. Reconstructing the transport history of
692 pebbles on Mars. *Nat. Commun.* 6: 8366.
- 693 Valderrama, P., 2016. Origin and dynamics of volcanic debris avalanches: surface structure analysis
694 of Tutupaca volcano (Peru). *Earth Sciences. Univ. Blaise Pascal-Clermont-Ferrand II*.
- 695 Valderrama, P., Roche, O., Samaniego, P., van Wyk de Vries, B., Bernard, K., Marino J., 2016. Dynamic
696 implications of ridges on a debris avalanche deposit at Tutupaca volcano (southern Peru). *Bull.*
697 *Volcanol.* 78, 14.
- 698 Valderrama, P., Roche, O., Samaniego, P., Van Wyk de Vries, B., Araujo, G., 2018. Granular fingering as
699 a mechanism for ridge formation in debris avalanche deposits: laboratory experiments and
700 implications for Tutupaca volcano, Peru. *J. Volcanol. Geotherm. Res.* 349, 409-418.

- 701 Van Wyk de Vries, B., Self, S., Francis, P.W., Keszthelyi, L., 2001. A gravitational spreading origin for the
702 Socompa debris avalanche. *J. Volcanol. Geotherm. Res.* 105, 225-247.
- 703 Voight, B., Glicken, H., Janda, R.J., Douglass, P.M., 1981. Catastrophic rockslide-avalanche of May 18.
704 In: Lipman, P. W., Mullineaux, D.R. (Eds.), *The 1980 eruptions of Mount St. Helens, Washington.*
705 *U.S. Geol. Surv. Prof. Pap.* vol. 1250, pp. 347-371.
- 706 Zernack, A., Procter, J., Cronin S., 2009. Sedimentary signatures of cyclic growth and destruction of
707 stratovolcanoes: a case study from Mt Taranaki, New Zealand. *Sediment. Geol.* 220, 288-305.

712



713

714 **Fig. 2.** Area (km²) vs. volume (km³) of volcanic debris avalanche deposits on double log graph: Mount
 715 Shasta and Mount Saint Helens in the USA (Glicken, 1986; Siebert et al., 1987); Bezymianni in Kamchatka
 716 (Siebert et al., 1987); Parinacota in Chile (Clavero et al., 2002; Legros, 2002); Tutupaca in Peru (Samaniego
 717 et al., 2015; Valderrama et al., 2016); Soufrière in Guadeloupe (Boudon et al., 1984) and Mont Dore in
 718 French Massif Central (Bernard and van Wyk de Vries, 2017). A. The proximal zone; B. The ridged unit; C.
 719 The distal zone.

720

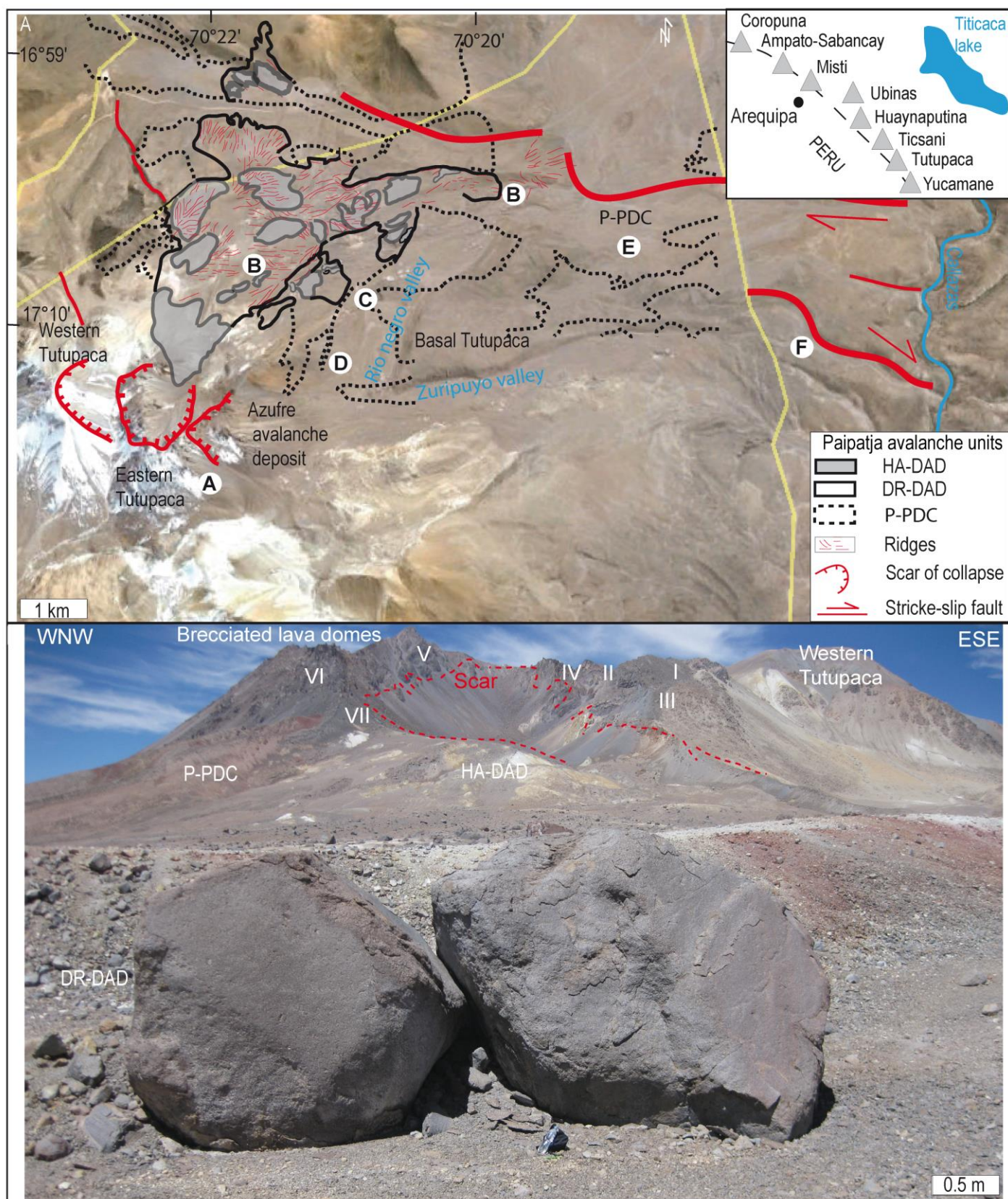


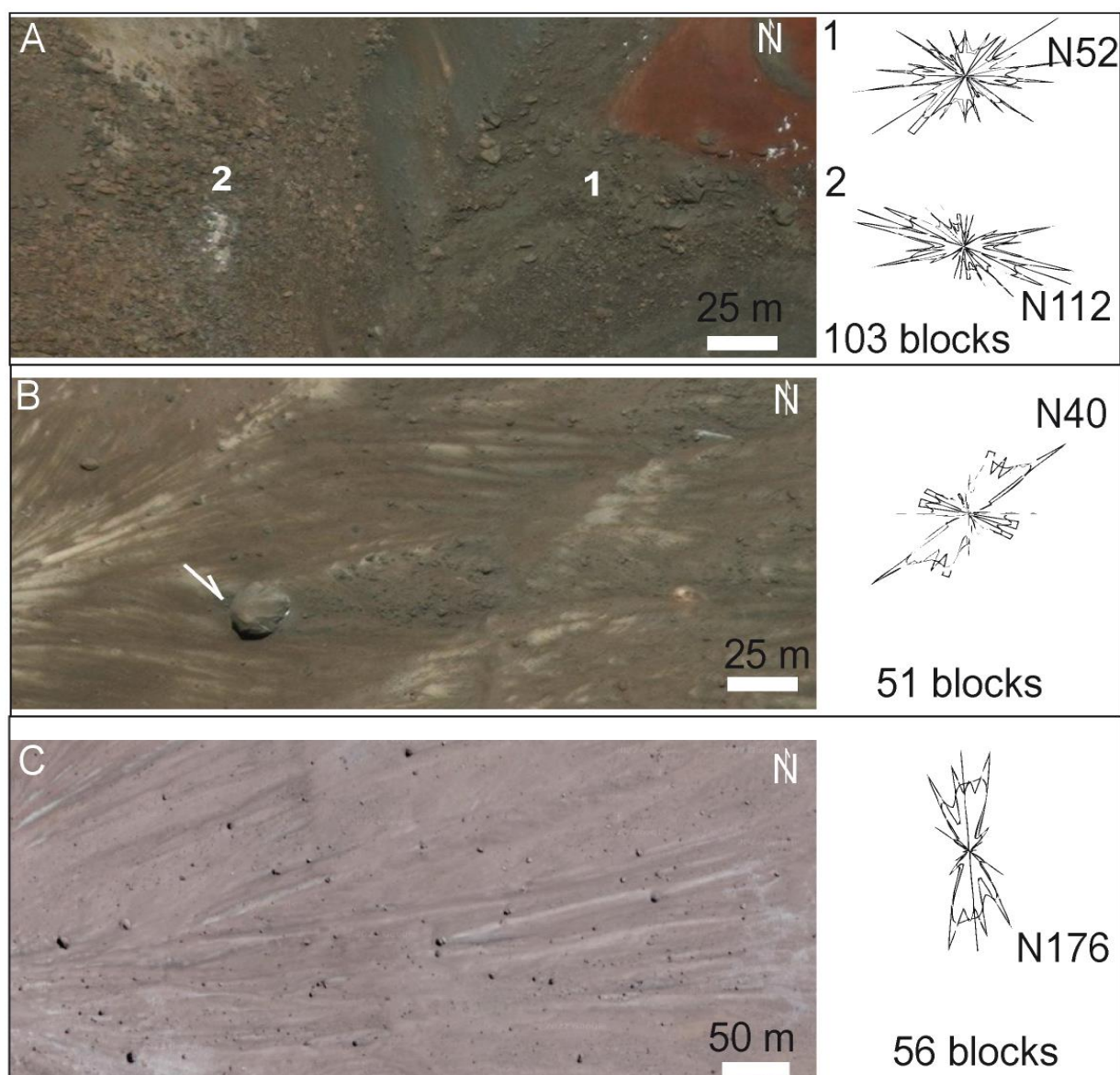
Fig. 3. Geological setting of the Paipatja avalanche deposits exposed in the northeastern part of Tutupaca volcanic complex (Southern Peru, modified from Samaniego et al., 2015; Valderrama et al., 2016). A. Landforms of the avalanche deposits and structures at the North East of the brecciated lava domes from Google Earth with stratigraphic sections. We differentiate the hydrothermal rich avalanche deposit (HA-

727 DAD, $L = 6-8$ km, $V < 1$ km³; $H/L = 0.23-0.17$, [Samaniego et al., 2015](#)); a dome rich debris-avalanche deposit
728 (DR-DAD); the Paipatja pyroclastic density current deposits (P-PDC, $\sim 218 \pm 14$ aBP). The right-top inset
729 shows the location of Pleistocene volcanoes in the Andean Central Volcanic Zone. The white points indicate
730 the outcrop locations of the clusters and the block lithofacies. A. Under the erosional amphitheater of collapse
731 scar in proximal zone; B. Transverse alignment of blocks and ridge structures; C. Extensional fault zone with
732 abrasion and jigsaw-fractured lithofacies; D. Shear zone along lateral levee; E. Impact and lava bombs; F.
733 Buried blocks and abrasion. B. Panoramic view of the northeast of Tutupaca volcano, showing the horseshoe-
734 shape amphitheater and lava domes (I to VI) and DR-DAD with transverse alignment of blocks. Most of the
735 domes are constructed on the older hydrothermally altered basal edifice ([Samaniego et al., 2015](#); [Valderrama](#)
736 [et al., 2016](#)).

737

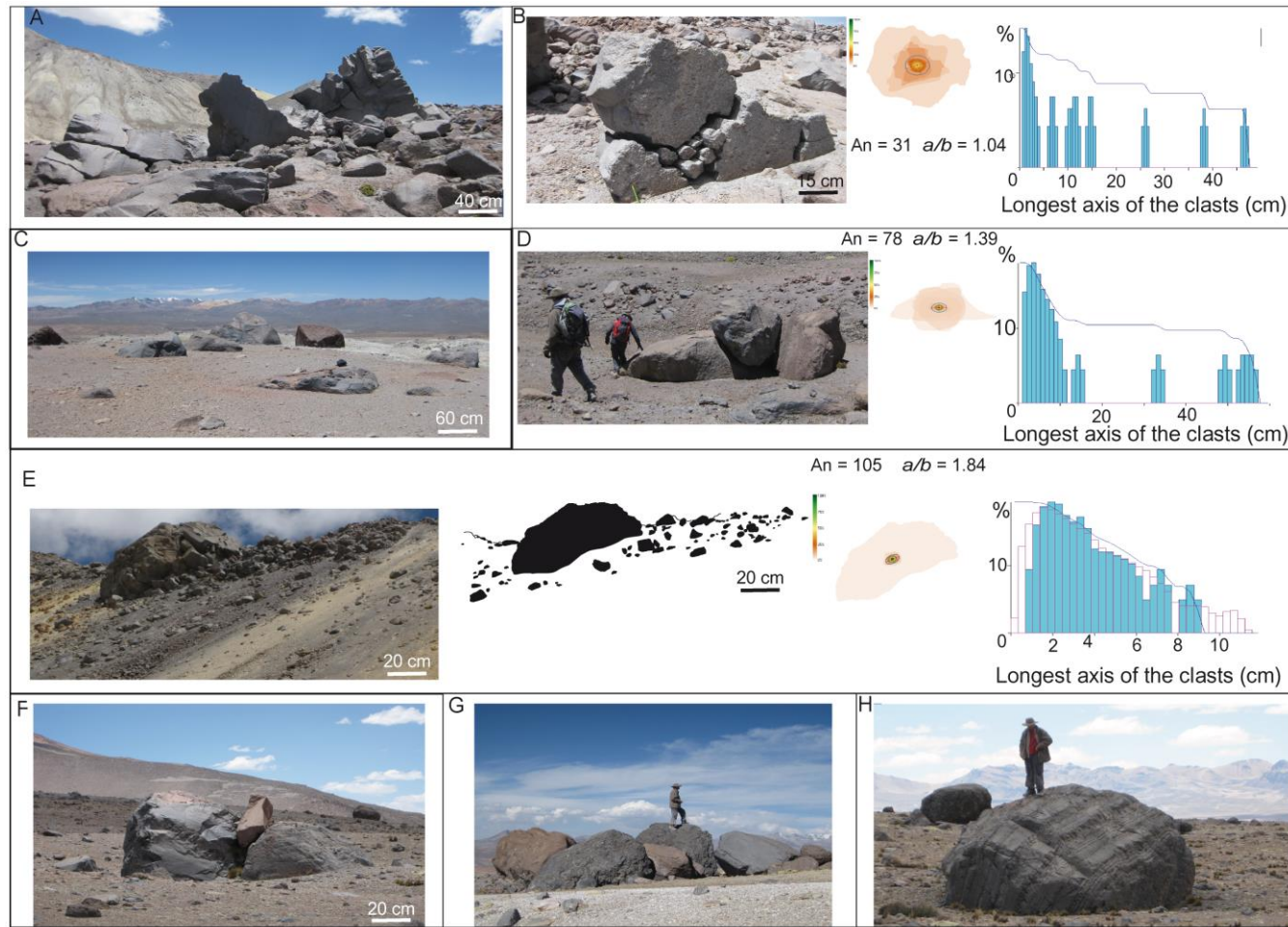
738

739



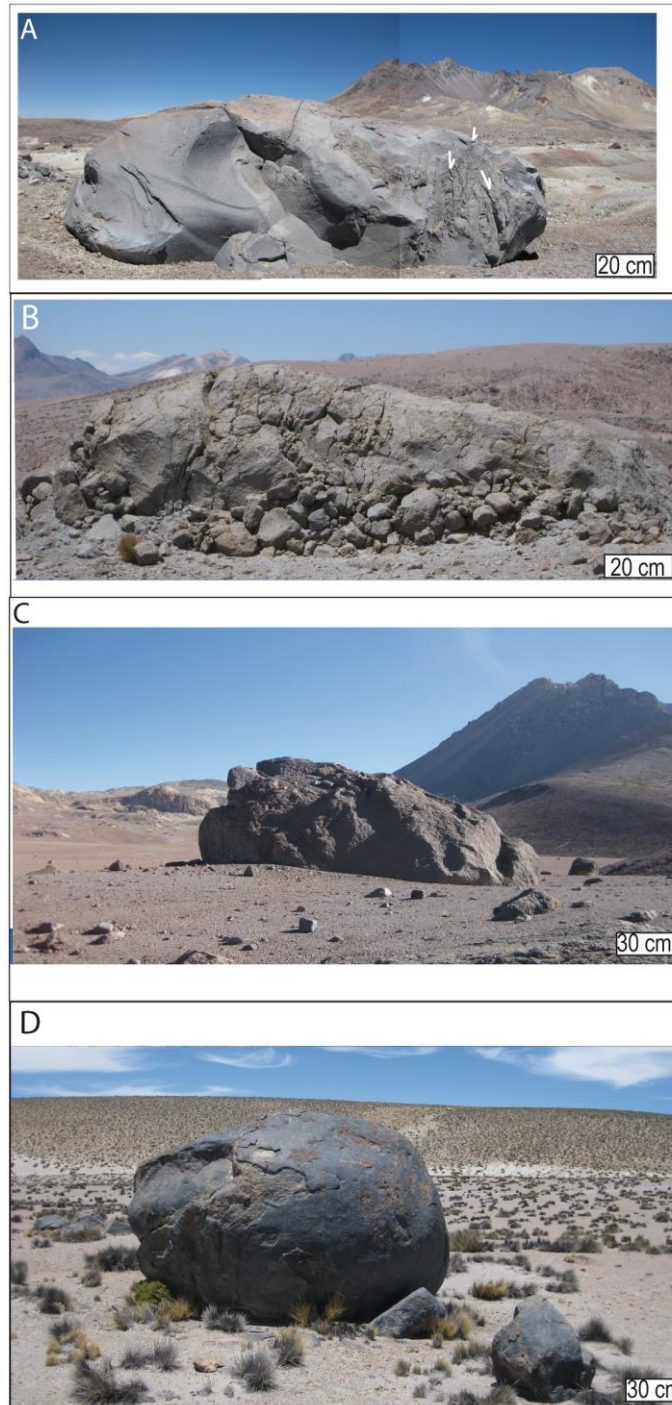
740

741 **Fig. 4.** The syn-emplacment block lithofacies and block orientations (SPO, [Launeau and Robin, 2005](#)) from
 742 proximal to distal zones using georeferenced Google Earth imagery. A. Proximal brecciated zones under the
 743 scar between domes V to VII: 1. An impacted and crushed zone showing imbricated block clusters without
 744 preferential orientation; 2. A tilted zone with N112E angular dome fragments adjacent to the PDC in red; B.
 745 Isolated polyhedral block (white arrow) of ridge structures in the median zone showing in downstream N40E
 746 disaggregated clasts; C. The transverse and isolated blocks (>1 m in length, N176E) surrounded by P-PDC
 747 unit in distal zone.



748

749 **Fig. 5.** Block clusters of DR-DAD from SPO analysis (Launeau and Robin, 2005). A. Vertical impact of blocks with abraded surface and undulated fractured
 750 borders under the erosional amphitheater of collapse scar; B. Impacted jigsaw-clusters with polymodal clast distribution; C. Subdued blocks in transverse
 751 ridges; D. Impacted blocks in distal zone with polymodal distribution of the clasts; E. Block along lateral levee with sigmoidal jigsaw-breccias showing a
 752 bimodal clast distribution; F. Angular and impacted block between aligned and subdued blocks; G. Block cluster in distal zone; H. Subdued and tilted blocks.



753

754

755

756

757

758

759

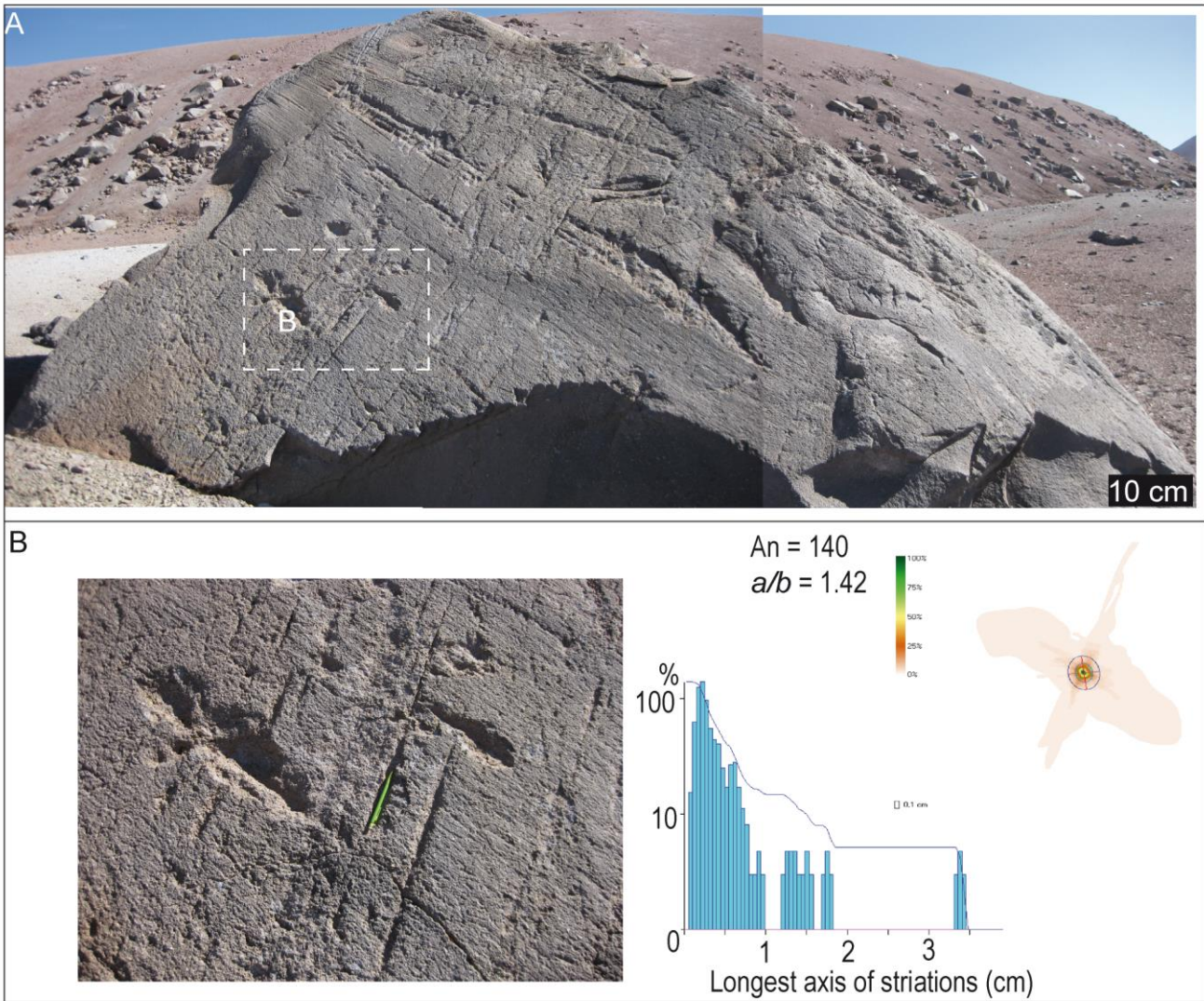
760

761

762

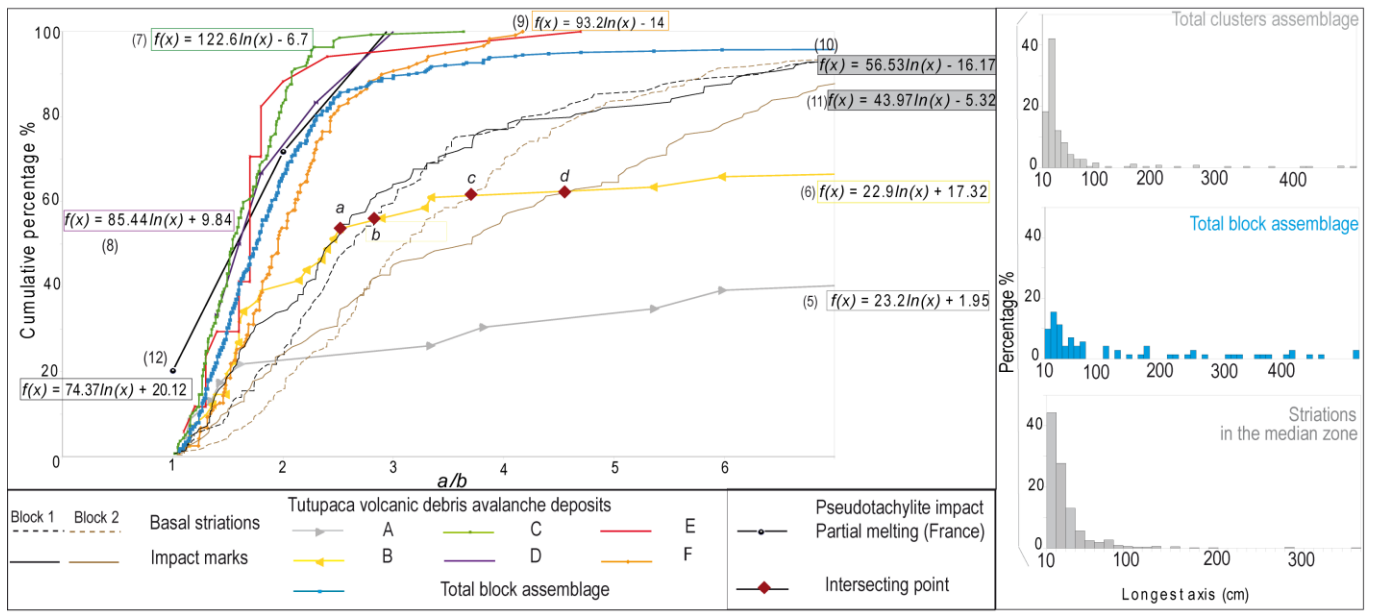
Fig. 6. Textural gradient of block lithofacies of the Paipatja avalanche deposits. A. Transverse blocks with an oriented abrasion: *white arrows* show striations on upstream sub-rounded faces and planar faces with conchoidal fractures in downstream; B. Large polyhedral block (~3 m high and ~5 m length) with an oriented abrasion, quenched and cracked surface in upper part and sub-rounded lava in altered vitreous phase in lower part; C. Transversal alignment of abraded blocks with bimodal clast distribution from SPO analysis (Launeau and Robin, 2005) related to pyroclastic density current deposits; D. Polymodal clast distribution (SPO analysis, Launeau and Robin, 2005) of pyroclastic density current deposits around a distal sub-rounded block.

763
764
765
766



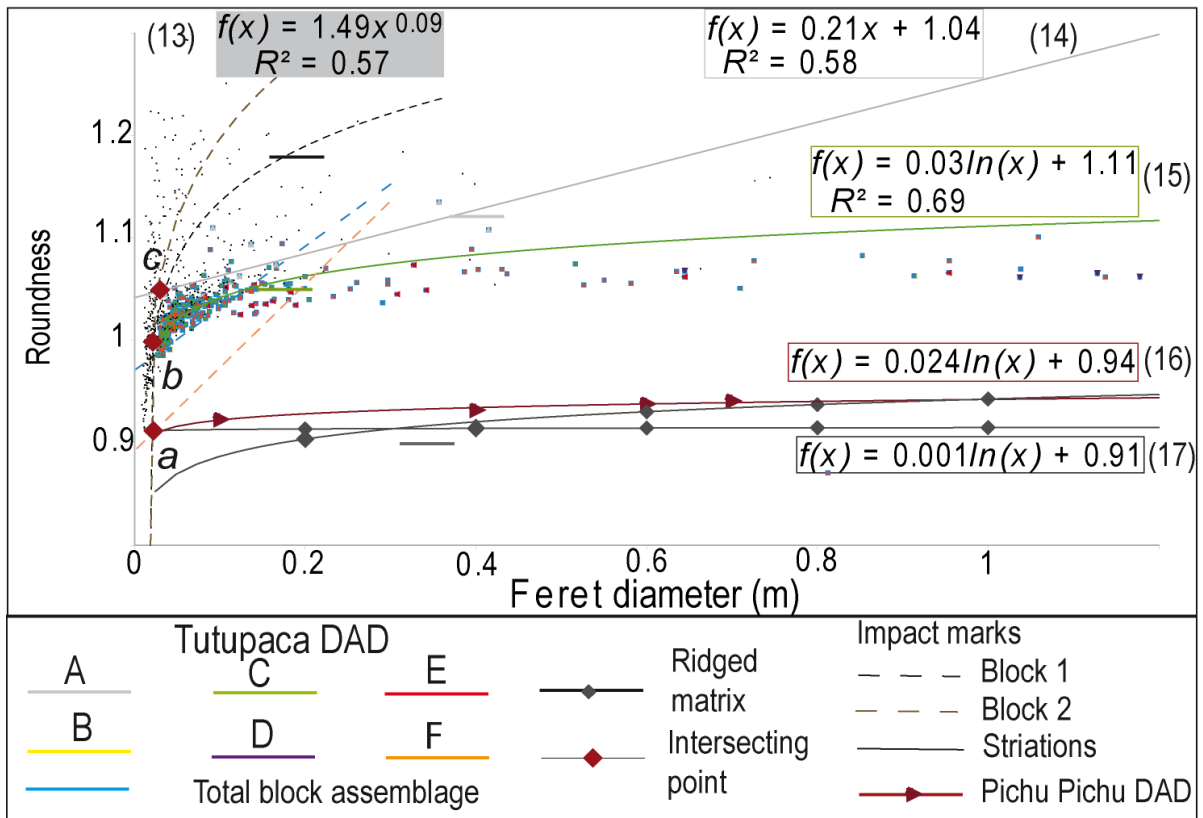
767
768 **Fig. 7.** Striations and grooves of ridged blocks from SPO analysis (635 striations, [Launeau and Robin,](#)
769 [2005](#)). A. Subdued block (~2 m high and 1.6 m length) with abraded planar surfaces, grooves and
770 striations with circular depressions (~1-5 cm depth, ~2-3 mm wide); B. Detailed analysis of grooves and
771 striations showing polymodal distribution related to the P-PDC interactions ($An = 140$ striations, $a/b =$
772 1.42).

773
774
775
776
777
778
779
780
781



782
 783
 784
 785
 786
 787
 788
 789
 790
 791
 792
 793
 794
 795
 796
 797
 798
 799
 800
 801
 802
 803
 804

Fig. 8. Sedimentological analysis of block lithofacies of the Paipatja avalanche deposits from proximal to distal zones. A. Cumulative curves of block lithofacies vs. a/b from SPO analysis (404 blocks, 635 striations and impact marks; [Launeau and Robin, 2005](#)); B. Histograms.



805

806

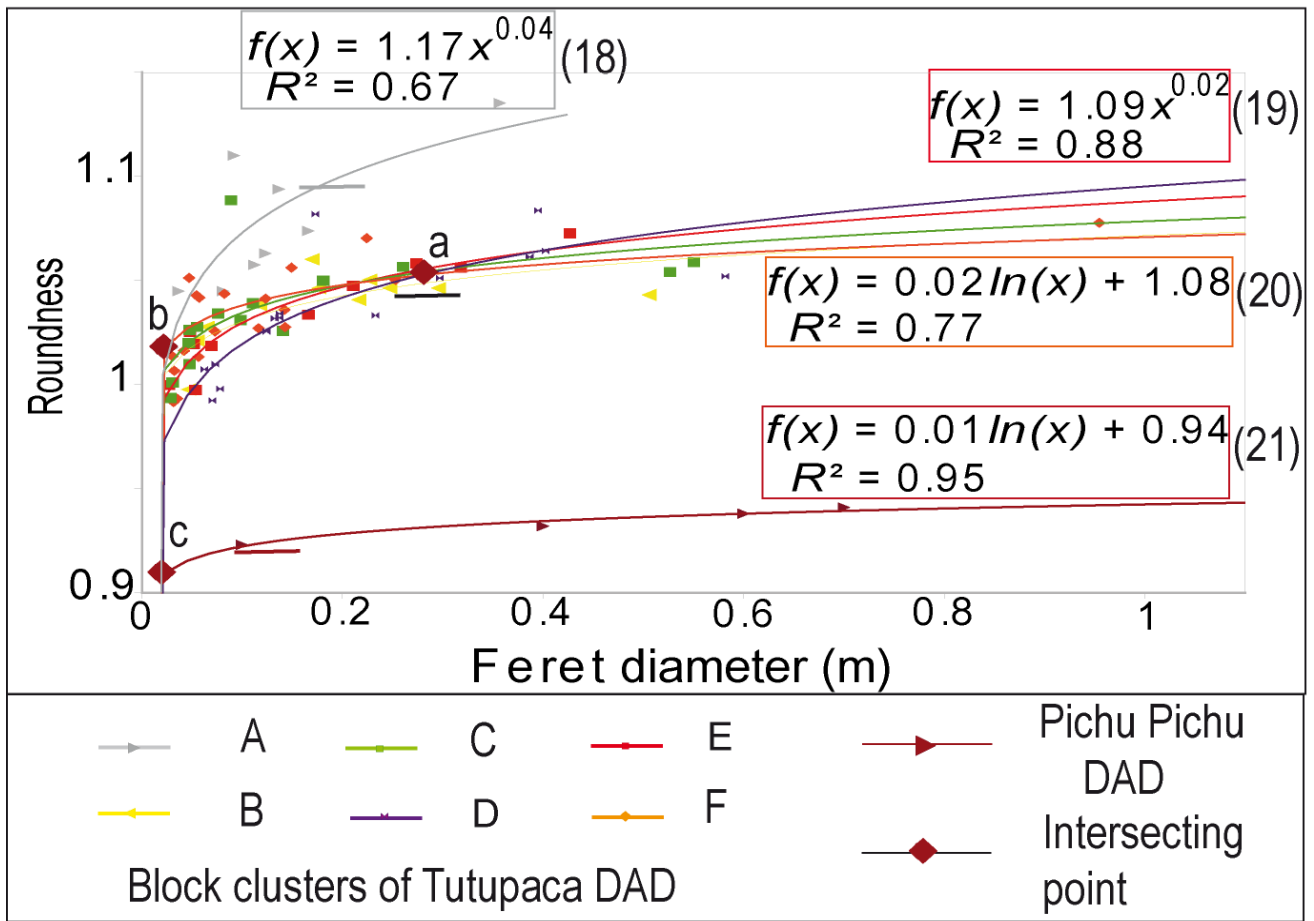
807

808 **Fig. 9.** Roundness vs. Feret's diameter (m) of block lithofacies and striations in different zones from

809 shape analysis using the software ImageJ (404 blocks, 635 striations and impact marks; [Blott and Pye,](#)

810 [2008](#); [Crawford and Mortensen, 2009](#)). The *horizontal lines* indicate the Feret's diameter at which

811 roundness stopped increasing. Error bars are smaller than the symbols.



812

813 **Fig. 10.** Roundness vs. Feret's diameter (m) of block clusters from shape analysis using the software
 814 ImageJ (Blott and Pye, 2008; Crawford and Mortensen, 2009). The horizontal lines indicate the Feret's
 815 diameter at which roundness stopped increasing. Error bars are smaller than the symbols (see
 816 Supplemental File 2).

817

818

819

820

821

822

823

824

825

826

827

828

829

830 **Table 1.** List of acronyms and their definitions.

831

	Acronyms	Definitions
	<i>A</i>	Area
	<i>a/b</i>	the largest axis / minor axis
	<i>D</i>	Fractal dimension
	<i>d</i>	Depth
	<i>E</i>	Ellipse
	Ellipse/ <i>a/b</i>	The ratio of the ellipse to the <i>a/b</i>
	<i>FD</i>	Feret's Diameter
Quantitative parameters	<i>H</i>	Height
	<i>h</i>	Exponent of the power regressions
	<i>H/L</i>	Apparent friction
	<i>L</i>	Length
	<i>S</i>	Surface
	<i>T</i>	Thickness
	<i>v</i>	Velocity
	<i>V</i>	Volume
	<i>W</i>	Width
		DR-DAD
Lithofacies	HA-DAD	Hydrothermally-rich debris avalanche deposit
	P-PDC	Paipatja pyroclastic density current deposit

832

833

834 **Table 2.** Methodology for block laboratory analysis.

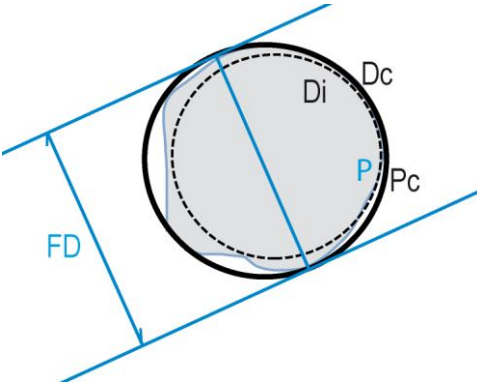
835

Outcrop map and observations	Google Earth imagery, landforms, faults, orientations, lateral and vertical variations in block lithofacies and lithostratigraphy, textures.
Grain size analysis	Image analysis and Feret's diameter measurement. Clast size distribution: cumulative curves, fractal distributions, statistical parameters.
Shape analysis	Shape analysis with texture of blocks, preferred orientation of block largest axis and

shape parameters.

836
837
838
839
840
841
842
843

Table 3. Clast shape parameters with Feret's Diameter (*FD*), Riley's circularity (*R_c*) and Roundness (*R*, Blott and Pye, 2008; Crawford and Mortensen, 2009; Bernard, 2015).

	<p>Feret's Diameter (<i>FD</i>)</p> <p>The longest distance between two parallel tangential lines</p>
	<p>Riley's circularity (<i>R_c</i>, Riley, 1941)</p> $R_c = \sqrt{D_i / D_c}$ <p><i>D_i</i> the largest inscribed circle <i>D_c</i> the smallest circumscribed circle</p>
	<p>Roundness (<i>R</i>)</p> $R = P / P_c$ <p><i>P</i> Perimeter <i>P_c</i> Convex perimeter</p>

844
845
846
847
848

Table 4. Fractal results of block lithofacies in different zones and striations compared to the surrounded matrix of the Paipatja avalanche deposits and P-PDC (see Supplemental File 1; Suzuki-Kamata et al., 2009).

852
853

	<i>h</i>	<i>D</i>	Correlation coefficient	Range of the clast size (cm)	Number of clasts
A	1,37	0,26	0,9	6.7-22.1	14
B	0,67	1,66	0,9	13.2-47.5	18
C	1,7	-	0,9	10.4-22.9	78
D	2,29	-	0.95	233.4-539.5	7
E	1,92	-	0.93	30.3-68.7	9
F	0,58	1,83	0,9	10.7-96.5	120

All zones	0,86	1,28	0,9	11.4-40.3	137
Surrounded matrix	0.07-1.16	0.67-2.84	0.91-0.98	0.001-6.4	-
Striations	1.18	0.6	0.9	5.94-44.68	265

854

855

856

857 **Table 5.** Mean values of block shape parameters and striations from SPO and shape analysis using the
858 software ImageJ (404 blocks, see [Supplemental File 2](#); [Launeau and Robin, 2005](#); [Blott and Pye, 2008](#);
859 [Crawford and Mortensen, 2009](#); [Bernard, 2015](#)). These shape data have been associated with the
860 correspondent standard errors.

861

	Roundness	Riley's circularity	<i>a/b</i>	Ellipse	Ellipse/ <i>a/b</i>
A	1.07±0.01	0.73±0.03	1.68±0.14	3.61±0.74	2.29±0.54
B	1±0.02	0.69±0.02	1.88±0.38	3.2±0.65	1.7±0.24
C	1.02±0.001	0.68±0.006	1.63±0.3	3.34±0.25	2.04±0.15
D	1.13±0.07	0.64±0.05	1.91±0.26	5.15±2.18	2.7±0.59
E	1±0.02	0.64±0.02	1.8±0.2	5.01±1.25	2.78±0.33
F	1.05±0.03	0.63±0.01	2.1±0.06	3.95±0.24	1.88±0.35
Mean	1.23±0.009	0.66±0.005	1.7±0.03	3.5±0.15	2.05±0.1
Striations	0.9±0.01	0.3±0.007	3.69±0.1	21.9±1.57	5.82±0.5

862

863

864

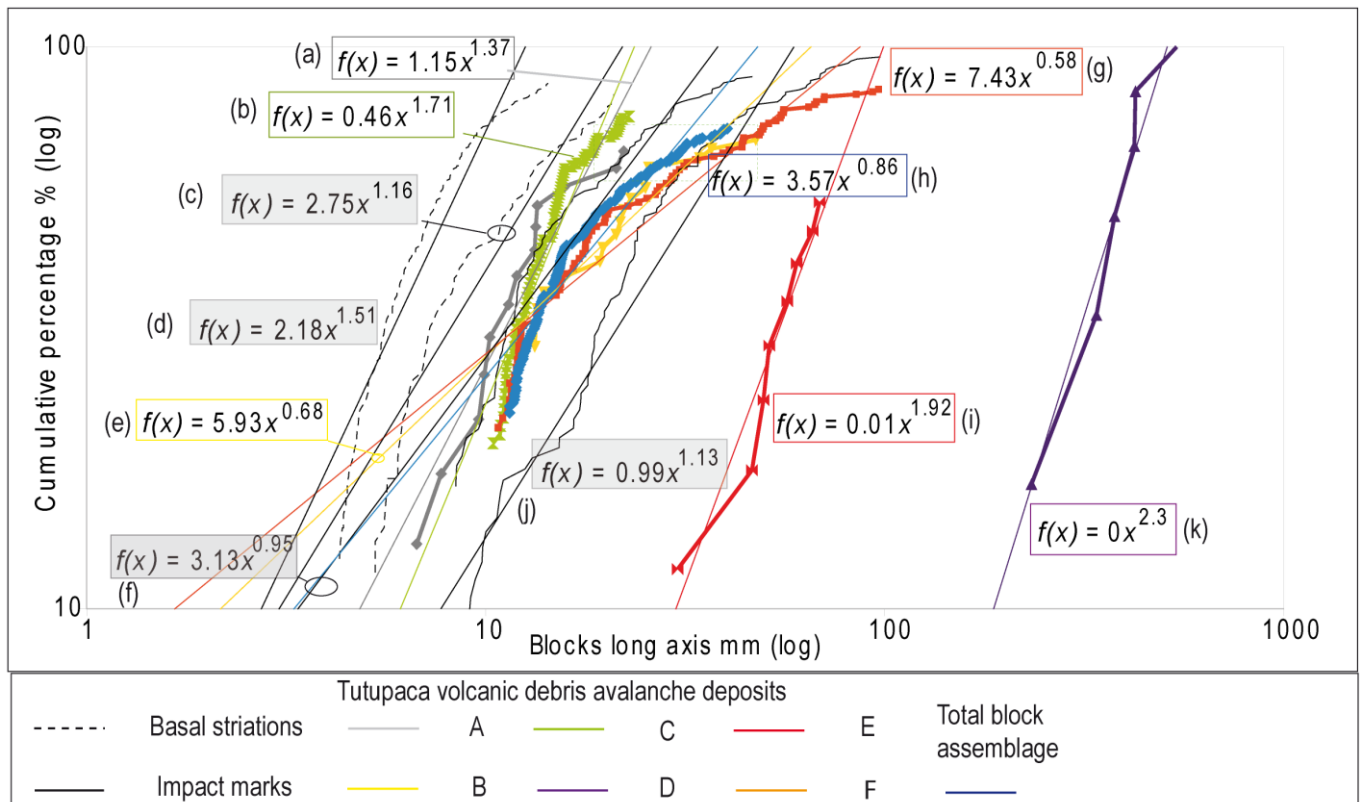
865

866

867

868

869



870

871 **Supplemental File 1**

872 Cumulative % vs. long clast-axis on double log graph. The exponent h of size distributions were
 873 estimated from the power regressions (a-k) by the methods of the least squares ($R^2 > 0.9$ in Table 4, Eq. 6
 874 in Suzuki-Kamata et al., 2009). The h values obtained for each structural unit ranged from 6.7 to 537.9
 875 cm for block lithofacies and from 5.94 to 44.68 cm for striations. From following equation $2h + D = 3$
 876 (Eq. 7 in Suzuki-Kamata et al., 2009), we translate the h -values into fractal D values in Table 4. The h -
 877 values for the block lithofacies and striations range from 0.58 to 2.29 (Table 4). Substitution of these
 878 values into the previous equation (Eq. 7 in Suzuki-Kamata et al., 2009), gives corresponding fractal D -
 879 values of 0.26 to 1.83. The negative values of fractal dimension have not been considered in Table 4.

880

881

882